Synthetic Three-Dimensional Voxel-Based Microstructures that Contain Annealing Twins

Submitted in partial fulfillment of the requirements for

the degree of

Doctor of Philosophy

in

Materials Science and Engineering

Lisa H. Chan

B.S., Chemical Engineering, University of California – Irvine
B.S., Materials Science and Engineering, University of California – Irvine
M.S., Materials Science and Engineering, Carnegie Mellon University

Carnegie Mellon University
Pittsburgh, PA

May, 2010

Acknowledgments

I would like to thank my advisors, Dr. Anthony Rollett and Dr. Gregory Rohrer, for their guidance, support, and advice throughout the years. I would also like to express my gratitude to my committee members, Dr. Katayun Barmak, Dr. Marc De Graef, and Dr. David Saylor for their crucial discussions and review of the dissertation. Furthermore, Dr. David Saylor is acknowledged as the original author of the misorientation-based version of the orientation assignment algorithm.

Special thanks are given to Dr. Stephen Sintay for his invaluable discussions and help in both my experimental and computational investigations. I would like to thank Dr. Hasso Weiland, and Dr. Soonwuk Cheong for their advice on the corrosion studies of aluminum, Dr. Robert Heard for his supervision on the OIM analyses of the GBE 718+ alloy, Dr. Sukbin Lee for providing me with the meshing and GBCD binning algorithms, Dr. Samuel Lim for providing me with the rolled copper orientation map, and Dr. Michael Groeber for providing me with the reconstructed Inconel 100 structure. Many thanks are also given to my fellow research group members and the members of the MRSEC group. Last but not least, I am grateful to my family and friends for their encouragement and support.

This work was supported in part by the Materials Research Science & Engineering Center (MRSEC) of the NSF under grant DMR-0529425, and by The Pennsylvania Technology Investment Authority.

Abstract

The five-parameter grain boundary character distribution (GBCD) of a material contains both the grain boundary plane orientation and the lattice misorientation information. This work focuses on generating three-dimensional microstructures that match the full five-parameter GBCD obtained from experimentally observed microstructures. Microstructures that contain annealing twins are of particular interest in this investigation. The statistics that are used to quantify the differences between the synthetic and experimentally observed structures are texture or orientation distribution (OD), GBCD, number and area fractions of Σ3 and coherent Σ3 boundaries, Σ3 cluster distribution, and twin density.

The main simulation code used in this study is the grain orientation assignment algorithm. This algorithm consists of taking a digital three dimensional microstructure and assigning orientations to the grains through a simulated annealing based optimization method, such that the generated orientation distribution and misorientation distribution or five-parameter GBCD will match the user-defined values. The generation methods used in creating the digital voxel-based microstructures and the methods used to reconstruct experimentally measured structures with the dual-beam microscope are discussed. From performing the grain assignment algorithm with different textures and misorientation distribution (MD) as the target distributions, it was found that when the OD and MD are incompatible, a compromise must be made in order for the two distributions to fit together in the structure. The studies of matching several textures, MD, and GBCD to various microstructures indicated that the neighbors per grain and grain boundary areas have significant effects on the possible OD, MD, and GBCD that can exist in the structure.

Due to the unique features of the annealing twins, a twin insertion algorithm is used to generate annealing twins in the synthetic microstructures. To demonstrate the capability of the

twin insertion algorithm, the twin grains were removed from an experimental structure, Inconel 100, and were then regenerated with the twin insertion algorithm. The largest Σ3 cluster measured in the experimental Inconel 100 structure consists of 98 grains, which can only be observed by analyzing the fully-reconstructed 3D structure.

Table of Contents

List of Tables

List of Figures

Chapter 1 Introduction

1.1 Motivation

Crystalline materials are generally aggregates of a large number of single crystals. Grain boundaries are the transition regions between two adjacent grains of different crystal orientations [1]. When the misorientation between the two crystals is small (<15°), the grain boundary can be described by relatively simple dislocation configurations and is termed a low-angle boundary. For example, a low-angle tilt grain boundary is composed of edge dislocations. When the misorientation is large (≥15°), the grain boundary will involve more complex structures of dislocations, vacancies, and displaced atoms, and is termed a high-angle boundary. Since grain boundaries have a relatively open structure as compared to the bulk, the atoms that make up the non-equilibrium structure at the boundary have higher energies than the bulk atoms [2, 3]. Therefore, chemical reactions, such as etching and corrosion, and solid-state mass transport effects, such as diffusion and atomic segregation, occur preferentially along the grain boundaries [2]. Since the free volume and energy vary between different grain boundary types, not all boundaries are equally sensitive to chemical attack or mass transport effects. Many different grain boundary dependent properties, such as the resistance to fatigue cracking, and intergranular corrosion, have been found to be dependent on the crystallographic nature of the grain boundaries [4, 5]. Therefore, it is necessary to control the distribution of grain boundary types in a microstructure. One method of controlling this is a process known as Grain Boundary Engineering (GBE) [5].

In face-centered cubic (FCC) metals, Grain Boundary Engineering typically involves maximizing the density (or length fraction) of high symmetry boundaries as denoted by low sigma (Σ) values for Coincident Site Lattice (CSL) relationships. Recent studies have shown that

by increasing the fraction of low-Σ CSL boundaries, properties such as intergranular corrosion cracking resistance [6], creep resistance [7], strength [8], and fatigue cracking resistance [9] of the material can be improved. An example of the influence of grain boundary engineering on the properties of a material can be found in Section 3.1.1. Studies on aluminum alloy 2124 show how boundaries with different CSL relationships can yield different intergranular corrosion responses.

One major shortcoming in the CSL-based studies is that only 10% of researchers have analyzed the grain boundary plane distributions [10, 11]. Further discussion on the need to study the grain boundary plane orientations can be found in Section 4.2. One way to define the five parameters is to specify the lattice misorientation and the boundary normal. In face-centered cubic and low stacking fault energy metals, annealing twinning events are considered to be the most effective way of increasing the populations of low-Σ CSL grain boundaries [12]. Some researchers have even coined the phrase "twin-induced grain boundary engineering" where the goal of the thermal mechanical treatment is only focused on maximizing the number of annealing twins or the length fractions of Σ3 grain boundaries in the microstructure [13-17]. However, not all grain boundaries with the Σ3 relationship have improved properties. For example, Gertsman *et al.* [18], Henrie *et al.* [19], and Lin *et al.* [20] have observed that not all Σ3 boundaries are corrosion or crack resistant, and analyzed the angle of deviation between the boundary trace of the cracked Σ3 boundaries and the {111} trace of the grains on either side of the boundary. In the Ni-based and Fe-based austenitic stainless alloys, Gertsman *et al.* [18] observed that 2% of the cracked boundaries have a Σ3 relationship, and have boundary traces that deviated from the {111} trace by 5.1°-8.1°. In 304 stainless steel, Henrie *et al.* [19] observed that the corroded Σ3 boundaries deviated from the ideal {111} trace by an average of 48.8° whereas the non-corroded

Σ3 boundaries only deviated from the {111} trace by 20.9°. In melt-spun Ni_3Al ribbons, Lin *et al.* [20] found that only incoherent Σ3 boundaries were cracked. The results from these researchers show that the difference in the corrosion resistance among Σ3 boundaries is due to the variation of the grain boundary plane orientations found in coherent and incoherent twin boundaries. This is one example of the reasoning behind the necessity of including grain boundary plane distributions in the study of GBE. Also, many researchers have referred to the distribution of CSL boundaries as the grain boundary character of the material [14, 17, 21-23]. In this study, the term grain boundary character distribution (GBCD) consists of the distribution of plane normals and the misorientation of the crystal lattice at the grain boundary, as consistent with studies performed by Randle *et al.* [24, 25] and Rohrer *et al.* [26, 27].

Another problem with GBE is that the thermal mechanical processes that are used to increase the fraction of CSL boundaries also change the grain shapes of the microstructure. An example of such changes is shown in Section 3.1.2 through comparisons between a conventional and a GBE processed nickel-based superalloy.

Computer simulations is an efficient method for analyzing the effects that GBCD may have on the properties of the materials without having to perform multiple thermal mechanical processes that may change the grain shapes. However, a statistically representative microstructure, especially one that contains annealing twins, must be generated before these material property simulations can be performed. This study focuses on the generation of the synthetic microstructures that contain annealing twins. A review of the studies performed by other researchers on simulating annealing and deformation twins is presented in Section 4.4. In these studies, most of the computer simulations were performed on thin-films or two-dimensional structures with nanocrystalline grains. The work presented here focuses on creating

large enough sets of annealing twins, that can both satisfy the misorientation relationship and the boundary plane normal requirement of coherent Σ3 boundaries.

1.2 Hypothesis

It is possible to statistically generate three-dimensional microstructures that match the full five-parameter grain boundary character distribution obtained from experimentally observed microstructures. The microstructures that are used to test the hypothesis are face-centered cubic materials that contain annealing twins. The statistics that are used to quantify the differences between the synthetic and experimentally observed structures are (a) texture, (b) five-parameter grain boundary character distribution, (c) number and area fractions of Σ3 and twin boundaries, (d) Σ3 cluster distribution, and (e) twin density (number of twins per grain).

1.3 Objectives

To generate a microstructure that statistically matches experimentally observed structures, the current study concentrates on the following objectives:

- Create digital microstructures that do not contain twins.
- Define grain boundary plane orientations.
- Develop a simulation model that assigns orientations to the grains such that the orientation and the five-parameter misorientation distributions in the digital microstructures match the target values to an acceptable accuracy.
- Synthesize annealing twins in the microstructure such that the Σ3 cluster distribution, twin boundary fractions, and texture measurements match the statistics gathered from experimentally observed microstructures.

Chapter 2 Background

2.1 Crystallography

The main objective of this section is to provide a general context for understanding grain orientations, textures, misorientations, and the most commonly used methods in representing their respective distributions.

2.1.1 Orientations

The orientation of a grain can be thought of as a transformation of the axes from the crystal reference frame to the external sample reference frame. This transformation can be represented by axis-angle pairs, 3x3 matrices, Euler rotational angles, Rodrigues-Frank vectors, and homochoric (equal volume partitions) space vectors. The axis-angle pair, Euler angle, and matrix representation will be described below, while the other representations can be found in Section 2.1.4.

The axis-angle pair is defined by the common axis that exists between the sample and crystal reference frame such that a single rotation (ω), brings the two reference frames into coincidence with each other, as illustrated by Fig. 2.1. The most commonly used parameterization for representing orientations is with three Euler angles, using either the Bunge [28], Roe [29], or Kocks [30] conventions. In this study, the Bunge convention will be used. In the Bunge convention, the definition of the three Euler rotation angles (ϕ_1, Φ ϕ_2) can be thought of as a set of physical rotations of the crystal reference frame, which is initially coincident with the sample reference frame, until the crystal reference frame matches the orientation of the grain. An illustration of the Euler angle definition is seen in Fig. 2.2 where the Euler angles (ϕ_1, Φ ϕ_2) are defined by first rotating about the z-axis of the crystal reference frame, which equates to ϕ_1,

then secondly rotating around the x-axis of the crystal reference frame to obtain the second angle, Φ, and lastly rotating around the rotated z-axis to obtain the last Euler angle ϕ_2 when the crystal reference frame matches the orientation of the grain. The 3x3 matrix representation of the orientation can be calculated with Equations 2.1 and 2.2 once the axis-angle or Euler angle representations are obtained.

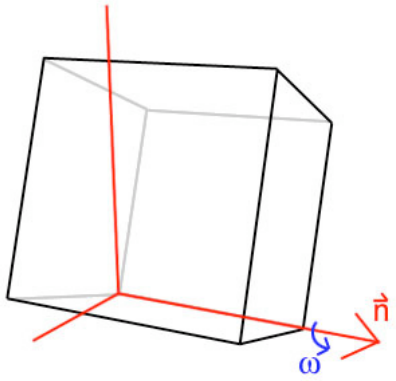

Figure 2.1 Image of an axis-angle representation of a grain orientation, where $\vec{n}$ is the common axis and ω is the rotational angle.

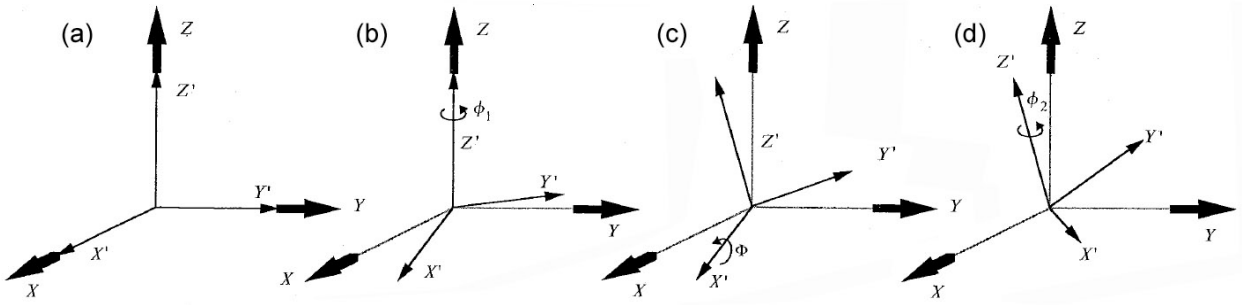

Figure 2.2 Euler angles definition. (a) The sample and crystal reference frames are coincident with each other. (b) After the first rotation of the crystal axes of $\phi_1$around Z'. (c) After the second rotation of the crystal axes by an angle of Φ around X'. (d) After the third rotation of the crystal axes of ϕ_2 around the already rotated Z' axis. The image was obtained from [31].

$$g(\omega < u,v,w >) = \begin{bmatrix} \cos\omega + u^2(1-\cos\omega) & uv(1-\cos\omega) + \sin\omega & uw(1-\cos\omega) - v\sin\omega \\ uv(1-\cos\omega) - w\sin\omega & \cos\omega + v^2(1-\cos\omega) & vw(1-\cos\omega) + u\sin\omega \\ uw(1-\cos\omega) + v\sin\omega & vw(1-\cos\omega) - u\sin\omega & \cos\omega + w^2(1-\cos\omega) \end{bmatrix} \quad (2.1)$$

$$g(\phi_1, \Phi, \phi_2) = \begin{bmatrix} \cos\phi_1 \cos\phi_2 - \sin\phi_1 \sin\phi_2 \cos\Phi & \sin\phi_1 \cos\phi_2 + \cos\phi_1 \sin\phi_2 \cos\Phi & \sin\phi_2 \sin\Phi \\ -\cos\phi_1 \sin\phi_2 - \sin\phi_1 \cos\phi_2 \cos\Phi & -\sin\phi_1 \sin\phi_2 + \cos\phi_1 \cos\phi_2 \cos\Phi & \cos\phi_2 \sin\Phi \\ \sin\phi_1 \sin\Phi & -\cos\phi_1 \sin\Phi & \cos\Phi \end{bmatrix} \quad (2.2)$$

Texture is the average crystallographic orientation of the grains in a material, and is usually measured from a statistically representative set of grains. Typically, a material is considered to be textured when the average crystallographic orientation shows a preference to a certain direction. The units of measure for this characterization (or distribution) are multiples of random distribution (MRD), which indicate texture whenever this value is different from 1. To normalize any distribution into MRD values, the distribution is scaled such that the multiplication of the sum of the values per bin with the size of the bins is equal to the volume of the bins. A comparison between MRD, probability density functions and cumulative probability functions can be found in Appendix A. Some of the common methods to portray orientation information or texture are through the use of pole figures and plots in Euler angle space. Examples of these representations can be found in Section 7.1.3.

2.1.2 Rolling and Fiber Textures

Texture arises frequently due to the slipping and twinning events that occur during deformation processes, which give rise to preferred orientations. In analyzing deformed FCC metals, two types of deformation textures can be formed depending on the material's stacking fault energy. The copper type texture is usually formed in materials with high stacking fault energy, and the brass type texture is usually formed in materials with low stacking fault energy [32]. In this study, deformation textures obtained from high stacking fault energy materials, such as copper (γ_{SFE} ~ 78 mJm^{-2}), will be discussed. This deformation texture will henceforth be referred to as "rolling texture". An example of an orientation distribution that is characteristic of

rolling texture is shown in Fig. 2.3. The distribution is represented both on a {111} pole figure and in Euler space. The texture components and their corresponding Euler angle definitions that are typically studied for the rolling texture are listed in Table 2.1 [33].

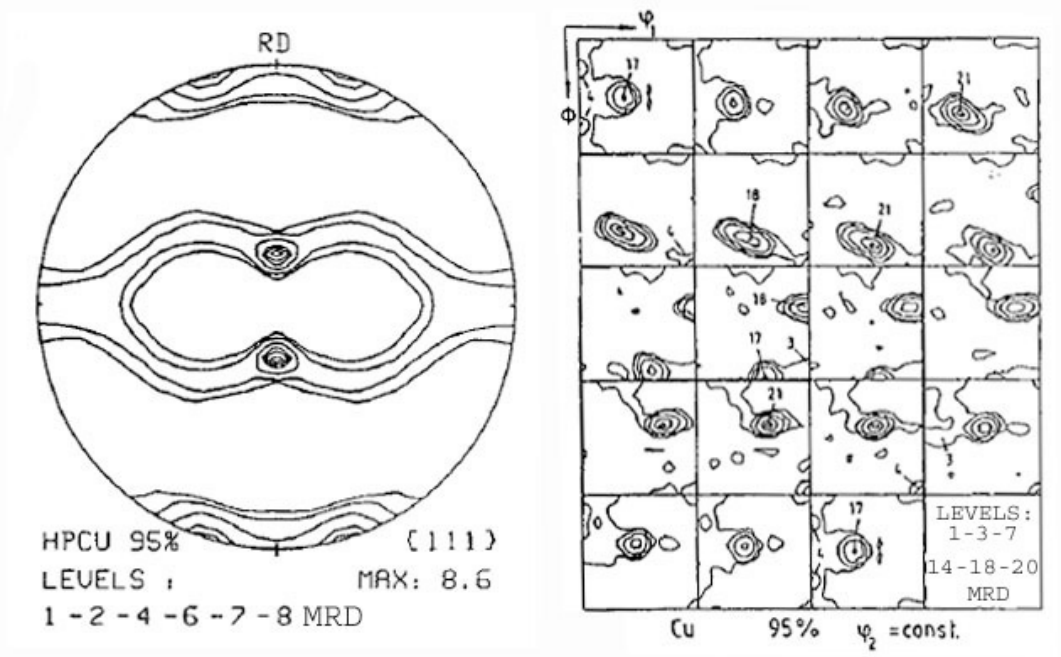

Figure 2.3 (Left) {111} pole figure, and (right) Euler angle plot at every 5° of ϕ_2 showing rolling texture obtained from 95% reduced copper, which is also the typical deformation textures found in high stacking fault materials [34].

Table 2.1 Texture components typically observed in rolled face-centered cubic materials and their respective Euler angle definitions [33].

Texture Component	**Bunge Euler angles (degrees)**		
	ϕ_1	Φ	ϕ_2
Cube	0	0	0
Goss	0	45	0
S	59	37	63
Brass	35	45	0
Copper	90	35	45

The rolling texture mentioned above can be defined as the combination of the texture components listed in Table 2.1, although in reality, a continuous range of orientation is present as the orientation distribution shown in Fig. 2.3 indicates. A fiber texture however, contains a continuous range of grain orientations, in which a specific crystallographic direction is parallel to

one of the sample axis directions. In this study, only the most commonly analyzed fiber textures will be used: the <100>, <110>, and <111> fiber textures. When pole figures are plotted for fiber textures, the centers of the polar plots in some cases correspond to the fiber axis direction (e.g. the <111> fiber texture appears as a single peak at the center of the {111} pole figure).

2.1.3 Misorientations

Misorientation is defined as the transformation between two crystal orientations, and therefore can be represented by any of the orientation parameterizations described in the previous section. However, it is an arbitrary choice as far as picking which crystal to rotate into coincidence with the other is concerned. Therefore, there are $2xN^2$ equivalent misorientations with N being the number of proper symmetry operators for the corresponding crystal structure. In the case of cubic materials, there are N=24 proper symmetry operators, which yield 1152 equivalent misorientations. To select a single misorientation to represent all equivalent misorientations, a selection rule must be imposed. This selection rule will be defined below with the definition of the fundamental zone in Section 2.1.5.

2.1.4 Rodrigues-Frank Space and Homochoric Space

Heinz and Neumann have discussed two disadvantages in using the Euler angle space to plot the orientation distribution [35]. In plotting orientations in the Euler angle space, a degeneracy exists where any sets of rotations with the second angle $\Phi=0$, and $\phi_1+\phi_2$ = constant cannot be differentiated from each other. The other problem with Euler angle space is that angle axis pairs that share the same axis do not appear in the plot as a straight line but a curly line through the space. Also, no simple rules exist for combining two sets of Euler angles together (e.g. to compute a misorientation) whereas well established rules for combining Rodrigues-Frank

vectors together are available. Frank mentioned that the most favorable advantage in using Rodrigues-Frank vectors space is the fact that varying rotation angles about the same axis appear as a straight line in Rodrigues-Frank space [36].

Given an orientation representation of a unit vector $\vec{n}$ and angle ω, the relationships between the axis-angle pair, Rodrigues-Frank vector, and homochoric space vector representations are given by Equations 2.3-2.4 respectively [36].

$$\vec{R} = \vec{n}\tan\left(\frac{\omega}{2}\right) \tag{2.3}$$

$$\vec{H} = \vec{n}\left[\frac{3}{4}(\omega - \sin\omega)\right]^{\frac{1}{3}} \tag{2.4}$$

2.1.5 Fundamental Zones

The term fundamental zone is first defined by Frank [36] as the region which the Rodrigues-Frank vector [36, 37] lies closest to the origin. However, the usage of the fundamental zone is not limited to the Rodrigues-Frank vector representation. In any representation of an orientation or misorientation, a fundamental zone is the region that contains one and only one representative for any orientation or misorientation. Out of all the symmetrically equivalent orientations or misorientations, the unique representative is selected through the use of the axis-angle pair representation. For misorientations, the selected representative is the set of axis-angle pairs that has the smallest rotation angle (ω) and the rotation axis that contains all positive components in which the relation: u≥v≥w≥0 is satisfied. With the aforementioned selection rule, in cubic materials, the rotational angle ranges from 0-62.8 [35], while the axis always lies somewhere inside (or on the edge of) the standard stereographic triangle (SST) highlighted in red shown in the stereographic projection of Fig. 2.4.

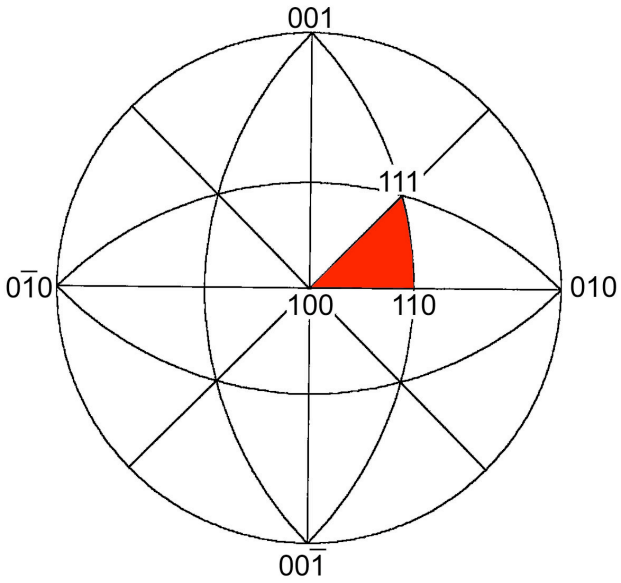

Figure 2.4 A stereographic projection with one standard stereographic triangle for cubic materials highlighted in red.

In representing orientations, the rotation axis cannot be changed with symmetry, and thus the selection rule simply becomes finding the orientation with the smallest rotation angle. In Rodrigues-Frank vector space, this means that the Rodrigues-Frank vectors must satisfy Equations 2.5-2.6. The fundamental zone traced out by Equation 2.5 is a cube in the Rodrigues-Frank vector space with edge length $\sqrt{2}-1$, while Equation 2.6 causes the truncated corners to appear as shown in Fig. 2.5a [35]. In tracing the fundamental zone for misorientations however, the additional selection rule of the rotation axis further decreases the size of the fundamental zone as shown in Fig. 2.5b.

$$R_i \le \sqrt{2}-1 \tag{2.5}$$

$$\sum_{i=1}^{3} R_i \le 1 \tag{2.6}$$

The fundamental zones for orientations and misorientations in homochoric space are very similar to the ones found for Rodrigues-Frank vector space. The main difference between the two fundamental zones is that the faces of the fundamental zone have a slightly bowed out surface for homochoric space rather than a flat surface for the Rodrigues-Frank space. In this

study, homochoric space is used for comparing the distributions of grain orientations and misorientations because of its ability to be easily divided into equal volume elements [36]. In the Euler angle space of $0 \leq \varphi 1 \leq \frac{\pi}{2}, 0 \leq \Phi \leq \frac{\pi}{2}, 0 \leq \varphi \leq \frac{\pi}{2}$, 36 copies of the fundamental zone is stored for misorientations while 3 copies of the fundamental zone is stored for the orientations. On the other hand, only one copy of the fundamental zone is stored for both the orientation and misorientation in homochoric space. The fundamental zone in homochoric space is partitioned by dividing each of the three dimensions into equal sections. Once the space is subdivided into equal volume elements, the orientation or misorientation distribution can be treated as a one dimensional histogram. However, the one major disadvantage in using the homochoric space is that once an orientation or misorientation has been binned into the corresponding volume element, it is difficult to convert the orientation or misorientation into a different representation.

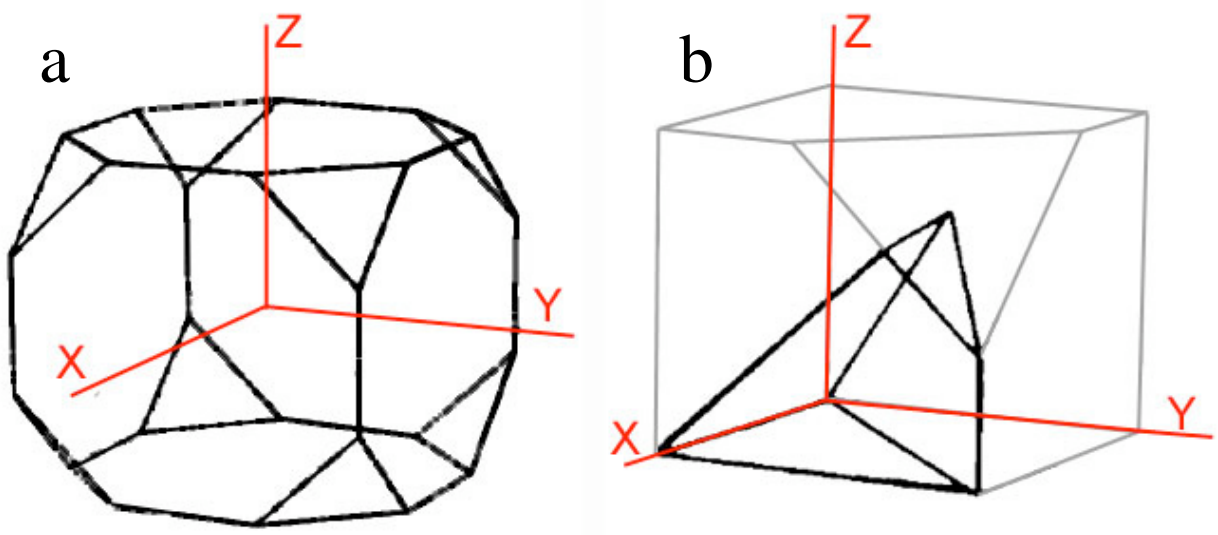

Figure 2.5 (a) Cubic Rodrigues orientation space. (b) Cubic Rodrigues misorientation space highlighted in black. The first octant of Rodrigues orientation space is drawn in grey to clarify the difference in the size between the orientation and misorientation fundamental zones. Images were modified from [35].

2.2 Grain Boundary Characteristics

In this section, the definition of the CSL boundary relationships, the method to discretize the grain boundary character distribution, and the observations of annealing twins in both two and three-dimensional views are discussed.

2.2.1 CSL boundaries

Kronberg and Wilson were the first to introduce the concept and importance of the coincident site lattice (CSL) theory [38]. CSLs are defined by the finite fraction of crystal lattice sites that coincide between the two lattices. The quantity sigma (Σ) is then defined as the volume ratio between the unit cell of coinciding sites and a standard unit cell, which is also the reciprocal density of coinciding sites [38]. An example of a Σ5 relationship is shown in Fig. 2.6 [39]. It should be noted that the CSL theory is only a geometrical concept, and as such, any boundary can be defined as a CSL boundary provided that the sigma value is allowed to approach infinity [40].

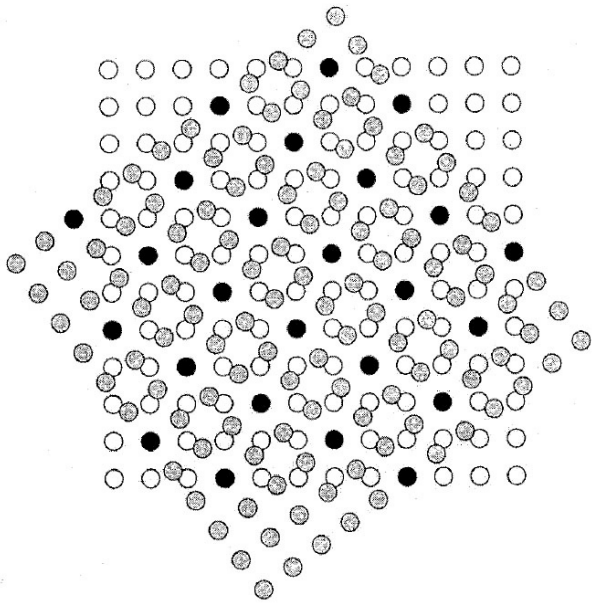

Figure 2.6 Two overlaying lattices (grey and white), with the black atoms being the coinciding lattice sites. This is an example of a Σ5 relationship. Image obtained from Humphreys and Hatherly [39].

A general procedure for calculating sigma values from misorientations is provided by Ranganathan [41]. Since CSL sigma values are simply defined by the overlaying of lattices, some of the CSL sigma values can be obtained by different misorientations that are not related by symmetry. These sigma values are distinguished by a letter designation in the order of increasing misorientation angle [42]. A truncated list of axis-angle pair definitions of Σ values of up to Σ29b are given in Table 2.2 [42]. Read and Shockley were the first to propose that low angle grain boundaries close to a Σ1 relationship could be categorized as a defective version of a Σ1 boundary since the small deviation from the exact relationship could be accounted for by dislocations [43]. Various criteria have since been proposed by other researchers in defining the maximum allowable angular deviation $(\Delta\theta)$ such as the Read-Shockley approximation [44], Palumbo-Aust criterion [45], and Brandon's criterion [46]. In this study, Brandon's criterion was used to identify the allowable spread of the exact CSL relationships in misorientation space. Brandon's criterion states that a grain boundary can be assigned a certain sigma value if the angle of deviation from the exact CSL relationship satisfies,

$$\Delta\theta \leq \frac{15^{\circ}}{\sqrt{\Sigma}} \tag{2.1}$$

Experimental studies by other researchers have shown that grain boundaries with a low-Σ relationship (Σ≤29) exhibit improved properties. Creep resistance [7], and intergranular degradation such as intergranular corrosion [47, 48], and fatigue cracking [9] resistance, have been shown to increase with increasing fraction of the low-Σ boundaries.

In this study, the Rodrigues-Frank vector space was used to plot the misorientations because for all the CSL boundary relationships that are of interest in this study (∑ values up to

29b), their definitions appear as unique positions in the Rodrigues-Frank fundamental zone. An example of one of the chosen fundamental zones is shown in Fig. 2.7.

Table 2.2 Coincident site lattice relationships. Reproduced from Table 4.1 of [39].

Sigma (Σ)	**Misorientation Angle (°)**	**Misorientation Axis**
1	0	Any
3	60	< 111 >
5	36.87	< 100 >
7	38.21	< 111 >
9	38.94	< 110 >
11	50.48	< 110 >
13a	22.62	< 100 >
13b	27.80	< 111 >
15	48.19	< 210 >
17a	28.07	< 100 >
17b	61.93	< 221 >
19a	26.53	< 110 >
19b	46.83	< 111 >
21a	21.79	< 111 >
21b	44.40	< 211 >
23	40.45	< 311 >
25a	16.25	< 100 >
25b	51.68	< 331 >
27a	31.58	< 110 >
27b	35.42	< 210 >
29a	43.61	< 100 >
29b	46.39	< 221 >

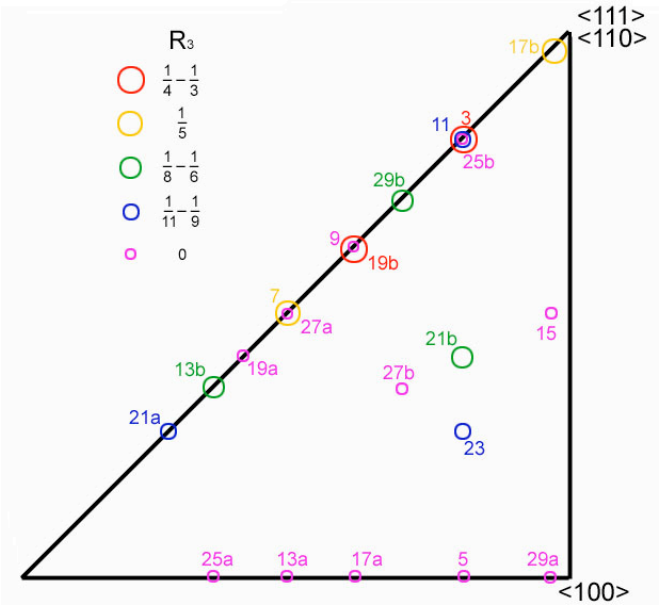

Figure 2.7 Top view of a Rodrigues-Frank fundamental zone showing the locations of the CSL boundary relationships.

2.2.2 Grain Boundary Character Distribution

Grain boundaries can only be distinguished from one another when five independent macroscopic parameters are defined [49]. The grain boundary character distribution (GBCD), which consists of the distribution of grain boundary types and planes in a material, will be characterized with all five parameters that relate to the grain boundary: three parameters for specifying the lattice misorientation and two parameters for specifying the boundary plane orientation. Therefore, the GBCD function, $\lambda(\Delta g, \mathrm{n})$, is defined as the relative areas of internal interfaces that have a misorientation $\Delta g = g_1 g_2^T$ and an interface normal, **n** [27].

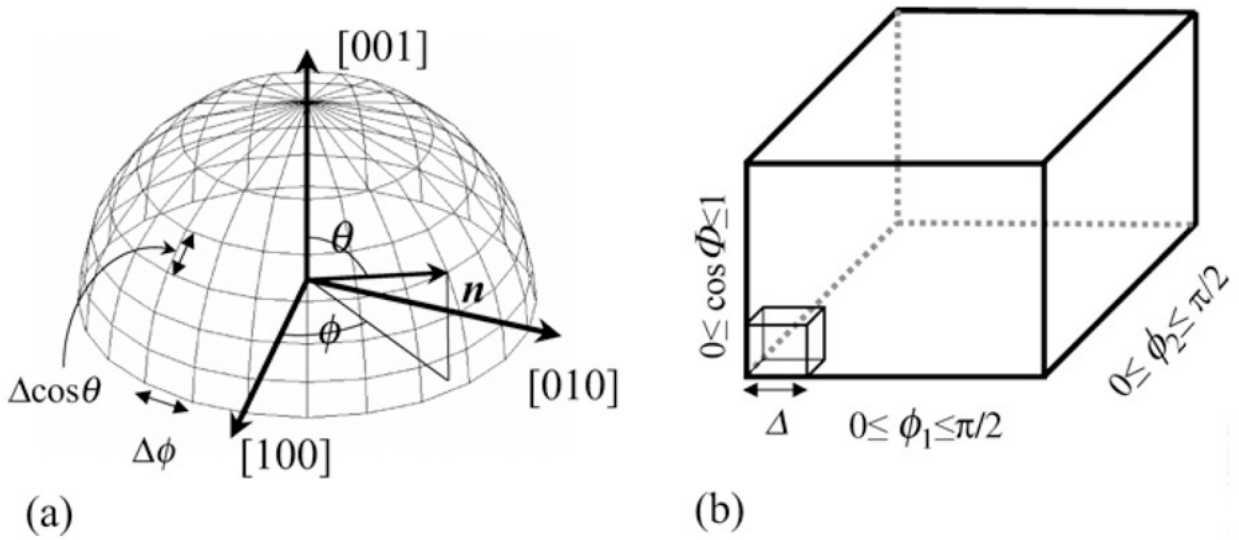

Figure 2.8 The parameterization of the GBCD function with (a) spherical angles that represent the interface normal, and (b) the three Euler angles that represent the lattice misorientation [27].

For easier analysis of the grain boundary types that exist in the system, $\lambda(\Delta g, \mathrm{n})$ is parameterized into discrete cells by using the three Euler angles (φ_1, Φ, φ_2) that represent the lattice misorientation, and two spherical angles (θ, φ) that represent all possible interface normals. For any material, the Euler angles φ_1, Φ, and φ_2, range from 0 to 2π, π, and 2π respectively. In the parameterization of the misorientation, the angles φ_1, cos(Φ) and φ_2 are used to subdivide the Euler angle space into equal volumes. For the interface normals, the spherical angles θ and φ range from 0 to π and 2π respectively and cos(θ) and φ are used to discretize the domain of the interface normals into equal areas. The discretization of $\lambda(\Delta g, \mathrm{n})$ with respect to the five parameters is shown in Fig. 2.8. The homochoric subdivision of the Euler angle space into equal volumes and the interface normal space into equal areas allows for each cell to have an equal probability of being populated by a random grain boundary. When the population of each cell is divided by the total population in $\lambda(\Delta g, \mathrm{n})$, the units of measurement become multiples of random distribution (MRD). Hence, for a random GBCD, all cells in $\lambda(\Delta g, \mathrm{n})$ would have the same values, which is equivalent to an MRD value of 1.

A common way of displaying the GBCD is by first choosing a particular misorientation, and then plotting the relative areas of grain boundaries with the specified misorientation as a function of grain boundary plane orientation on a stereographic projection plot.

2.2.3 Annealing twins

Annealing twins are commonly observed in FCC materials that have low-stacking fault energies. It should be noted that from here on, unless otherwise specified, any reference to twins in this study has to do with annealing twins rather than mechanical or deformation twins. The main difference between mechanical twins and annealing twins is that mechanical twins are generated from the cross-slipping of partial dislocations [50], while one of the mechanisms believed to be responsible for the generation of annealing twins is growth accidents that occur during the migration of the grain boundaries [51]. A review on the formation mechanisms of annealing twins can be found in Section 4.3.

A twin boundary in FCC materials is generated with a 180° rotation of the lattice about the twin plane normal, which forms a 60°<111> misorientation (the CSL Σ3 relationship) between the twin grain and the neighboring grain or the grain the twin is residing in (the parent grain). The twin boundary is considered coherent when the Σ3 boundary has a 60 [111] misorientation and a plane normal parallel to the [111] direction in both adjacent crystals.

Most studies of annealing twins by other researchers were performed on the planar sections of the materials. An example of the four most common morphologies of annealing twins observed in two dimensions are shown in Fig. 2.9 [52]. In the case of C, where a twin does not completely span the grain in this section plane, steps can be seen at the short edge of the twin as shown in the bright field image and illustration of Fig. 2.10a and 2.10b respectively. As seen in the illustration, only the longer boundaries highlighted in red are coherent with the grain. In

the studies of increasing the fraction of low-Σ boundaries, twinning events have been found to be very effective in introducing low-Σ boundaries [12].

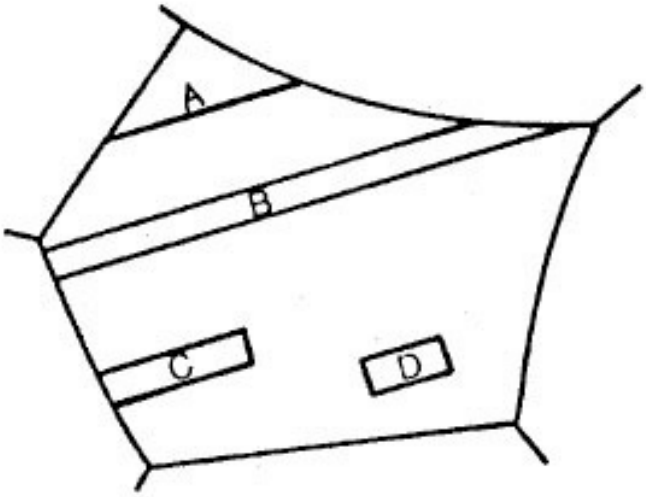

Figure 2.9 The four prominent morphologies of annealing twins found on two-dimensional sections [52].

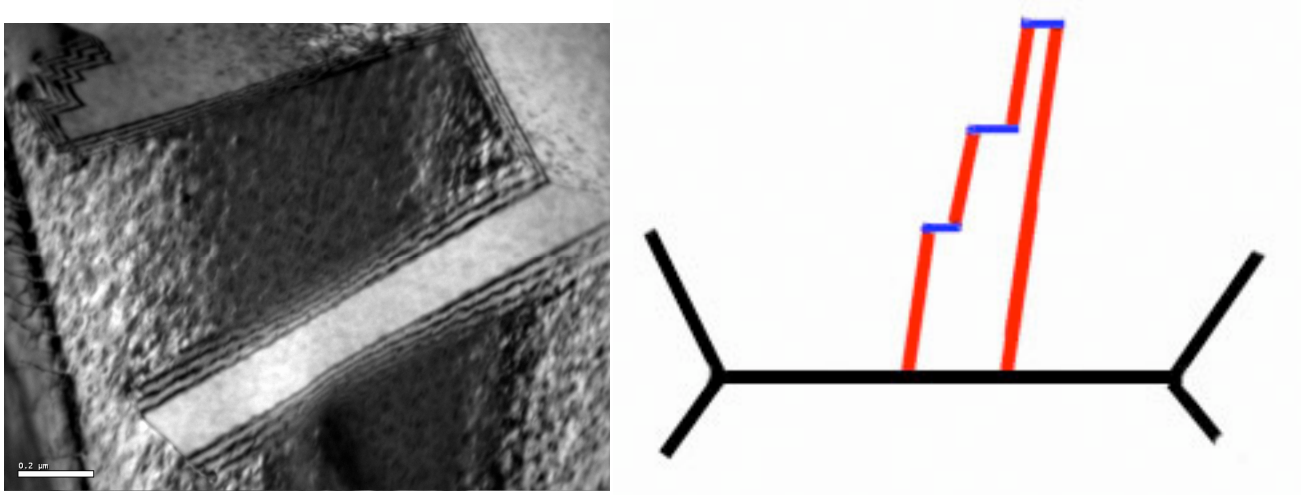

Figure 2.10 (a) A bright field image of an annealing twin observed under the transmission electron microscope in the 718+ alloy discussed in Section 3.1.2. (b) An illustration of an annealing twin with coherent boundaries highlighted in red and incoherent boundaries highlighted in blue.

One of the problems with observing twins on a planar section of the structure is that it is not possible to measure how the planar section intersects with a twin. If the observation plane is parallel with the twin's flat interface, the twin grain will not have the morphologies that are observed in Fig. 2.9. Therefore, to truly observe the behavior of the twin grains, a three

dimensional view of the twin is necessary. Bystrzycki and his coworkers [53, 54] have reconstructed the annealing twin grain shape through the use of serial sectioning on a $NiMn_2$ alloy. Bystrzycki *et al.* [53, 54] characterized the annealing twin shape with only two categories: lamellae twins or edge twins. Lamellae twins are characterized by a combination of two parallel coherent grain boundaries and irregular incoherent grain boundaries, while edge twins can be approximated as tetrahedrons. However, the division between the two shapes is not distinct, as Bystrzycki *et al.* [53, 54] also mentions that twins have frequently been found to have a mix of lamellae and edge twin features. As seen in Fig. 2.11, Bystrzycki *et al.* [53, 54] used AutoCad [55] to reconstruct the twins, and from the image, it is very difficult to quantify or categorize the grain into any particular shape. In this study, with the three-dimensional tools that are available, reconstruction, presentation, and analysis of the twins will be improved, as seen in Fig. 2.12. Chapters 6 and 9 of this dissertation explain how twin grains can be characterized and synthesized in either the computer generated or experimentally observed microstructures.

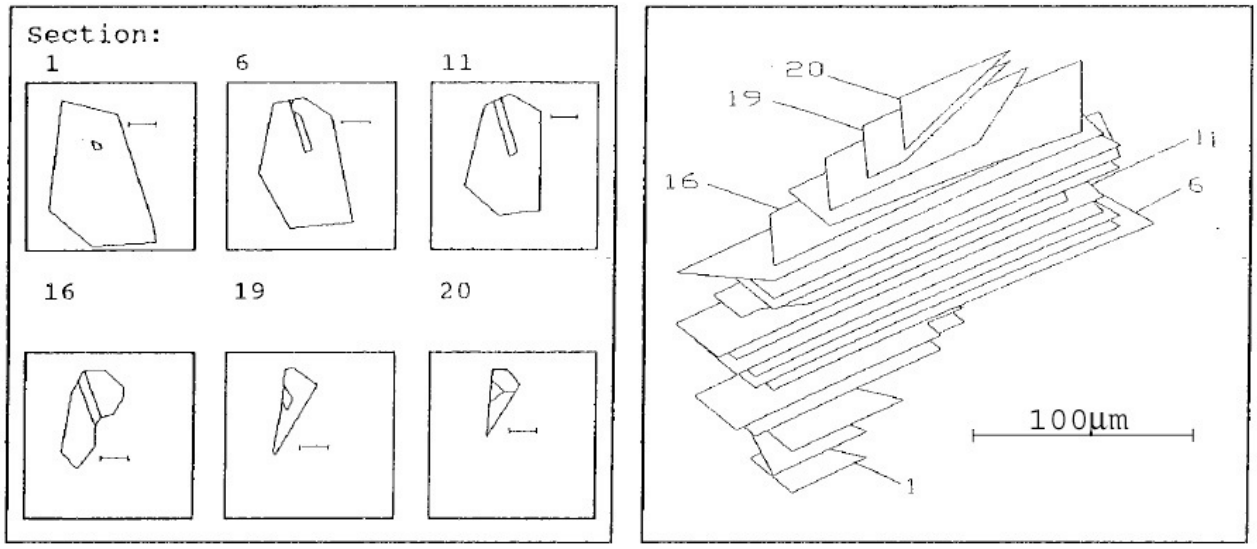

Figure 2.11 Bystrzycki *et al.*'s (left) serial sections and (right) the reconstructed 3d view of the lamellar twin [53, 54].

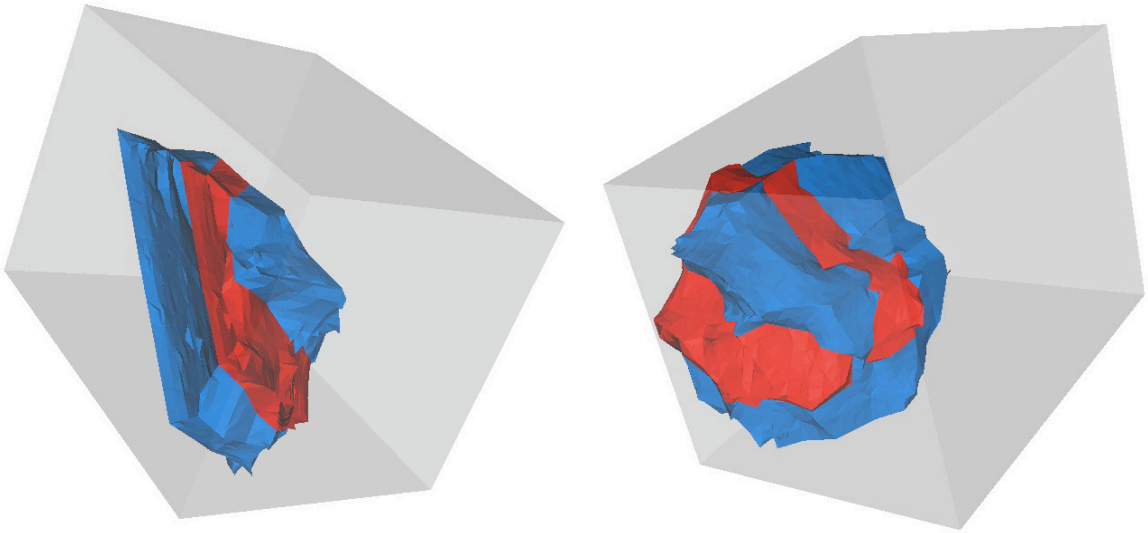

Figure 2.12 Three dimensional view of a grain cluster, obtained from a reconstructed Inconel 100 data set [56, 57], showing the twin grain (red) cutting through the parent grain (blue). Left and right images simply show the different angles of observing the grains.

2.3 Simulated Annealing

Simulated annealing was used to assign grain orientations to the voxelized microstructures. Simulated annealing is an efficient method for finding the desired global minimum or maximum values for a function that contains many independent variables [58]. As the name implies, simulated annealing is formed based on the observations of real-world annealing phenomenon. In the annealing procedure, a heated system with random configurations can either be quenched or slow-cooled to reach a lower energy state. In terms of computer models, the quenching of the material is similar to an iterative improvement method, while the slow-cooling of the material is comparable to the simulated annealing method in searching for a low energy state. A cost function is analogous to the energy of the system, where the goal of the algorithm is to reach the minimum value of this function. The iterative improvement method takes a system of known configuration, and iteratively rearranges the configuration, such that the cost function is lowered, until no further improvement to the cost function can be made [59, 60].

However, the problem with the iterative improvement method is that only the local rather than the global minima will be found.

On the other hand, what is known as the Metropolis procedure [61] is a more generalized iterative improvement where the probability of allowing a proposed move with a higher cost function is defined by the Boltzmann probability distribution [58, 62]. The Boltzmann probability distribution is based on the idea that a system that is in a thermal equilibrium at temperature T will have an energy probabilistically distributed among all the different energy states [63]. The simulated annealing procedure is then the Metropolis algorithm performed at various temperatures. One advantage of this more elaborate procedure is that one can avoid configurations stuck in local minima (in energy or cost). An annealing schedule is typically used to define the constant ratio at which the temperature decreases, and the number of rearrangements allowed at each temperature step [58]. In summary, the simulated annealing procedure requires [63]:

1. The definition of the possible system configurations.
2. A generator that allows for random changes in the system configuration.
3. The definition of a cost function.
4. The starting annealing temperature and the annealing schedule.

Chapter 3 Related Experimental Work

The experimental results presented in this section serve to expand and support the motivation for the work presented in the later sections. Intergranular corrosion studies on the 2124 aluminum alloy yielded results that show why the control of CSL boundary distributions is an important aspect in improving material properties. On the other hand, the studies on a nickel-based superalloy show what problems the thermomechanical treatments involved in GBE can introduce.

3.1.1 Intergranular Corrosion Studies on 2124 Aluminum Alloy

The 2124 aluminum alloy used in the study has a nominal chemical composition (wt %) of Cu: 3.8, Mg: 1.2, Mn: 0.48, Fe: 0.09, Si: 0.04, Zn: 0.04, Ti: 0.02, and balance Al. The 6.3 mm thick material first underwent a heat treatment at 350°C for 2 h followed by air cooling to relieve any residual stress. The material was then cold rolled to 82% reduction through a constant speed rolling mill. After cold working, the samples received a solutionizing heat treatment of 540°C for 2 h. Room temperature water was used to quench the samples immediately after removal from the box furnace. The annealed samples were subjected to ASTM G110 corrosion testing, whereby 2.5 cm x 2.5 cm samples were immersed into a solution of sodium chloride and hydrogen peroxide for 24 h [64]. Cross-sections perpendicular to the rolling plane were mechanically polished for microstructural characterization through Electron Backscatter Diffraction (EBSD). Diffraction data was collected on a Phillips XL40 FEG instrument equipped with an EBSD indexing system provided by EDAX, Inc. using operating parameters of an accelerating voltage of 20kV, a working distance of 17mm, and a step size of 1µm scanning on a hexagonal sampling grid. An example of an EBSD data set is portrayed with an inverse

pole figure map in Fig. 3.1. Figure 3.1 also demonstrates the method used to study the grain boundary data.

Since the raw EBSD data collected with the Orientation Imaging Microscopy (OIM^{TM}) software package contains points where the pattern was incorrectly indexed, either from overlapping of diffraction patterns or uneven topography effects, and points that are not indexed, from the corrosion of the boundaries, the erroneous results need to be corrected. The correction or "clean up" method chosen for this purpose is grain dilation. The grain dilation method first identifies points that do not belong to a grain and groups of points that is smaller than the specified minimum grain size (5 pixels for this study), then changes the orientation of the identified points to match the orientation of the grain with the majority of neighboring points or a neighboring grain that is randomly selected [65]. After the EBSD data has been cleaned, the OIM software can be used to extract the grain boundary information. Grain boundaries were reconstructed with the OIM software by connecting all triple points, or points where three surrounding orientation belongs to three different grains, with straight lines. However, if the furthest perpendicular distance between the reconstructed boundary and the true boundary exceeds a set tolerance, the straight line is segmented such that the reconstructed boundary will follow more closely to the true boundary. Once the grain boundaries were reconstructed, the corroded boundaries were traced by hand onto the cleaned image such that all the reconstructed grain boundaries can be categorized into either the corroded boundary or the non-corroded boundary group.

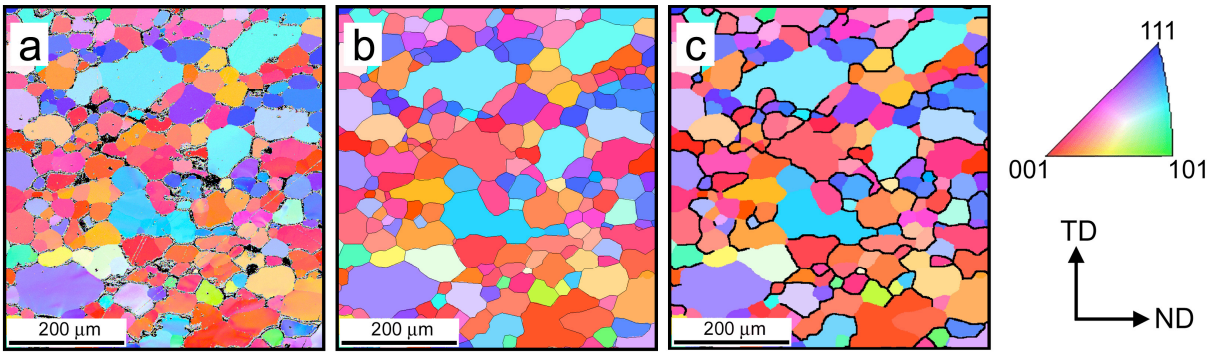

Figure 3.1 Inverse pole figure maps showing the EBSD data (a) as obtained from the OIM system, (b) with the grain segments highlighted after being cleaned up with the TSL software, and (c) with the corroded grain boundaries manually traced back onto the cleaned map.

In the OIM software, the area of each grain, A_i, in a hexagonal grid is given by,

$$A_i = Np_i * S^2 * \frac{\sqrt{3}}{2} \tag{3.1}$$

where Np_i is the number of points that make up grain i, and S is the scanning step size [65]. The circle equivalent diameter of the grain is then calculated with,

$$d_i = 2\sqrt{\frac{A_i}{\pi}}. \tag{3.2}$$

Once the circle equivalent diameter of each grain is calculated, the number-weighted average grain size is calculated with,

$$\bar{d} = \frac{1}{N}\sum_{i=1}^{N} d_i \tag{3.3}$$

while the area-weighted average is calculated with,

$$\bar{d} = \frac{\sum_{i=1}^{N} A_i d_i}{\sum_{i=1}^{N} A_i} \tag{3.4}$$

where N is the total number of grains in the analysis [65]. If the grain size is uniform, the number-weighted and area-weighted average grain sizes will be very close to each other. On the other hand, for non-uniform grain sizes, the area-weighted average will generally yield a larger

grain size than the number-weighted average. For this analysis, both averages were calculated, which gave an area-weighted average grain size of 66.7μm, and a number-weighted average grain size of 41.8μm. The number and lengths of the CSL grain boundary types with Σ≤19 are reported in Table 3.1. From Table 3.1, it can be seen that Σ1 not only dominates in numbers but also in length over the other CSL boundary types.

Table 3.1 Number and length of grain boundaries with a CSL relationship of Σ≤19. (N=number, L=length, and A=area)

	N%	L, m	L,%	<L>, m	L/A, m^{-1}
Total	100.00	95604.7	100.00	30.4	$5.94x10^{-2}$
Σ1	11.49	12440.2	13.01	34.5	$7.72x10^{-3}$
Σ3	3.02	2958.3	3.09	31.1	$1.84x10^{-3}$
Σ5	1.50	1621.8	1.70	34.5	$1.01x10^{-3}$
Σ7	1.24	1148.9	1.20	29.5	$7.13x10^{-4}$
Σ9	1.18	1044.4	1.09	28.2	$6.49x10^{-4}$
Σ11	0.76	769.2	0.80	32.1	$4.78x10^{-4}$
Σ13	0.57	687.6	0.72	38.2	$4.27x10^{-4}$
Σ15	0.57	500.6	0.52	27.8	$3.11x10^{-4}$
Σ17	0.45	523.7	0.55	37.4	$3.25x10^{-4}$
Σ19	0.54	517.3	0.54	30.4	$3.21x10^{-4}$

From a total of 1191 grains (excluding edge grains), 3142 grain boundaries were observed. Of those 3142 grain boundaries, 23% have a Σ≤19 CSL relationship and 49% were corroded. The population of Σ≤19 type boundaries is reported in Fig. 3.2. The percentage of each corroded boundary type is also included in the plot. Since 49% of all grain boundaries were corroded, any boundary type with the 'Corroded' bar covering less than 49% of the 'Population' bar, as denoted by the red lines, in Fig. 3.2 should have a higher corrosion resistance. On this basis, Σ1, 3, 7, and 13 boundaries have a higher resistance to corrosion than the other CSL boundaries analyzed. However, it is uncertain that grain boundaries with a Σ13 relationship truly have a higher corrosion resistance since only 18 boundaries were observed. In the interest of

investigating whether $\Sigma 3^n$ boundaries have higher corrosion resistance, $\Sigma 27$ boundaries were also considered. However, since only six $\Sigma 27$ boundaries were found within the indexed areas, the result was not included in the analysis.

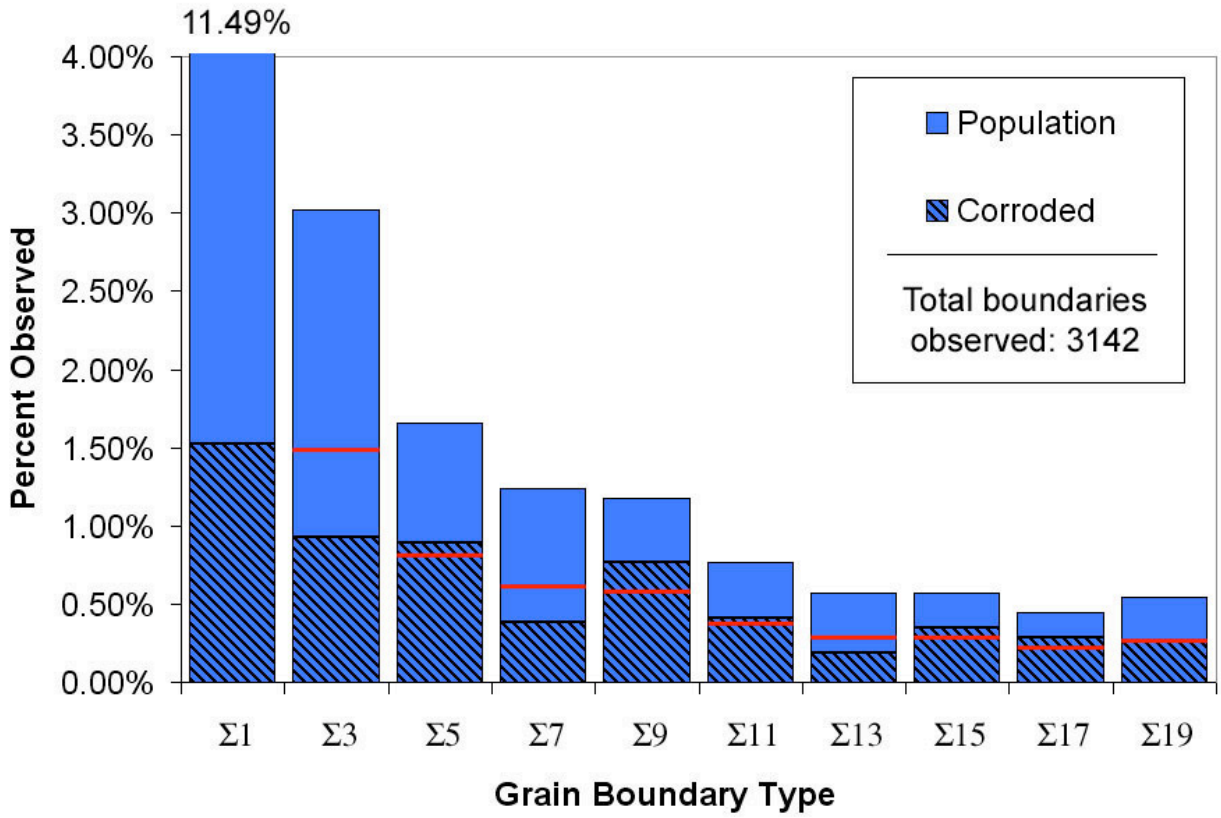

Figure 3.2 The percent of grain boundaries observed is indicated in solid color and within each bar, the percentage of grain boundaries that are corroded is indicated in stripes for each CSL boundary type. The solid red lines denote 49% of the population for each CSL boundary type. Note that the population of $\Sigma 1$ grain boundaries is truly 11.49%. The scale on the y-axis was adjusted to allow easier visualization for the $\Sigma 3$-19 boundary populations.

The limitation of this intergranular corrosion study rests on observing corrosion only on a two-dimensional plane. Without a three-dimensional model of the sample, connectivity studies and grain shape analysis remains limited. However, the difference in corrosion resistance of the grain boundary types, based on CSL relationships, is still clearly observed.

3.1.2 Grain Boundary Engineering of Nickel-Based Superalloy

Conventional and grain boundary engineered samples of 718+, a nickel-based superalloy, were provided by Integran Technologies Inc. for EBSD analysis. Diffraction data was collected with an accelerating voltage of 20kV, a working distance of 17mm, and a step size of 0.5µm and 2µm for the conventional and GBE samples respectively. Examples of the EBSD data sets collected from the two different samples are shown as image quality maps in Fig. 3.3. Even though grain boundaries with a Σ3 relationship have been highlighted in red, it is very difficult to differentiate the fraction of Σ3 boundaries in the two samples in Fig. 3.3. Therefore, Table 3.2 provides a complementary numerical analysis on the different length fractions of the CSL boundaries with $\Sigma \leq 19$. From Table 3.2, it can be seen that the sample that has undergone GBE processing contains a 45% increase in the fraction of Σ3 boundaries compared to the sample that has undergone conventional processing. On the other hand, the populations of the other CSL boundary types have lower fractions, with Σ1 being the most significant.

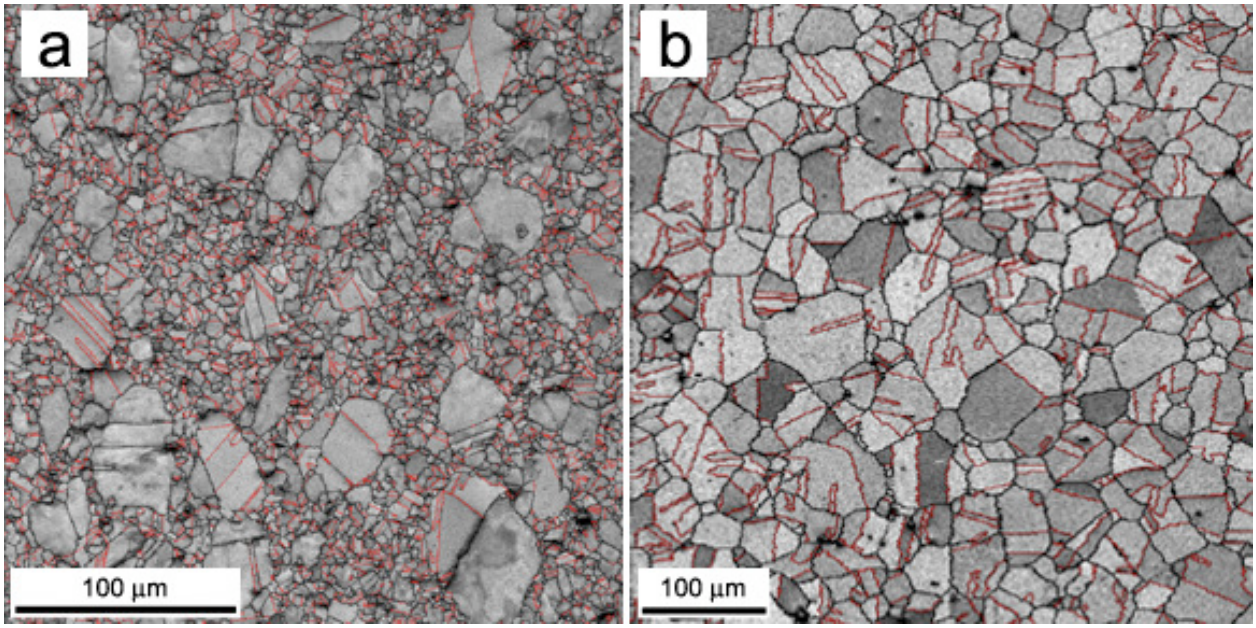

Figure 3.3 Image quality maps showing the (a) conventional and (b) grain boundary engineered 718+ alloy. Grain boundaries with a misorientation angle greater than 15° are highlighted in black, while boundaries with a Σ3 CSL relationship are highlighted in red.

As seen in Fig. 3.3, the grain sizes for the two samples are very different, with the area-weighted average grain size being 10.38 μm and 30.40μm, while the number-weighted average grain size being 3.44 μm and 16.91 μm for the conventional and GBE samples respectively. Moreover, the grain size distribution of the conventional samples is bimodal, suggesting abnormal grain growth. This study is an example of the problems involved in experimentally increasing the fraction of low-Σ CSL boundaries. Even though the fraction of Σ3 boundaries has increased, the grain structures are very different between the conventional and GBE processed samples. Even if improved material performance was observed in the GBE processed material, the improved performance can not be explained with CSL boundary fractions alone. Therefore, time-consuming experimentation on material processing can be avoided by utilizing computer simulations, which is the most cost-effective way to explore the effects of the CSL boundaries on material properties.

Table 3.2 Number and length of grain boundaries with a CSL relationship of Σ≤19 for a conventional and a grain boundary engineered nickel-based superalloy sample. (N=number, and L=length)

	Conventional				GBE			
	N	N, %	L, m	L,%	N	N, %	L, m	L,%
total	141893	100.00	41000.0	100.00	30401	100.00	36000.0	100.00
Σ1	43204	30.45	12474.9	30.42	1233	4.06	1423.8	3.95
Σ3	47070	33.17	13587.9	33.14	14993	49.32	17312.4	48.09
Σ5	691	0.49	199.5	0.49	106	0.35	122.4	0.34
Σ7	956	0.67	276.0	0.67	226	0.74	261.0	0.72
Σ9	2013	1.42	581.1	1.42	767	2.52	885.7	2.46
Σ11	1053	0.74	304.0	0.74	252	0.83	291.0	0.81
Σ13	834	0.59	240.8	0.59	141	0.46	162.8	0.45
Σ15	498	0.35	143.8	0.35	52	0.17	60.0	0.17
Σ17	870	0.61	251.2	0.61	47	0.15	54.3	0.15
Σ19	633	0.45	182.7	0.45	23	0.08	26.6	0.07

Chapter 4 Literature Review

4.1 Statistical Digital Microstructure Generation

Various statistical methods to generate three-dimensional digital microstructures exist with each method exhibiting its own strengths and weaknesses. The traditional method of generating composite microstructures is to evolve a randomly digitized system that contains black and white pixels that represent the two different phases. To evolve the system towards a minimum energy state, two randomly selected pixels of different phases are swapped until good agreement with the target statistics is reached [66-68]. This evolution method automatically preserves the volume fraction of the different phases. Similarly, a genetic algorithm can be employed where a population of points is allowed to evolve by producing offspring [69, 70]. A cost function, such as mechanical response, is used to measure the fitness of the resulting microstructure, and the shape and size of the two phases in the microstructure evolves such that one or more cost functions are optimized. Genetic algorithms are effective in creating two-phase materials where grain information is not required.

In generating a statistically representative polycrystalline material, more complex geometrical shapes are needed to represent a grain [71]. A relatively fast and efficient strategy is to generate a microstructure based on a 3D Voronoi tessellation [72, 73]. Initially, a volume is filled with random points. Voronoi tessellation then constructs bisecting planes perpendicular to the lines joining the points such that the volume is segmented into unique regions with each grain being a single Voronoi cell [74]. Alternatively, Fan *et al.* [75] packs spheres with a lognormal volume distribution into the simulation box, and subsequently uses the centers of the spheres as the initiating points for Voronoi tessellation.

In order to generate microstructures that contain more characteristic grain shapes, many authors have used ellipsoid distributions to approximate the grain size and shape distributions that exist in the real microstructures [76-80]. Brahme *et al.* [76] followed Saylor *et al.*'s [79] method in packing ellipsoids into the simulation box such that the shape and size distributions match experimental values. The grain shape and size distributions are first extracted from orthogonal two-dimensional EBSD maps. A large number of overlapping ellipsoids is then inserted into the simulation box. An active subset of the ellipsoids that will allow maximum space filling and minimum overlapping of ellipsoids are identified. Brahme *et al.* [76] then takes the centers of all the ellipsoids (active or inactive) as points for Voronoi tessellation. The Voronoi cells created by the inactive ellipsoids are then grouped into grains when the seed points of the Voronoi cells lie within the corresponding active ellipsoid. Brahme *et al.* [76] also simulated elongated grains by stretching an equiaxed grain structure along the rolling and transverse directions. On the other hand, Groeber *et al.* [77, 78] extracts the ellipsoid shape and size distributions from a fully reconstructed three-dimensional dataset. The ellipsoids are then packed into the simulation box one by one to maintain the ellipsoid size and shape distributions, and the number of neighbors shared per grain. Once the ellipsoids are packed into the box, Groeber *et al.* [77, 78] takes the centers of the ellipsoids as seed points for Voronoi tessellation. The limitations of the Voronoi tessellation generation method are mainly related to the geometry of the grain boundaries. When structures with equiaxed grains are generally created using one Voronoi cell, the resulting boundary planes are flat and planar. When more than one Voronoi cell is grouped to form a grain, the resulting boundaries are often very rough.

The microstructure generation method used by Saylor *et al.* [79] was described in the previous paragraph with Brahme *et al.*'s [76] generation methods. The difference between

Saylor *et al.* [79] and Brahme *et al.*'s [76] methods is that Saylor *et al.* [79] uses cellular automaton algorithm instead of the Voronoi tessellation with the centers of the ellipsoids as cell centers. The Cellular Automaton (CA) takes the centers of the active ellipsoids as nucleating sites, and allows the nuclei to grow outward with anisotropic growth rates (based on the ellipsoid size) until the entire volume of the active ellipsoids is filled. Further growth is then conducted, without any curvature or energy considerations, until the grains impinge upon one another and it terminates when all the free space in the bounding simulation box is consumed. Saylor *et al.*'s [79] generation algorithm is termed Microstructure Builder and is used for creating some of the digital microstructures used in this study.

St-Pierre *et al.* [80] proposed to generate more realistic microstructures by using the two-dimensional EBSD image as the input for the top surface of the digital structure. The ellipse shape and size extracted from the two-dimensional image are used to recreate the top surface of the structure following Saylor *et al.*'s [79] method, where the centers of the observed grains are used for cellular automaton. After the top surface has been created, the remaining volume in the box is filled with ellipsoids that are inserted one by one from largest to smallest with the ellipsoid center and the orientations are randomly chosen. After 65% of the voxels are consumed by ellipsoids, each remaining free voxel is then assigned to the grain with the nearest ellipsoid center. The limitation to St-Pierre *et al.*'s [80] generation method is that the size of the digital microstructure will be limited by the size of the two-dimensional image obtained from EBSD analysis.

4.2 The Importance of the Five-Parameter Grain Boundary Character Distribution

As mentioned in Section 1.1, Gertsman *et al.* [18], Henrie *et al.* [19], and Lin *et al.* [20] have observed that Σ3 boundaries with different boundary plane orientations can have different

corrosion or crack resistance. However, these researchers did not explicitly measure the grain boundary plane orientations. Through serial sectioning an intergranular stress corrosion cracked X-750 alloy, a Ni-Fe-Cr alloy, Pan *et al.* [81] found that cracked boundaries with CSL relationships of Σ5-49 consist of boundary planes that deviated away from the low-index planes. Some researchers have found that boundary properties correlate more with the boundary plane orientations rather than the CSL criteria [82-84]. In an Al-Cu-Mg-Zn alloy, Field *et al.* [82] found that {111} boundary planes aligned parallel to the rolling plane were more crack resistant. Ohfuji *et al.* [83] found that fracture surfaces occurred more preferentially on {100} planes in pure iron. In pure copper, Miyamoto *et al.* [84] found that grain boundaries with smaller interplanar spacing results in higher corrosion resistance. From the observations made by these researchers, it is evident that the full five-parameter GBCD must be evaluated to correlate not only the lattice misorientation distribution but also the grain boundary plane orientation with grain boundary dependent properties.

4.3 Formation of Annealing Twin Boundaries

Since the formation of annealing twin boundaries was first discussed by Carpenter and Tamura [85] in 1926 the formation mechanism of annealing twins is still under debate today. Many formation mechanisms have been proposed, and can be generally classified into 4 groups: (a) growth accident, (b) grain encounter, (c) stacking-fault packets, and (d) grain boundary dissociation [86]. Each of the 4 groups of formation mechanism will be briefly discussed.

The growth accident mechanism that was first proposed by Carpenter and Tamura [85] in 1926, and later described by Burke [87] and Fullman *et al*. [88], involves the idea that as grain boundaries migrate, stacking faults can occur and generate annealing twins. In 1969, Gleiter

[89] provided an atomistic explanation to the mechanism. During grain growth, atoms transfer from ledges of the shrinking grain to the ledges of the growing grain [89]. Stacking faults can then occur at the ledges of the growing grain, which then leads to the formation of coherent twin boundaries. However, in performing studies on Cu-3wt%Al, Baro and Gleiter [90] found that the growth accident mechanism was not able to explain twin boundary formation at annealing temperatures below 600 C. More recently, Mahajan *et al.* [51] proposed a modified growth accident mechanism, where annealing twin boundaries are formed due to the stacking faults that are accidentally generated on the {111} planes of the migrating boundaries, as seen in Fig. 4.1. The major assumptions of Mahajan *et al.*'s [51] growth accident mechanism are that the grain boundaries must migrate for twin boundary formation to occur, the driving force for boundary migration is dependent on the boundary curvature, which can be described by the ledges of the boundary, and that the ledges of the boundary may lie on {111} planes. Mahajan's [51] growth accident mechanism found support in experimental studies of annealing twin boundary formation in pure nickel, and copper [91], and molecular dynamics simulations in nanocrystalline metals [92].

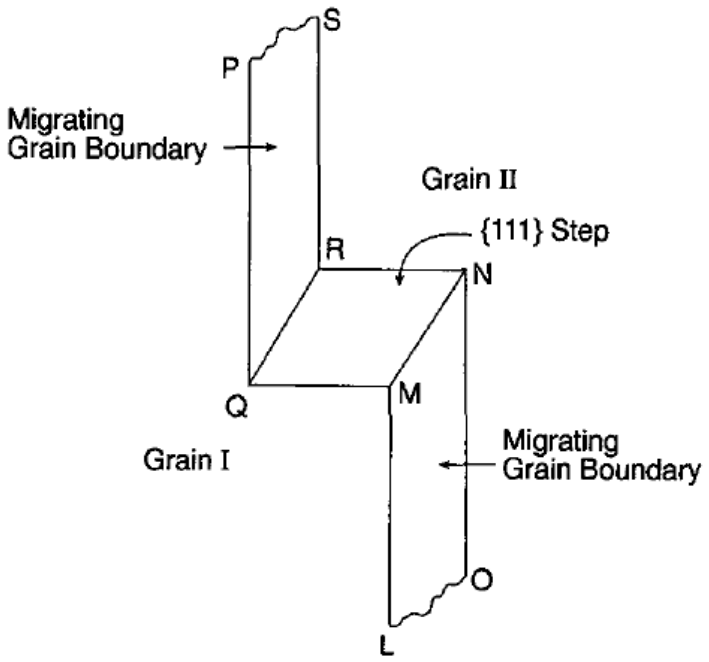

Figure 4.1 Demonstration of the growth accident mechanism proposed by Majahan *et al*. (Fig. 2 of [51]). As Grain I grows and Grain II shrinks, a {111} step (MNQR plane) can sometimes form.

The grain encounter mechanism that was proposed by Burgers [93, 94] and Nielsen [95] formulates that coherent twin boundaries are generated by the motivation to lower system energy when two growing grains meet. The grain encounter mechanism can only explain the formation of a single twin boundary, and can not explain the formation of true twin grains that are bounded by two parallel twin boundaries.

Dash *et al.* [96] proposed that during recrystallization, stacking fault packets are formed, and coalesce into annealing twins. In high purity nickel specimens, Merklen *et al.* [97] observed that thin twins were formed from the coalescence of the stacking faults.

The annealing twin boundary formation proposed by Meyers *et al.* [52] involves grain boundaries dissociating into segments of random and Σ3 boundaries under energetically favorable conditions. In thin-film welded bicrystals of gold, Goodhew [98] observed the dissociation of Σ9, 11, and 99 into Σ3 and other boundaries.

4.4 Simulating Twins

Both annealing twins and deformation twins have been extensively studied and simulated through various means. Since the structures of annealing and deformation twins are very similar in FCC metals, simulations of both types of twins will be reviewed in this section.

In simulating deformation twins, the most commonly used computational tool is molecular dynamics, where the atomic motion is tracked as the simulated material is deformed with high strain rates. Because atomic motion is being tracked in molecular dynamics, the length scale is on the order of angstroms while the time scale is on the order of femtoseconds [99, 100]. Even though parallel algorithms that allow for larger simulation domains and longer timesteps exist, millions of atoms are still needed to simulate a sub-micron size material while thousands of timesteps are needed to simulate picoseconds of deformation behavior [99]. Therefore, most deformation twin simulations are studied on nanocrystalline materials using only a few grains [101-106]. Also, the goal of these studies is not to generate representative microstructures, but to either study the formation mechanisms of deformation twins [101-103] or the effect of deformation twins on material properties [104-106]. Annealing twins have also been simulated using molecular dynamics by Farkas *et al.* [92]. However, the limitations of molecular dynamics remain since Farkas *et al.* [92] only observed the formation of annealing twins in 5nm-sized grains at timesteps up to 1500 ps. Due to the restrictions in length and time scales, molecular dynamics is not a suitable simulation method for generating annealing twins in large simulation domains that will contain thousands of grains.

Gertsman *et al.* [107, 108] has developed a different method for generating annealing twins in two-dimensions. Among the 19 hexagonal-shaped grains, a grain is chosen at random, and a portion of the grain is assigned the twin misorientation [108]. The twin boundary is then

constructed such that the selected portion is divided from the original grain. Twin boundaries are allowed to divide the original grain into two or three parts [107]. An example of Gertsman *et al.*'s simulated microstructure is shown in Fig. 4.2. Since Gertsman *et al*. [107, 108] was only concerned with generating representative misorientation distributions, grain boundary planes were not considered in the simulations. As seen in Fig. 4.2, the twin-generation technique does not produce realistic-looking microstructures that can be compared with experimentally observed structures.

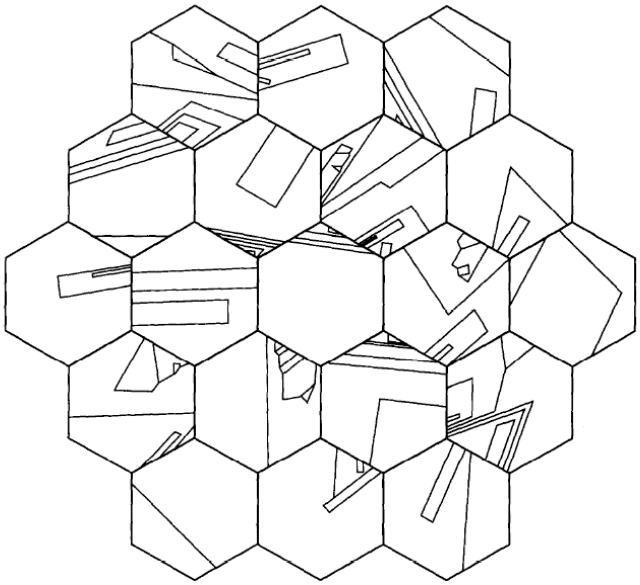

Figure 4.2 An example simulated microstructure created by Gertsman *et al.* [107].

Reed *et al.* [109] has simulated annealing twins by using a Monte Carlo method coupled with the Metropolis algorithm to evolve a pixel-based microstructure to a lower energy state. By assigning negative energies to the Σ1 and Σ3 grain boundaries, these boundaries were favorably created in the structure. An example of the simulated microstructure created by Reed *et al.* [109] is shown in Fig. 4.3. As seen in Fig. 4.3b, the simulated microstructure does not contain any Σ3 grain boundaries that have the appearance of a twin boundary (straight / parallel lines) that is typically observed in planar sections, as shown in Fig. 2.9 in Section 2.2.3.

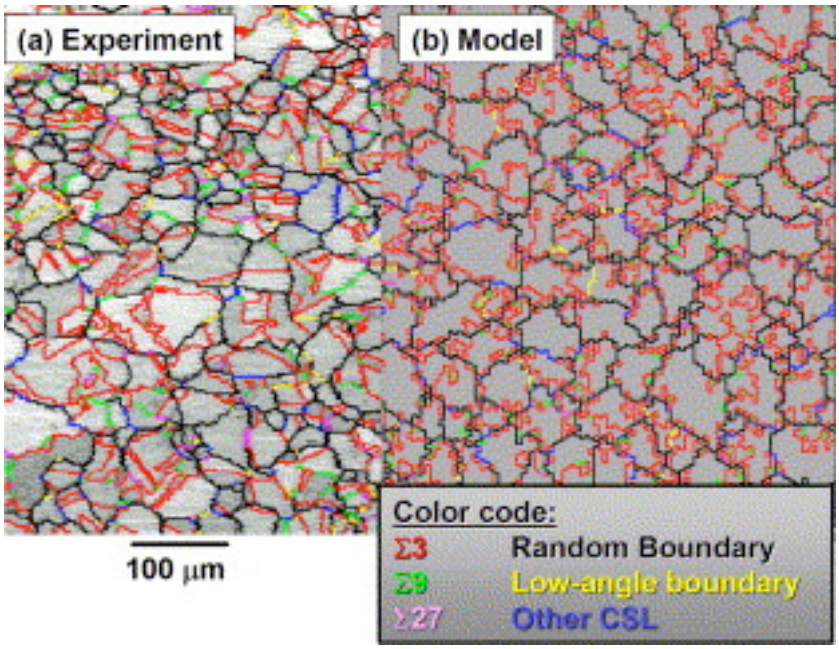

Figure 4.3 (a) Experimental EBSD and (b) simulated microstructure created by Reed *et al.* [109].

Chapter 5 Microstructure Generation

Since the current method of synthesizing annealing twins, discussed in Section 9.1 of this dissertation, only creates coherent Σ3 grain boundaries in an existing microstructure, other methods are required to generate the initial grain structure. In this section, different methods for generating realistic as well as idealized microstructures, and methods for obtaining experimental microstructures are presented. In this study, all microstructures are described with voxel data, where each voxel can be treated as an equiaxed three-dimensional pixel or a cube. In other words, the microstructures are represented as images and boundaries are implicit.

5.1 Synthetic Microstructures

Microstructure Builder was used to create microstructures that are representative of experimentally observed structures [79]. On the other hand, the Plank Generator and Voronoi tessellation growth simulation [110, 111] methods were used to generate some simple microstructures that represent the most simplified structures.

5.1.1 Microstructure Builder

The method used for generating voxel-based polycrystalline microstructures that are representative of experimentally observed structures was developed by other researchers, and is a computer software package known as Microstructure Builder [79]. In Microstructure Builder, the grains in the voxel-based structure are generated by optimally packing ellipsoids into a specified bounding box. The grain population is then controlled by specifying the size of the ellipsoids and the amount of overlap that is allowed between the ellipsoids. Once the ellipsoids are packed into the microstructure, the centers of the ellipsoids are taken as cell centers. These

cell centers are then allowed to grow at different rates based on the ellipsoid sizes until the grains impinge and all the space inside the bounding box is filled [79].

Three examples structures generated with Microstructure Builder are shown in Fig. 5.1. As can be seen in Fig. 5.1, the M1 and M2 structures have more equiaxed grain structures, while M3 is representative of rolled structures. From the plot of grain sizes in the figure, M2 is a structure that is equivalent to subjecting the M1 structure to grain growth. The M1 structure has a much higher number fraction of small grains (relative to the mean size) than the M2 structure. Further numerical details regarding the three different structures' dimensions and grain sizes are given in Table 5.1.

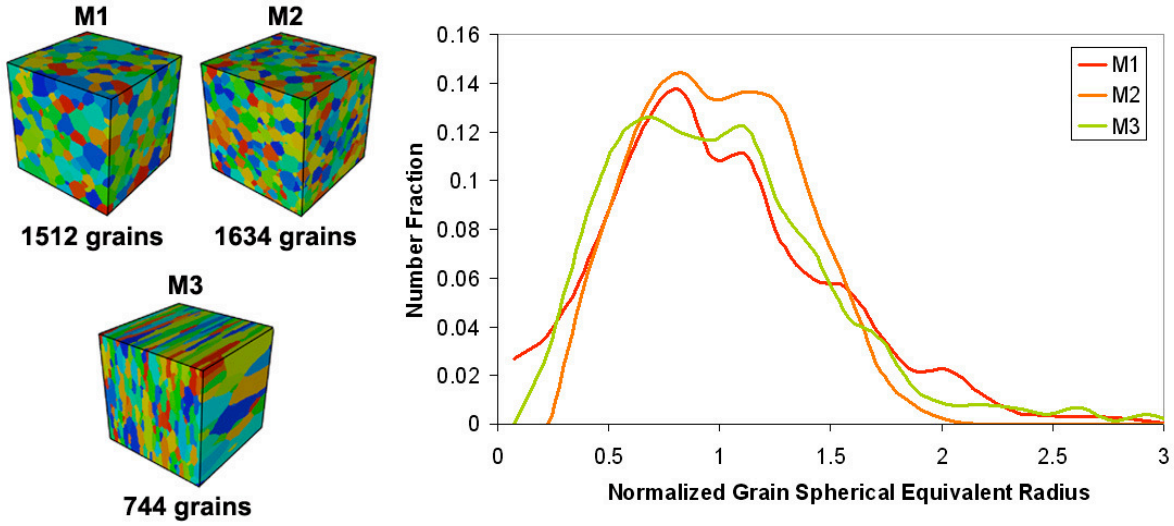

Figure 5.1 Grain structures (left) and the distributions of normalized spherical equivalent radius of the grains obtained from the three different structures generated by Microstructure Builder (right).

Table 5.1 Detailed grain information about the three different structures generated with Microstructure Builder.

Structure	Dimensions (voxels)	Number of Grains	Maximum Grain Volume (voxels)	Average Grain Volume (voxels)	Average Grain Spherical Equiv. Radius (voxels)
M1	200 x 200 x 200	1512	189,184	5295	8.71
M2	128 x 128 x 128	1634	8354	1282	6.05
M3	200 x 200 x 200	744	253,607	10,782	11.16

5.1.2 Plank Generator

The plank structure is the most simple and idealized structure, and can be thought of as a tower of stacked square slices, with each slice having a different grain identification number or orientation. The special feature of this structure is that each grain has two neighbors, which can be thought of as an idealized columnar structure. The plank structure shown in Fig.5.2 is made up of 800 grains with detailed structure dimensions and grain size information given in Table 5.2. As seen in the plot of grain sizes in Fig. 5.2, all the grains in the structure have identical grain volumes. Plank Generator can also generate structures that contain grains of various thicknesses such that a grain size distribution can be imposed without affecting any other geometric feature.

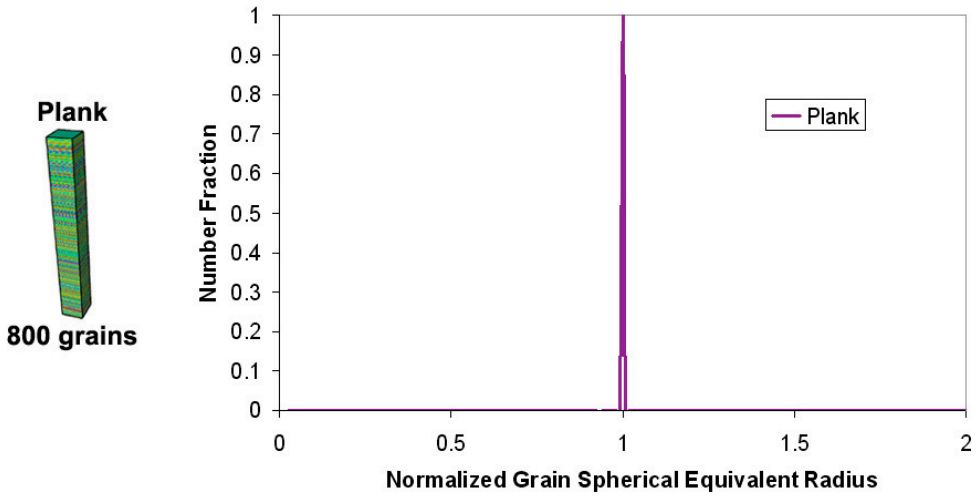

Figure 5.2 Grain structure (left) and the distribution of normalized spherical equivalent radius of the grains obtained from the plank structure (right).

Table 5.2 Detailed grain information about the plank structure shown in Fig. 5.2.

Structure	Dimensions (voxels)	Number of Grains	Maximum Grain Volume (voxels)	Average Grain Volume (voxels)	Average Grain Spherical Equiv. Radius (voxels)
Plank	100 x 100 x 800	800	10,000	10,000	13.37

5.1.3 Voronoi Tesselation Growth

An idealized microstructure of tetrakaidecahedron (14-sided) grains was generated with the Voronoi tessellation growth algorithm that was adapted from Lee [112]. The Voronoi tessellation growth method, outlined by Mahin and Rickman [110, 111], consists of randomly assigning seed points into a bounding cube, and segmenting the volume into unique regions such that each grain consists of one nucleating site. In this dissertation, instead of performing a Voronoi tessellation with randomly placed points, the seed points were placed on a regular grid. In the first layer, the seed points are placed on a square lattice spaced at a distance of r apart from each other. The second layer of points is placed on a square lattice that is shifted by a vector $\left(\frac{r}{2},\frac{r}{2},\frac{r}{2}\right)$ from the first layer of points. The two layers are then repeated in the subsequent layers until the seed points have filled the simulation box. A top view of the placement of the seed points is shown in Fig. 5.3. This placement of the seed points can be thought of as creating a body-centered cubic spatial arrangement of the seed points inside the bounding simulation box. This method of placing the seed points on a body-centered grid will allow the final output of the grains to have the special tetrakaidecahedron shape that is shown in Fig. 5.4. An example of the resulting tetrakaidecahedron structure generated by the Voronoi tessellation method is shown in Fig. 5.5. Because periodic boundary conditions were not used in creating this structure and thus grains touching the edges of the box are truncated, the grain size distribution is not uniform. The widths of the peak seen in the plot of grain sizes in Fig. 5.5 are only a consequence of binning errors. The peak at a normalized grain spherical equivalent radius of just above 1 should be a straight vertical line showing that all interior grains have the same grain size. Numerical details regarding the structure dimensions and grain sizes are given in Table 5.3.

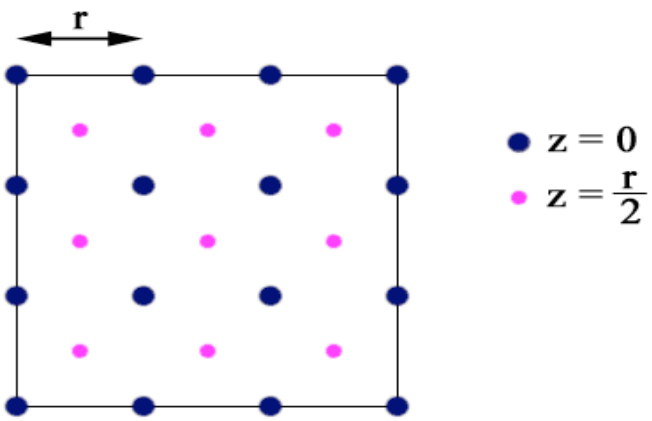

Figure 5.3 Top view of the placement of the initiating points used in Voronoi tessellation for creating structures containing tetrakaidecahedron-shaped grains.

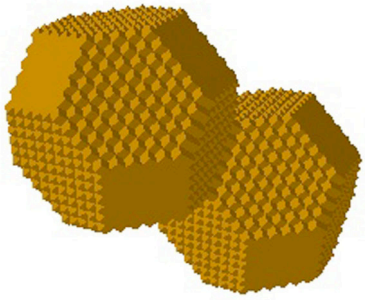

Figure 5.4 Illustration of two tetrakaidecahedron-shaped (14-sided) grains.

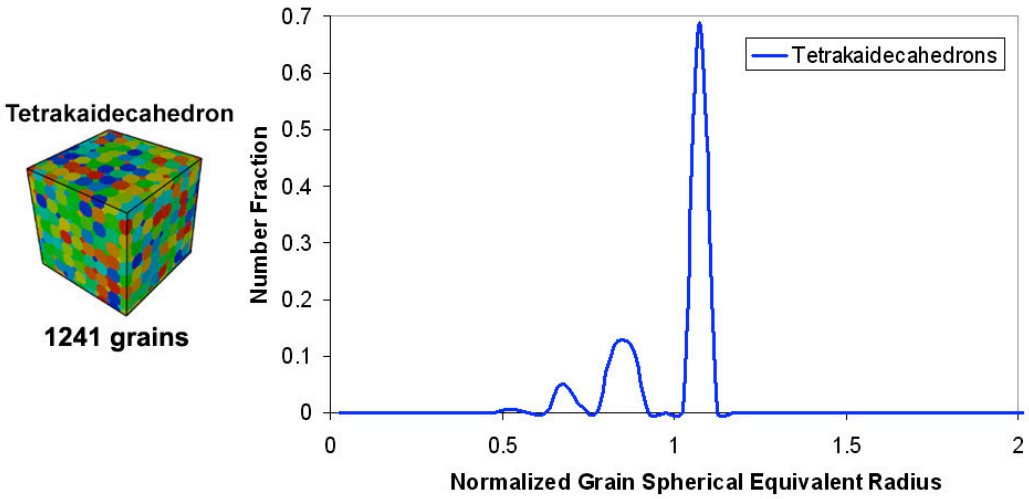

Figure 5.5 Grain structure (left) and the distribution of normalized spherical equivalent radius of the grains obtained from the tetrakaidecahedron structure (right). Although a regular grid of points was used to generate the microstructure, grains adjacent to the edge were truncated, giving rise to the small peaks below the average size.

Table 5.3 Detailed grain information about the tetrakaidecahedron structure shown in Fig. 5.5.

Structure	Dimensions (voxels)	Number of Grains	Maximum Grain Volume (voxels)	Average Grain Volume (voxels)	Average Grain Spherical Equiv. Radius (voxels)
Tetrakaidecahedron	200 x 200 x 200	1241	7858	6441	11.35

5.2 Experimentally Observed Structures

Three-dimensional microstructures can be obtained experimentally by using dual-beam systems that combine an orientation imaging microscope (OIM) with a focused ion beam (FIB) [56, 57, 71, 78, 113, 114]. After each layer of material is removed by the FIB, an electron back-scatter diffraction (EBSD) image is obtained on the surface of the material. The removal thickness is typically specified to be equal to the step size used in the EBSD data collection. The EBSD images are then reconstructed into a 3D digital structure with a registration method developed by Lee [115]. The registration method assumes that there is only translational misalignment between adjacent layers in the x and y directions. The alignment is then performed such that the total misorientation between adjacent layers is minimized. After the 3D structure is established, each grain is assigned a unique integer value for identification purposes.

Three experimentally reconstructed structures obtained from two different materials, Zirconia [71, 113], and Inconel 100 [57], were used in this study. The Zirconia structure and the smaller Inconel 100 structure are used in testing the orientation assignment algorithms, while the larger Inconel 100 structure is used in verifying the twin synthesizing algorithm. The structures are shown in Fig. 5.6 with detailed structure dimensions and grain size information given in Table 5.4. The large Inconel 100 structure contains approximately 5 times more grains than the smaller Inconel 100, and therefore produced a grain size distribution that appears much smoother than the distribution obtained from the smaller structure. As seen in the distributions of

normalized spherical equivalent grain size, the Inconel 100 structures have larger populations of smaller grain sizes that are attributed to the additional twin grains that are not found in the equiaxed grain structure of the Zirconia. Note that the grain sizes may be slightly biased towards the smaller grain size since all structures are non-periodic, and all surface grains are included in the distributions.

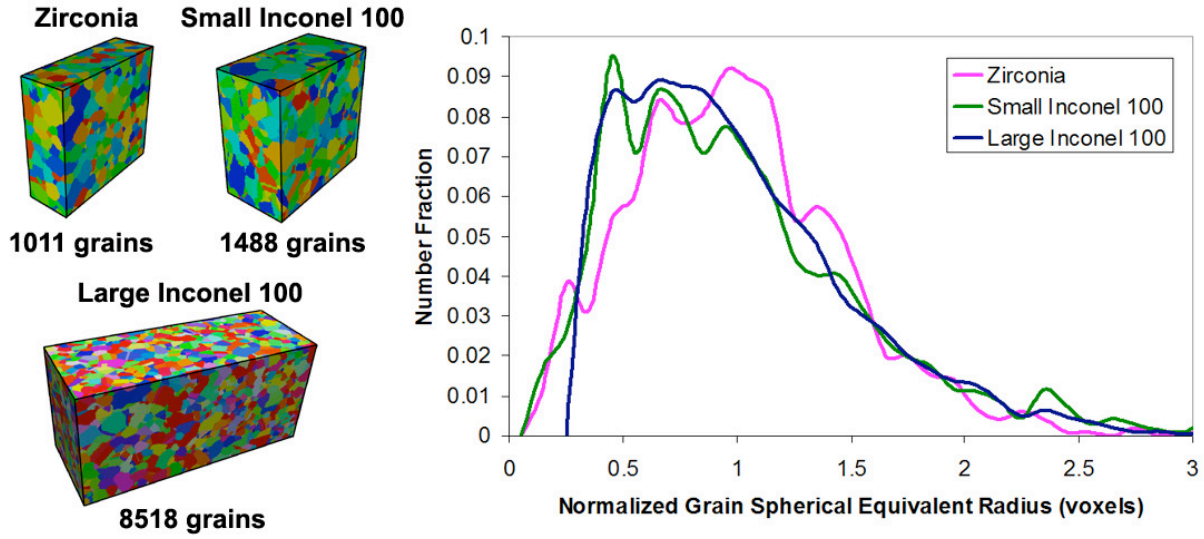

Figure 5.6 Grain structures (left) and the distributions of normalized spherical equivalent radius of the grains obtained from the reconstructed Zirconia [113] and the small and large Inconel 100 [57] structures (right).

Table 5.4 Detailed grain information about the reconstructed Zirconia and Inconel 100 structures.

Structure	Dimensions (voxels)	Number of Grains	Maximum Grain Volume (voxels)	Average Grain Volume (voxels)	Average Grain Spherical Equiv. radius (voxels)
Zirconia	150 x 140 x 50	1011	15,297	1053	5.30
Small Inconel 100	150 x 150 x 80	1488	26,900	1312	5.29
Large Inconel 100	389 x 146 x 184	8518	32,535	1227	5.41

Chapter 6 Digital Microstructure Characterization Techniques

After the digital microstructures are generated, the geometrical features of the microstructure must be quantified. The various methods used in this study to quantify the distribution of interface normals, Σ3 and twin boundary fractions, Σ3 and twin cluster distributions, grain size, twin width, and the twin density are presented here. In obtaining grain sizes, some researchers have either ignored the twins or presented both measurements with and without including the twins [91, 116]. For this purpose, a twin grain removal technique is presented for obtaining the grain sizes of the parent grains. The twin grain removal technique will also be used in this study for verifying the twin insertion algorithm.

6.1 Distribution of Interface Normals

To obtain the distribution of interface normals for the three-dimensional voxelized structures, a surface mesh must first be generated for the specified structure. For this purpose, the multi-material marching cubes algorithm was used to generate the initial surface mesh [117, 118]. The initial conformed surface mesh must be smoothed to remove any artifacts that may exist due to the voxelization or pixelation of the grain boundaries. The smoothing method imposed on the surface mesh is similar to the grain boundary reconstruction method used by the OIM software on the two-dimensional EBSD images, briefly described in Section 3.1.1. Instead of constraining the triple points, quadruple points are examined in the three-dimensional structure. Between any pair of quadruple points, the grain boundary line (a collection of all the triangle edges) is traced. Straight lines connecting the quadruple point and the midpoints of the connecting segments of the grain boundary line are then inserted. If the furthest perpendicular distance between the reconstructed straight line and the grain boundary line does not exceed a set

tolerance (0.7 voxels for this study), the straight line is accepted as the new boundary line. Once the smoothed conformed surface mesh is generated, interface normals can be calculated for every triangular element of the mesh. Each triangular area is then used for binning the corresponding misorientation and interface normal into the corresponding cell in the GBCD. The number of elements identified for each of the structures used in this study is given in Table 6.1.

Table 6.1 The number of nodes and triangles that resulted from generating surface meshes of the various structures.

Structure	Number of Nodes	Number of Triangles
M1	1 646 622	3 436 356
M2	882 904	1 899 378
M3	1 697 335	3 501 043
Plank	33 626	65 734
Tetrakaidecahedron	2 213 023	4 614 382
Zirconia	411 164	874 005
Small Inconel 100	690 652	1 473 903
Large Inconel 100	4 641 833	10 020 591

6.2 Σ3 and Twin Boundary Fractions

To quantify the number and area fractions of coherent and incoherent Σ3 grain boundaries, the conformed surface mesh is used to help classify the grain boundaries. Only the lattice misorientation across each triangular element of the mesh is needed for determining whether or not the Σ3 relationship exists. To determine the coherency of the triangular element, the misorientation axis from the minimal misorientation angle-axis relationship is rotated from crystal to sample reference frame using either one of the adjoining grain orientation matrices. The triangular element is considered to have a coherent Σ3 relationship if the angle between the misorientation axis and the interface normal is less than 15°. The area of the boundaries is then measured by summing the areas of the corresponding triangular elements. The number of coherent Σ3 boundaries is measured by counting the number of grain boundaries that have more than a threshold fraction (0.5 in this study) of the triangular elements classified with the coherent

Σ3 relationship. The discussion on choosing the correct threshold value for classifying the coherent Σ3 boundaries can be found in Section 10.2.1.

6.3 Σ3 and Twin Cluster Distributions

In correlating the connectivity of grain boundaries with the intergranular degradation behavior of materials, many researchers such as Basinger *et al.* [119], Frary *et al.* [120-122], Fullwood *et al.* [123], Gaudett *et al.* [124], Henrie *et al.* [19], Palumbo *et al.* [48], Schuh *et al.* [125, 126], and Wells *et al.* [127] have used bond percolation theory to identify clusters, where a cluster is defined as the length of connected degradation susceptible boundaries. The percolation threshold, the fraction of intergranular degradation resistant boundaries below which a cluster exists that spans the sample, is then often measured to determine whether a material is susceptible to intergranular degradation.

In this thesis, the site percolation theory is used to define clusters as the number of grains that are linked together through a certain boundary type, similar to the method used by Xia *et al.* [23]. Therefore, a Σ3 cluster consists of grains that are linked together through coherent or incoherent Σ3 boundaries, whereas a twin cluster consists of grains that are linked together only through coherent Σ3 grain boundaries. To characterize the Σ3 cluster distribution, the misorientation between the first grain and its neighbors are measured. If a Σ3 boundary exists between the first grain and a neighbor, the neighbor is added to the cluster. The misorientation between the newly added grain and all its corresponding neighbors is then measured and tested for the Σ3 relationship. The procedure is then repeated until no further Σ3 boundaries can be found next to the cluster. To characterize the twin cluster distribution, the list of coherent Σ3 boundaries obtained by performing the twin boundary fraction analysis is used. Since each grain

boundary corresponds to the interface between two adjacent grains, the uniquely assigned grain identification numbers are used to link the grains with coherent Σ3 boundaries together into clusters.

6.4 Grain Size

The grain size in any of the structures can be defined with either the grain volume or the spherical equivalent radius of the grain. The grain volume is calculated by summing up the number of voxels that make up the grain. The spherical equivalent radius takes the grain volume and calculates the radius assuming that the grain is a perfect sphere using,

$$radius = \sqrt[3]{\frac{3}{4\pi} Volume} \tag{6.1}$$

6.4.1 Twin Removal

In measuring grain sizes in FCC metals that contain annealing twins, when twins are included in the measurement, the average grain size is always smaller than when the twins are ignored [128]. On the planar orientation maps, the OIM software has the ability to exclude Σ3 boundaries from the grain size measurements by considering the twin and the parent together as one grain. The problem with using this technique is that the OIM software only uses the lattice misorientation to find the Σ3 boundaries. Therefore, all pairs of grains sharing a Σ3 boundary, regardless of the coherency of the boundary, will be merged together as one grain. The method used in this study observes the fully reconstructed 3D structures and only removes truly coherent Σ3 boundaries from the structures. Following the method outlined in Section 6.3 to identify twin clusters, the removal of the twin boundaries is simply performed by allowing the first grain to consume the remaining grains in the identified twin clusters. After the twin boundaries are

removed from the structure, random grain orientations are assigned such that any preferential texture that may be caused by the twin removal will be avoided.

6.5 Twin Density

Twin density is often measured by researchers as the number of twin boundaries intersected by a straight line on a two-dimensional planar section of the sample [89, 129-131]. In this study, the definition of twin density is changed to being the number of twins per parent grain. The modification to the twin density definition is necessary for the twin synthesizing algorithm to create statistics that match those observed in the experimental microstructures. The major challenge with the measurement of this type of twin density is that when more than one twin exists in the parent grain, it becomes very difficult to differentiate between the twins and the parent grain. The approach used to measure the number of twins per grain in this study is to identify the twin clusters in the structure. Since all the grains in the twin clusters are related through coherent $\Sigma 3$ boundaries, it is assumed that the twin cluster represents one parent grain that contains multiple twin grains.

Chapter 7 Texture Generation

7.1 Textures

In this section, the methods used for generating the <100>, <110>, and <111> fiber textures, creating the random texture, and extracting the rolling texture from an experimentally observed rolled structure are discussed.

7.1.1 Fiber Textures

The model used in this study for generating axial fiber textures was adopted from the work of Garbacz and Grabski [132, 133], where it is assumed that deviations from the ideal <hkl> direction can be described by the normal distribution. As seen in Fig. 7.1a, any specified <h'k'l'> direction will form a small angle φ with the ideal <hkl> direction. This allowable angle of deviation is then specified with the probability density function for a normal distribution,

$$p(\varphi) = \frac{1}{\sigma\sqrt{2\pi}} \exp\left(-\frac{(\varphi - \ )^2}{2\sigma^2} \right) \tag{7.1}$$

where is the mean, and σ is the standard deviation [134]. In generating the fiber textures, the mean is always set as zero, so that the standard deviation specifies the sharpness of the fiber texture or more simply, the allowable angle of deviation, as seen in Fig. 7.1b. In terms of Euler angle representation, the Euler angles that will satisfy the deviation is given in Table 7.1, with deviations of the Euler angles satisfying the relation given by,

$$\Delta\Phi + \Delta\phi_2 \leq 15 \tag{7.2}$$

where $\Delta\Phi$ and $\Delta\phi_2$ can be positive or negative values [132].

Table 7.1 Euler angles for calculating the three fiber textures <100>, <110>, and <111>.

Euler Angles	<100>	<110>	<111>
ϕ_1	0° – 360°	0° – 360°	0° – 360°
Φ	0° + $\Delta\Phi$	90° + $\Delta\Phi$	54.7° + $\Delta\Phi$
ϕ_2	0° + $\Delta\phi_2$	45° + $\Delta\phi_2$	45° + $\Delta\phi_2$

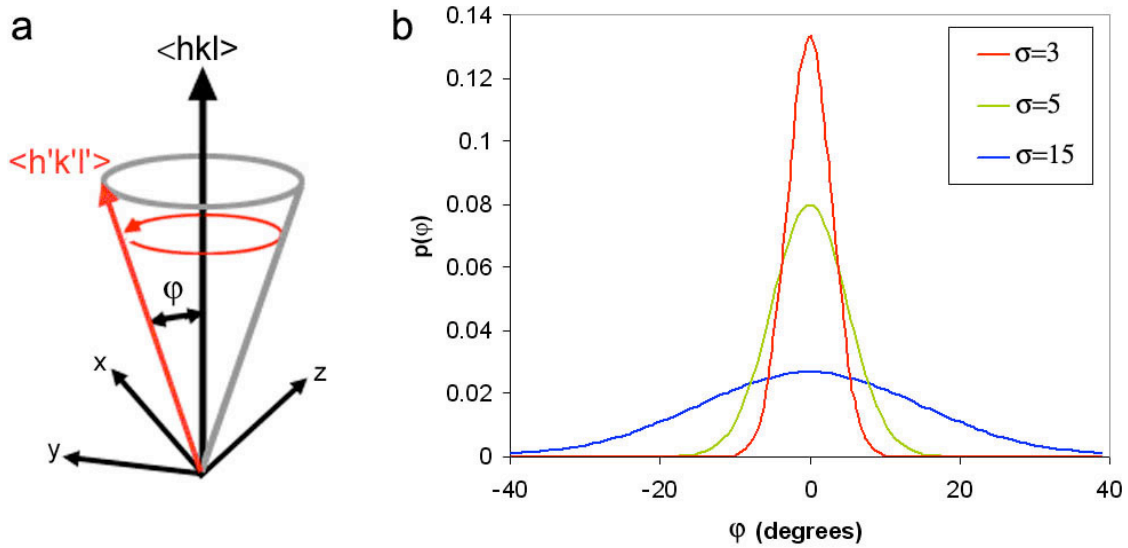

Figure 7.1 (a) Shows the method used to specify the allowable angle of deviation from the ideal <hkl> texture, and (b) shows the three probability density functions with varying sharpness of texture as σ varies from 3 to 15 (redrawn from [133]).

The pole figures shown in Fig. 7.2 were plotted with a list of 10,000 orientations generated with =0° and σ=5° for each corresponding fiber texture. The highest peak occurring at the center of each pole figure corresponds to each fiber texture where all the grain orientations happen to have their major axis aligned parallel with the corresponding pole. For example, the peak at the center of the (100) pole figure for the <100> fiber texture indicates that the <100> crystal direction is aligned parallel with the <100> sample direction. The ring patterns seen in the other pole figures are created from rotating the crystal axis 360° around the specified fiber axis.

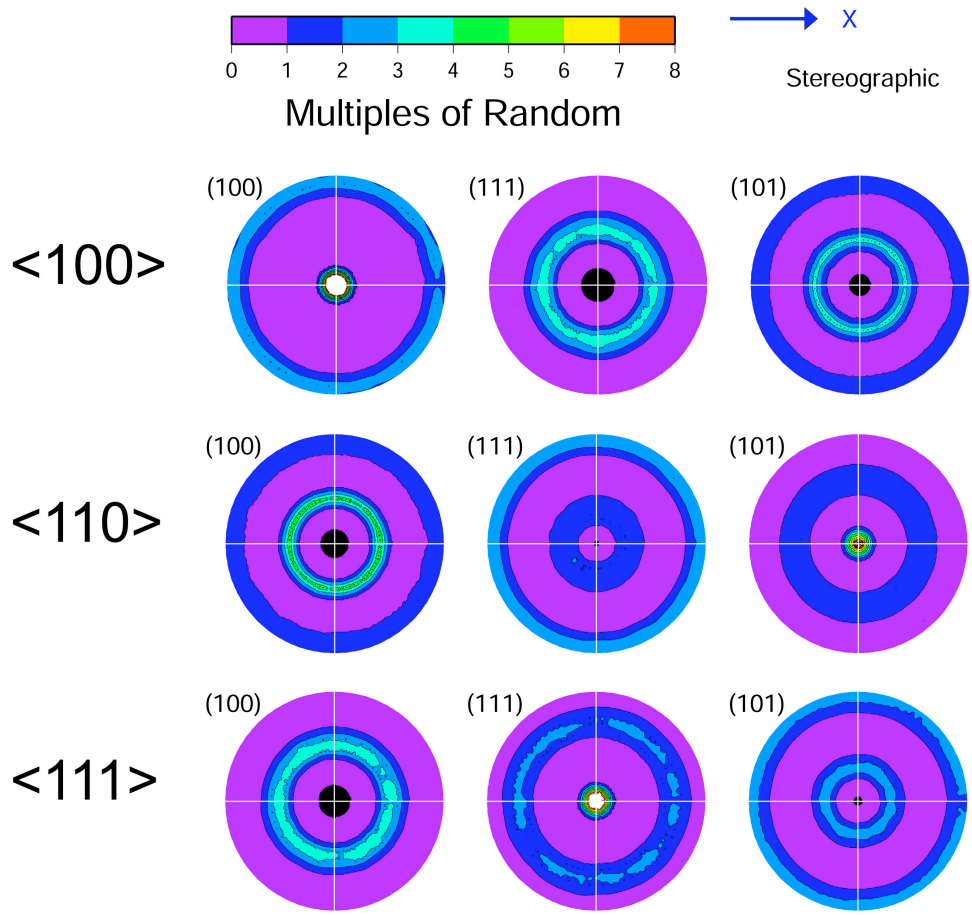

Figure 7.2 Pole figures showing the <100>, <110>, and <111> fiber textures. Note that white is off-scale in the positive direction (MRD>8) and black is off-scale in the negative direction.

7.1.2 Random Textures

To generate a random texture, the list of Euler angles simply need to be randomly assigned. In the Euler angle space, this means that the angles ϕ_1 and ϕ_2 are chosen randomly within the range of 0 to 2π and the cosine of the second angle is chosen randomly within the range -1 to +1. The most common pseudo-random number generator algorithm, the linear congruential generator, is used for this purpose [135]. Since the list of random orientations was generated as a list of three Euler angles, the list can be treated as both orientation and misorientation. As seen in Fig. 7.3, when the list of random Euler angles is plotted with either an orientation distribution function (OD) plot or misorientation distribution function (MD) plot, a

random distribution or 1 MRD is observed. The texture components for the random texture are also calculated and shown in Table 7.2. The number fractions of the various texture components calculated with the random texture are commonly used as a basis of comparison with texture components calculated with other textures.

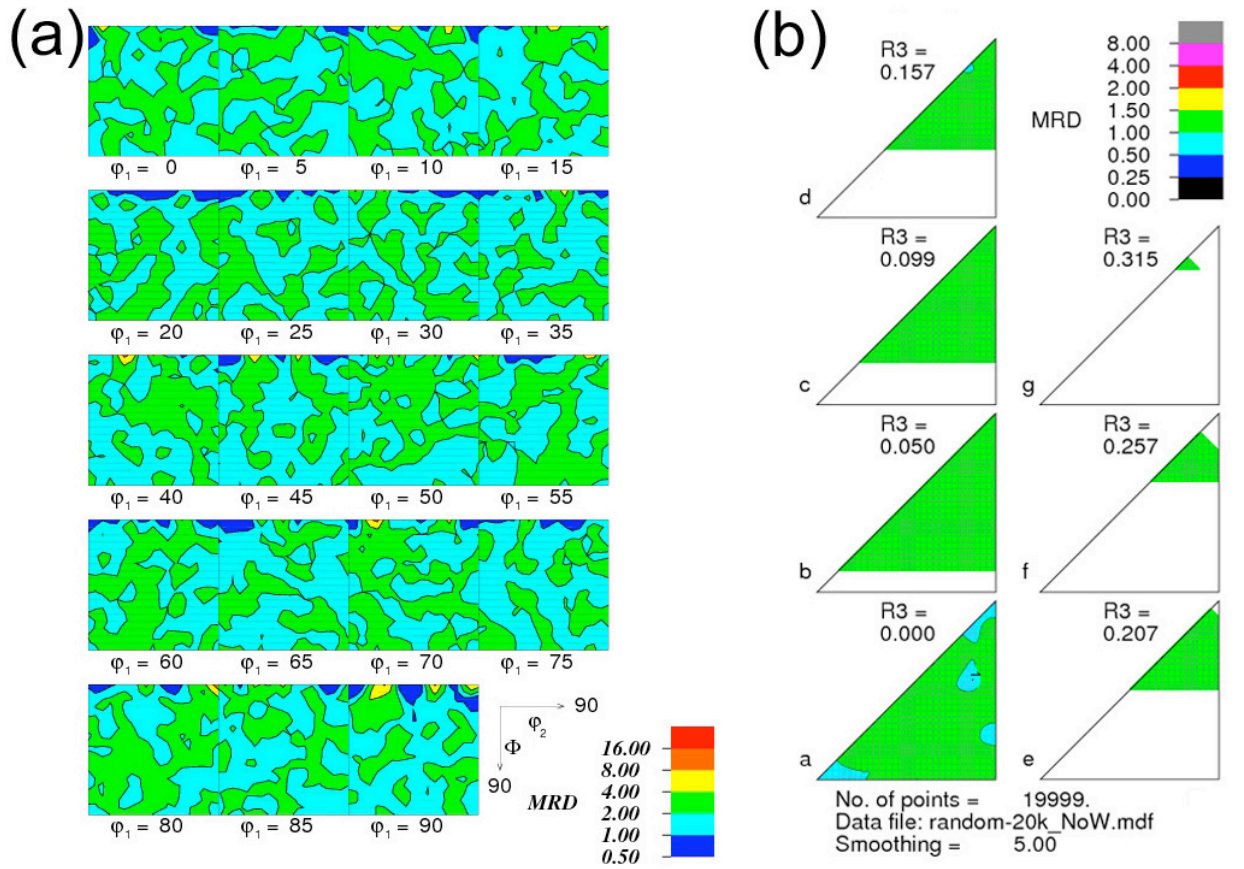

Figure 7.3 Random texture shown with (a) OD plots created with slices of ϕ_1 in Euler angle space, and (b) MD plots with slices of R_3 in Rodrigues-Frank misorientation space.

Table 7.2 Number fraction of texture components observed in random texture with a capture radius of 15°.

Texture Component	Cube	Goss	S	Brass	Copper
Volume Percent (%)	0.005	2.8	44.8	26.4	19.9

7.1.3 Experimental Textures

The rolling texture used in this study was obtained from an EBSD map of rolled commercial-purity copper. The inverse pole figure map and pole figures obtained from the EBSD map are shown in Fig. 7.4. As seen in the inverse pole figure map, a rolled structure is clearly observed, while in the pole figures, the distinct pattern generated by the rolling texture is seen. The OD and MD extracted from the rolled copper using the OIM software are plotted in Euler angle space and Rodrigues-Frank space in Fig. 7.5. The highest intensity found in the pole figures and Euler angle space plots are 8 MRD and 16 MRD respectively. The difference in maximum intensity values is due to the fact that intensity on the pole figure is equivalent to integrating along a path in Euler angle space [33]. After normalization, the pole figure intensities are lower than the intensities found in the Euler angle space plots because one has, in effect, averaged the ODF intensities along the integration path. In Fig. 7.5b, the MD of the rolled copper shows somewhat higher than random frequencies of low angle grain boundaries and misorientations that are close to the $\Sigma 3$ relationship.

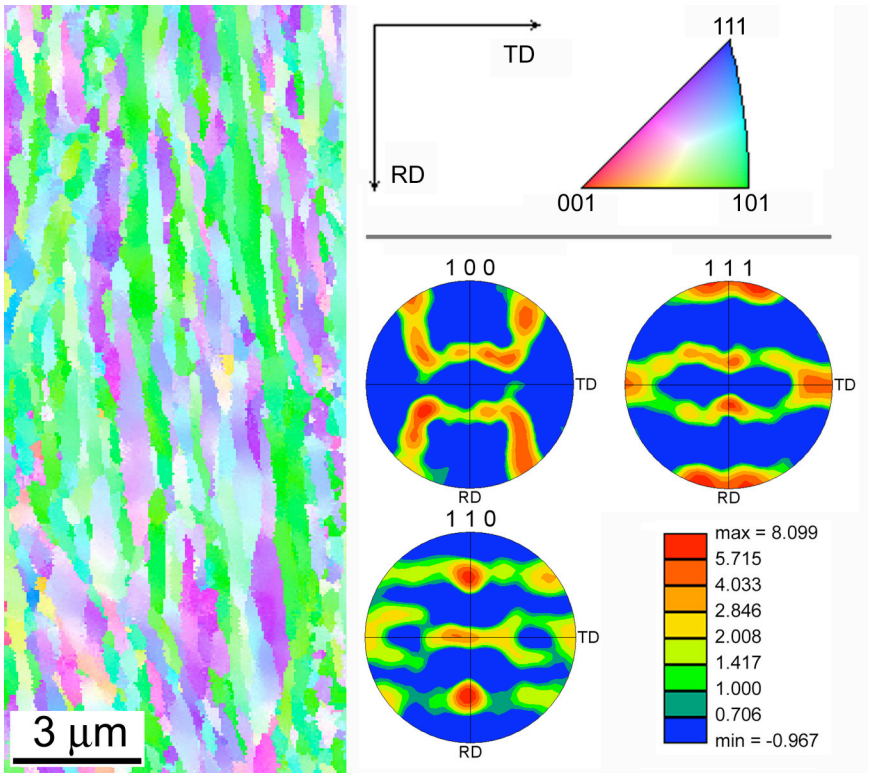

Figure 7.4 (Left) Inverse pole figure map, and (lower right) the pole figures obtained from EBSD scan collected from rolled commercial-purity copper.

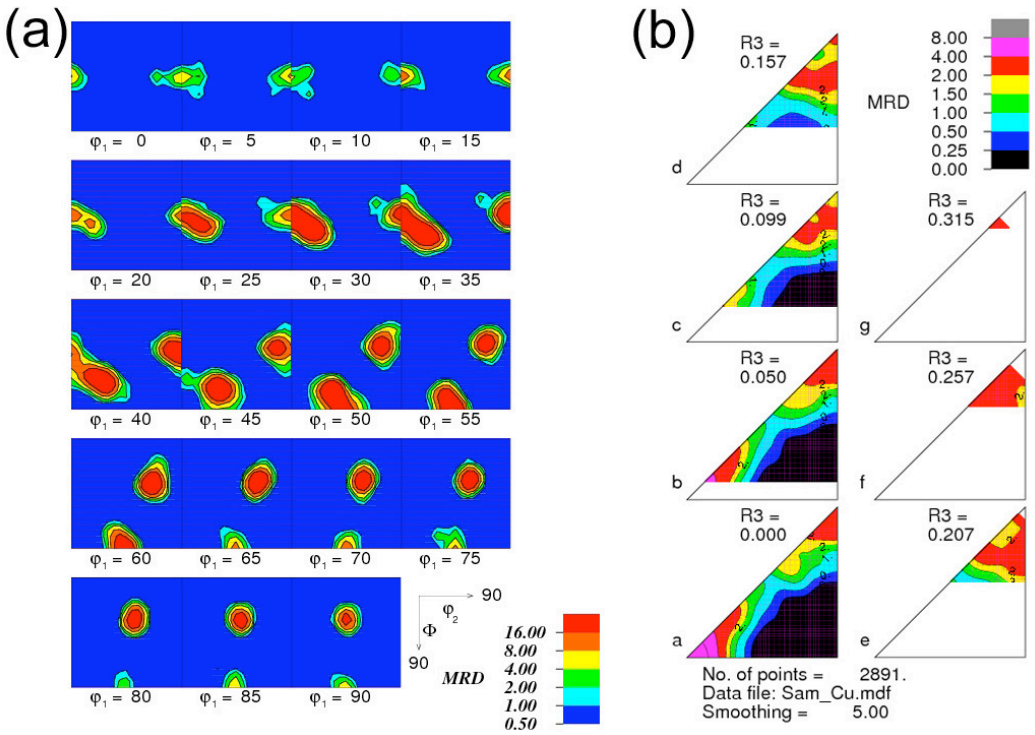

Figure 7.5 (a) OD plots created with slices of ϕ_1 in Euler angle space showing the grain orientations, and (b) MD plots with slices of R_3 in Rodrigues-Frank space showing the misorientations observed in rolled commercial-purity copper.

7.2 Misorientation Distributions

The method used to generate a list of CSL boundary types and the various techniques to extract GBCD from experimentally observed data sets are presented in this section.

7.2.1 CSL Boundary Lattice Misorientations

As previously shown in Fig. 2.6 of Section 2.1.4, CSL boundary relationships appear as unique positions in the Rodrigues-Frank fundamental zone. A similar set of singular points can be located in the Euler space fundamental zone. However, due to the asymmetric nature of the fundamental zone [136] in Euler space, the larger domain of all three Euler angles ranging from 0 to $\frac{\pi}{2}$ is typically used instead, which contains 36 copies of the fundamental zone. The algorithm for generating the list of sigma boundary relationships searches the domain of the Euler angle space in 0.1 radian steps to identify all the CSL relationships. In using Brandon's criterion for classifying the CSL relationships, any one specified misorientation could intersect with more than one CSL relationship. Therefore, the angle of deviation between the specified misorientation and all CSL relationships ($\Sigma \leq 49$) must be calculated to ensure that the misorientation is properly labeled with the closest CSL sigma value. Two lists of CSL boundaries are plotted in Fig. 7.6, the first list consists of misorientations with a $\Sigma 1$ relationship, and the other consists of misorientations with $\Sigma 1$, 3, and 7 relationships. As a consequence of the angle of deviation allowed by Brandon's criterion, the location of each CSL relationship is no longer a singular point. For example, the $\Sigma 3$ peak can be seen through several sections in Rodrigues-Frank space after using 5° of Gaussian smoothing. As mentioned in Section 3.1.1, the grain boundaries that have $\Sigma 1$, 3, and 7 CSL relationships are the boundaries of interest for improving the intergranular corrosion resistance of Aluminum.

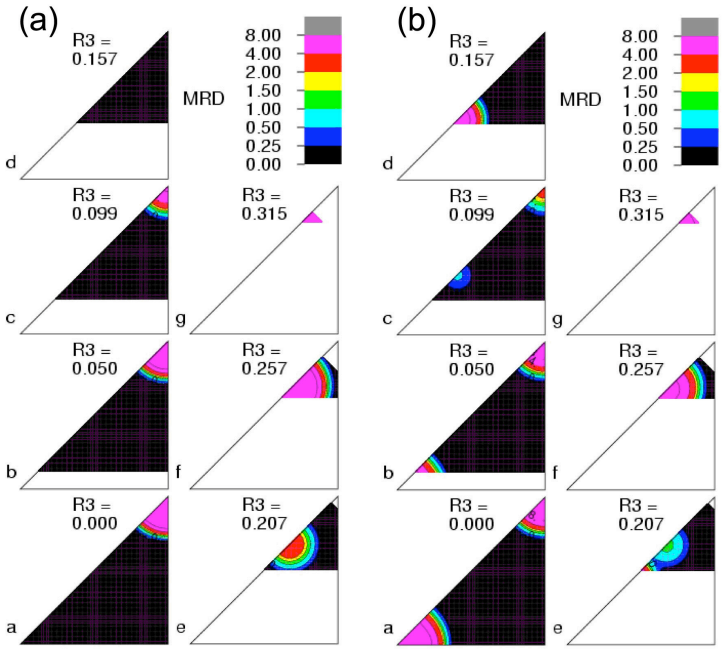

Figure 7.6 MD plots in Rodrigues-Frank space with (a) showing boundaries limited to the Σ3 relationship, and (b) showing boundaries with Σ1, 3, and 7 relationships. A reference for the ideal CSL positions can be found in Fig. 2.6.

7.2.2 Stereological Methods in Obtaining GBCD

A stereological approach can be used to estimate the distribution of grain boundary types based on the observation of a planar section [137]. As mentioned before, the grain boundary character distribution is parameterized with the three Euler angles that represent the lattice misorientation, and the two spherical angles that represent the grain boundary normal. In observing a planar section, only the grain boundary trace and the lattice misorientation are known. Even though the exact grain boundary inclination is unknown, the grain boundary plane must lie somewhere within the zone of the grain boundary trace. Hence, for each observed length of grain boundary trace, every possible observed plane within the zone of the specified grain boundary trace is added to the GBCD. After a large set of boundary traces have been observed, the relative areas of the correct grain boundary orientations will be larger than the incorrectly observed orientations. In this analysis, it is assumed that all of the bicrystals with a

similar misorientation are randomly oriented with respect to the plane of observation and that a sufficient number are sampled. For cubic materials, not only are $5x10^4$ boundary traces needed, but the material must be relatively untextured for this method to give correct approximations of the grain boundary distributions. Further detailed description of the stereological method for obtaining the full five-parameter GBCD from planar sections is given by Saylor *et al.* [137].

7.2.3 Experimental GBCD

Experimental GBCDs can be measured from one of the reconstructed microstructures that were collected from the dual beam FIB-SEM. Details about the meshing of the structure to obtain the interface normals were given in Section 6.1. Since the binning of the GBCD requires both the misorientation information as well as the interface normals, caution is required to treat the combination of the two types of information. In experimentally obtaining the crystallographic information, the reference frame used to collect the orientation information is not always identical to the sample reference frame. In such a case, the interface normals must be rotated such that both the orientation and sample references frames coincide with each other prior to being binned into the GBCD. For example, under default settings, experimental interface normals observed with the OIM system made by EDAX, Inc. must be transformed with Euler angles $\phi_1 = -90°$, $\Phi=180°$, and $\phi_2=0°$ before being binned into the GBCD.

Chapter 8 Orientation Assignment Algorithms

8.1 Algorithms for Orientation Assignment

Two different versions of the orientation assignment algorithms are presented here, the MD version (3 parameters) and the GBCD version (5 parameters). The main difference between the two versions of the code is that in the MD version, only the distribution of lattice misorientations is used, whereas in the GBCD version, the distributions of both the lattice misorientations and the interface normals are used in assigning the grain orientations in the specified microstructure.

Given the geometric configuration of the grains in a specified microstructure, the grain information must first be extracted to simplify the orientation assignment procedure. The only grain information required by the MD version of the orientation assignment program is the grain volume, the grain boundary area between each pair of adjacent grains, and the neighbor information for each grain. The GBCD version of the program requires additional information about the interface normals for each grain boundary. The grain volume is calculated as the total number of voxels that make up each grain. To obtain the neighbor information, the nearest neighbor of each voxel is examined to determine both the identification number of the neighbor and the boundary area shared with that neighbor. As mentioned before, the interface normals are extracted from meshing the structure and calculating the normal vectors corresponding to the triangulated surfaces. The grain volumes and grain boundary areas are used to calculate the volume-weighted orientation distribution and area-weighted misorientation distribution or grain boundary character distribution respectively.

Once the list of grain information is obtained, orientations are then assigned such that the distributions of grain orientations and grain boundary misorientations will match the target

distributions. As previously stated, the homochoric space is convenient for representing the distributions of grain orientations because it can be easily divided into equal volume elements. However, while the distribution is tracked in homochoric space, each individual grain orientation is tracked with the Rodrigues-Frank vectors assigned to the grains. To specify the target grain orientation distribution, crystallographic information can either be extracted from orientation maps or computer generated with the methods mentioned before. In either case, binning of the orientation distribution is accomplished by adding the number fraction of each orientation observed into the appropriate cell in homochoric space. To specify the target misorientation distribution for the MD version of the algorithm, the same procedure as specifying the target orientation distribution is used. To specify the target GBCD, the five parameter boundary information can either be calculated with stereological methods from an orientation map, or extracted from an experimentally reconstructed 3D data set, as described in Sections 7.2.2-7.2.3.

After the target distributions are specified, grain orientations are assigned to the specified microstructure using simulated annealing, such that the output and target distributions will match. The simulated annealing method has been shown by Miodownik *et al.* [138] to be an efficient Monte Carlo algorithm that assigns appropriate distributions of grain orientations and misorientations to three-dimensional microstructures. It should be noted that this simulation method does not allow any spread or deviation in orientation within a single grain, thus only one orientation is assigned to each grain. Also, the geometric information of the grains remains constant throughout the simulated annealing procedure. The algorithm can initiate the simulated annealing procedure by assigning either random orientations or grain orientations that were based on the target orientation distribution to the grains. Next, both the grain orientation distribution and either the misorientation distribution or grain boundary character distribution are

calculated and compared to the target distributions. Each observed grain orientation and misorientation are binned into the corresponding cells in homochoric space based on the volume fraction of the grain and area fraction of the boundary respectively. The grain boundary character distribution is calculated and binned with the same method mentioned in Section 2.2.2. The error value between the proposed and target distributions are then calculated with either

$$\text{error} = \text{OD\_weighting}\left(\sum_{i}^{N_i} (OD_i^{\text{proposed}} - OD_i^{\text{target}})^2 \right) + \text{MD\_weighting}\left(\sum_{j}^{Nj} (MD_j^{\text{proposed}} - MD_j^{\text{target}})^2 \right) \quad (8.1)$$

or

$$\text{error} = \text{O}D\text{\_weighting}\left(\sum_{i}^{Ni} \left(OD_i^{\text{proposed}} - OD_i^{\text{target}}\right)^2 \right) + \text{GBCD\_weighting}\left(\sum_{k}^{CD} \sum_{l}^{CD} \sum_{m}^{CD} \sum_{n}^{CD2} \sum_{o}^{4CD2} \left(GBCD_{klmno}^{proposed} - GBCD_{klmno}^{proposed}\right)^2 \right) \quad (8.2)$$

where index *i* sums over the homochoric cells for orientation, index *j* sums over the homochoric cells for misorientation, indexes *k*, *l*, and *m* sum over the GBCD cells for Euler angles, and indexes *n* and *o* sum over the GBCD cells for boundary normals. The total number of cells in homochoric space is designated with Ni and Nj, the total number of cells in each direction in Euler angle space is designated with *CD*, and the total number of cells representing the interface normal is given by *CD2* and *4CD2*. In the parameterization of the interface normal, *CD2* relates to the latitude angle, which ranges from 0 to 90°, while *4CD2* relates to the longitude angle, which ranges from 0 to 360°. The variables OD_weighting, MD_weighting, and GBCD_weighting enable the user of the simulated annealing algorithm to vary the closeness of fitting to either the target OD or to the target MD (or target GBCD). These variables can be specified with the weight variable, which ranges from 0 to infinity, with,

$$\text{OD\_weighting} = 2 - \frac{2}{\text{weight} + 1} \tag{8.3}$$

$$\text{MD\_weighting} = \frac{2}{\text{weight} + 1} \text{ or} \tag{8.4a}$$

$$\text{MD\_weighting} = \frac{2}{6(\text{weight} + 1)} \tag{8.4b}$$

$$\text{GBCD\_weighting} = \frac{2}{\text{weight} + 1} \times 10^{-13} \tag{8.5}$$

The option of dividing the MD_weighting by 6 is motivated by the fact that the fundamental zone for misorientations is $\frac{1}{6}$ the size of the fundamental zone for orientations. Therefore, for the same cell or bin size in homochoric space, only $\frac{1}{6}$ of the cells are used to bin the misorientation distribution. The division by 6 offsets the bias of it being easier to achieve the same error between the fitted and target MD distributions as a consequence of the smaller fundamental zone. Due to the differences between using the homochoric space and the Euler angle space for binning the OD and GBCD, the GBCD_weighting has been scaled by an additional 10^{-13} to ensure that the error values obtained from the OD and GBCD are on a similar magnitude. In measuring the errors contributed by the target and output ODs, volume fractions of grain orientations are binned into 1000 bins in homochoric space. On the other hand, to measure the error contributed by the target and output GBCDs, grain boundary areas are binned into 236,196 bins (using 10° bins) in the Euler angle space. For example, a grain boundary area of approximately 960,000 voxels was observed in the M1 structure. Since the difference between the target and output GBCD is measured as the squared difference in boundary areas, this difference must be scaled by a factor of 10^{-11} to allow reasonable comparisons with the difference in volume fractions between the target and output OD. However, because there are

approximately 100 times more bins in measuring the GBCD as compared to the OD, an additional scaling factor of 10^{-2} must be included, and hence the scaling factor of 10^{-13} was included in the GBCD_weighting.

After the error value is computed at each step, the algorithm evolves the proposed distributions towards the target distributions by one of two evolution operations. The algorithm can either choose a grain at random and assign another orientation to the grain, or choose two grains at random and swap their orientations. Once either of the two operations is selected, the probability that the evolution step is accepted is calculated with,

$$P = \begin{pmatrix} 1 & error \leq 0 \\ e^{-\frac{error}{T}} & error > 0 \end{pmatrix} \tag{8.6}$$

where T is the annealing temperature. Simply, when the error of the system is decreased, the evolution step is always accepted, whereas when the error of the system is increased, the evolution step is either accepted or rejected based on the value of the annealing temperature. The annealing schedule then consists of decreasing the annealing temperature for a fixed number of annealing steps until the error of the system has decreased significantly. To complete one annealing step at a specified annealing temperature, 10N successful evolution steps or 100N attempts of evolution must be performed, where N is the total number of grains in the specified microstructure. After an annealing step is completed, the annealing temperature is decreased by 20%, for the next annealing step to proceed. The default settings for the algorithm specify the initial annealing temperature to be 0.0001 and the number of annealing steps to be 50, which is equivalent to allowing the annealing temperature to decrease 49 times.

8.2 Verification of the Algorithm – MD Version

To verify that the MD version of the algorithm is indeed assigning the correct OD and MD to the structure, the rolling texture components and the CSL boundary distributions were tracked as OD_weighting and MD_weighting were changed following Equations 8.3 and 8.4a. The results shown in Fig. 8.1 were obtained by initiating with random grain orientations, and performing the grain orientation assignment on the M1 structure with the target OD being rolling texture, and the target MD being the list of Σ1, 3, and 7 relationships. As seen in Fig. 8.1A, as OD_weighting increases, the volume fraction of the texture components in the structure quickly approaches that of the target volume fractions (denoted by the straight lines across the graph). It appears that an OD_weighting of approximately 1.3 is sufficient to match the output and target textures with the total difference in volume fractions of texture components, listed in Fig. 8.1, reduced from 0.82 to 0.09. For the area fractions of CSL boundary plot shown in Fig. 8.1B, the maximum fraction of CSL boundaries is achieved with an MD_weighting value as low as approximately 0.5. It should be noted that the target MD cannot be fully matched because it would require the grain boundary network to be composed entirely of only boundaries that have Σ1, 3, or 7 relationships. Therefore, Fig. 8.1B not only shows that an MD_weighting of only 0.5 is sufficient, but also that the maximum area fractions of the Σ1, 3, and 7 boundaries that are possible with rolling texture in structure M1 are 0.27, 0.22, and 0.20 respectively.

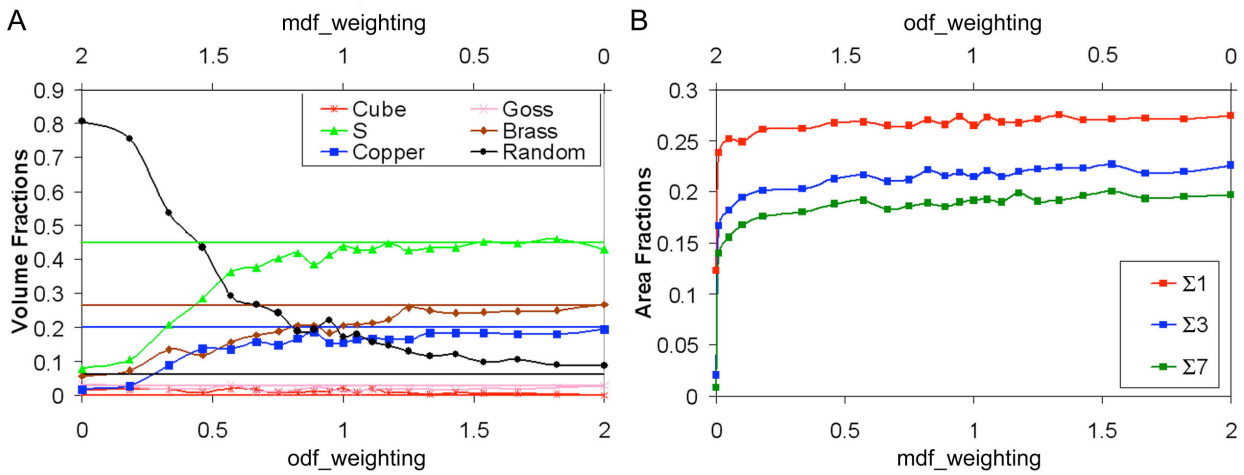

Figure 8.1 (A) Volume fractions of texture components plotted against OD_weighting and MD_weighting that shows the results obtained from using rolling texture as the target OD. The target texture components are drawn as straight lines across the plot. (B) Area fractions of the sigma boundaries plotted against MD_weighting and OD_weighting showing the results obtained from using the list of Σ1, 3, and 7 grain boundary relationships as the target MD.

8.3 Verification of the Algorithm – GBCD Version

To verify that the GBCD version of the algorithm is indeed matching the target OD and GBCD, orientation assignment using rolling texture as the target OD and the GBCD obtained from a commercially pure nickel sample [139] as the target GBCD was performed on the M1 structure. The error value as grain orientations were assigned to the M1 structure is shown in Fig. 8.2. Despite the relatively high error value that remained at the termination of the algorithm, Fig. 8.2 indicates that further iterations of the algorithm will not greatly improve the fit between the target and output orientation distributions and GBCDs. The target and output orientation distribution plots are shown in Fig. 8.3. As seen in Fig. 8.3, the grain orientation assignment algorithm was not able to maintain the rolling texture as both the OD and GBCD was simultaneously matched. The target and output GBCD plots are shown in Fig. 8.4. As seen in Fig. 8.4b, 27MRD of coherent Σ3 boundaries was observed in the output GBCD. It should be noted that the M1 structure does not contain any twin grains, and therefore will not be possible for the output GBCD to achieve 1600 MRD observed at the coherent twin location in the target

GBCD. An interesting feature observed in Fig. 8.4 is that despite the high MRD value for the coherent Σ3 boundaries, the preferential boundary orientations of the Σ9 and Σ27a boundaries observed in the target GBCD were still matched by the output GBCD. Even though the output orientation distribution deviated from the target orientation distribution, it is still clear that the GBCD version of the orientation assignment algorithm was able to successfully match the GBCD as closely as possible after performing 230,000 iterations, which took approximately 6 days.

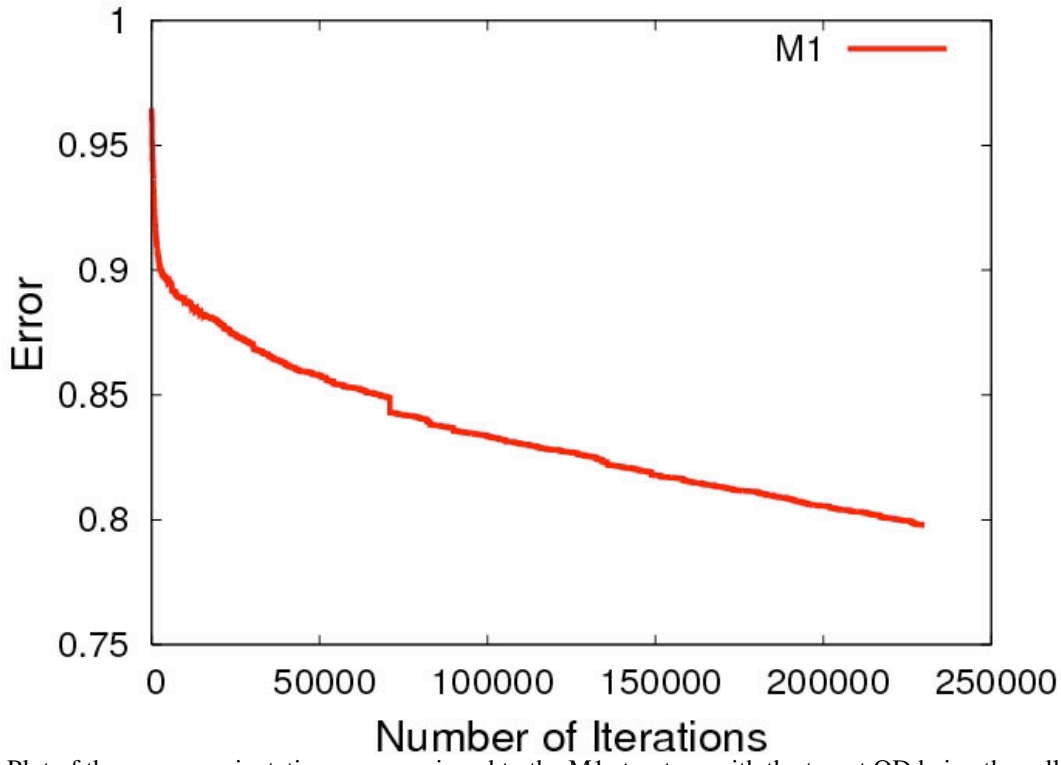

Figure 8.2 Plot of the error as orientations were assigned to the M1 structure with the target OD being the rolling texture, and target GBCD obtained from a nickel sample that contains annealing twins.

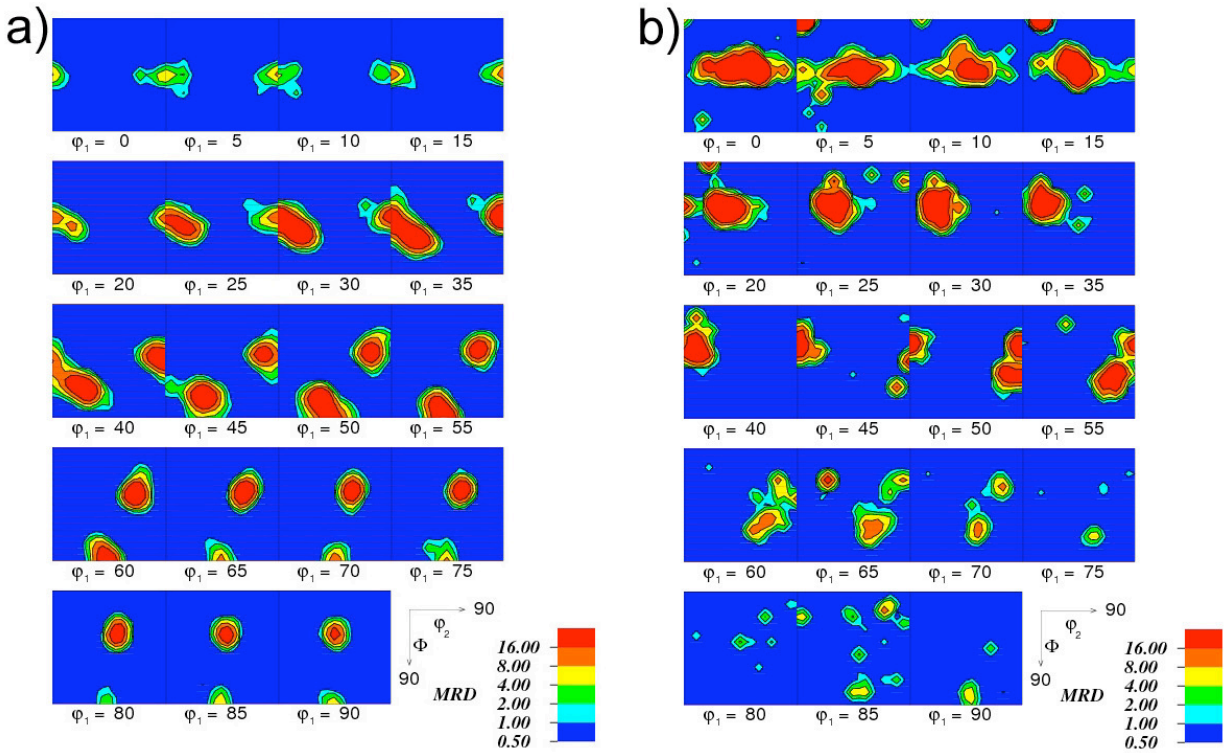

Figure 8.3 Euler angle plots showing the (a) target OD, rolling texture obtained from a rolled commercially pure copper, and (b) assigned OD obtained after performing orientation assignment with the GBCD version of the algorithm.

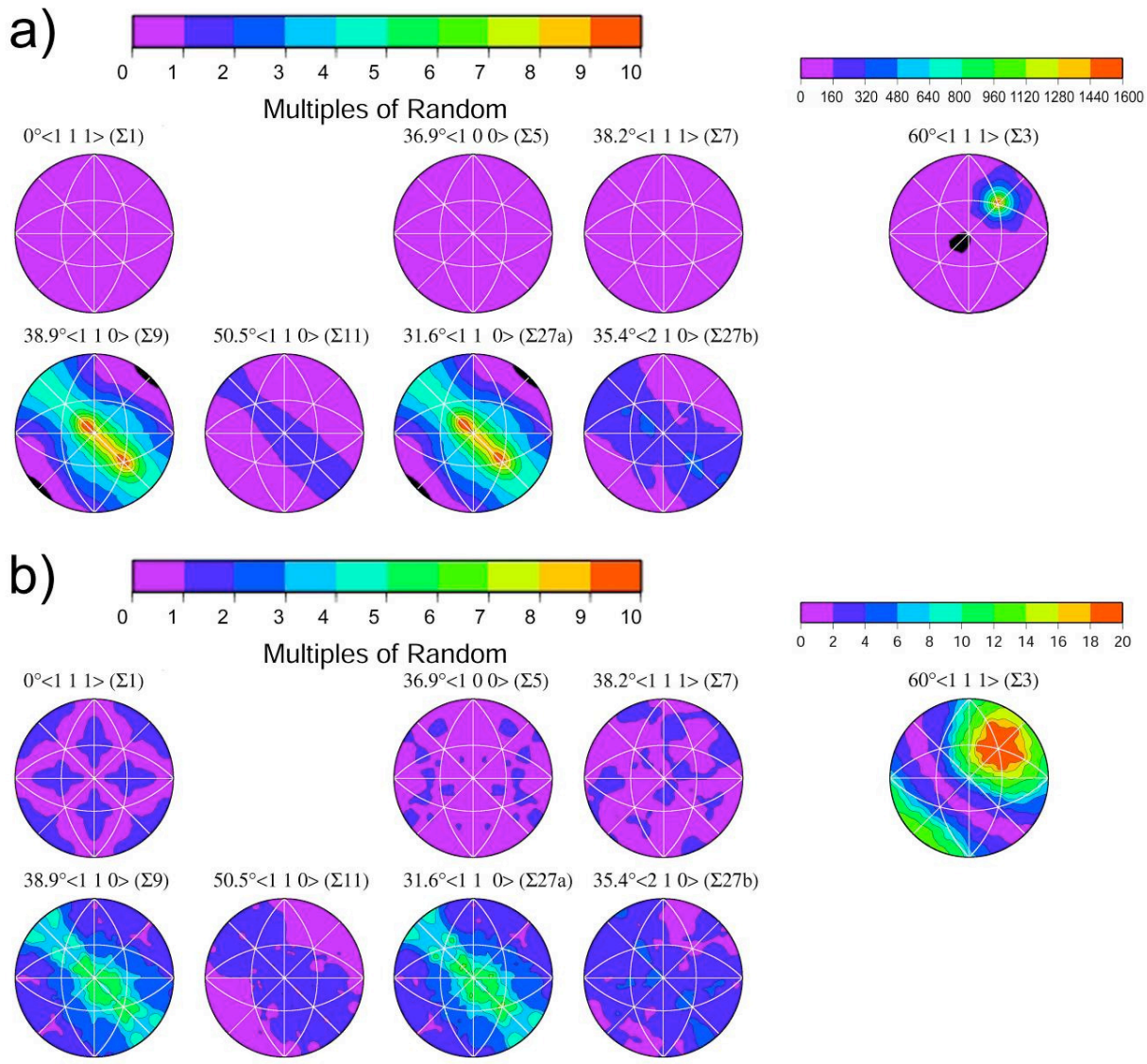

Figure 8.4 (a) Target GBCD plots measured from a commercially pure nickel sample, and (b) output GBCD plots after performing the GBCD version of the grain assignment algorithm on the M1 structure.

8.4 Sensitivity of Simulation Variables – MD Version

The effects of the different simulation variables are explored in the following sections, which includes the OD_weighting and MD_weighting variables used in calculating the system error, the choice for initial grain orientations, grain orientation evolution mechanism, the simulated annealing temperature, and the number of annealing steps. With the exception of the OD_weighting and MD_weighting sensitivity analysis, all structures used in the sensitivity

studies yield very similar results with common characteristics that are shown in the plots. Therefore, only results obtained from assigning grain orientations for the M1 structure are shown for those studies. Unless otherwise noted, all orientation assignments were performed under the default settings of the initial annealing temperature to be 0.0001, the number of annealing steps to be 50, and using only Equation 8.4a to calculate the MD_weighting. For each of the graphs displayed in this section, each point in the plots represents a separate simulation run that was produced with different weight values that range from 0 to infinity. Therefore, even though trends can be seen in the plots, each data point on the graphs is completely independent of any of the other data points.

8.4.1 Weighting for OD and MD

The different weighting of the OD_weighting and MD_weighting parameters for the simulated annealing procedure described in Section 8.1 is explored here. The results shown in Fig. 8.5 and Table 8.2 were obtained by performing the grain orientation assignments on all the synthetic microstructures, the experimental Zirconia, and the small Inconel 100 structure, described in Chapter 5, using both Equations 8.4a and 8.4b to calculate the MD_weighting as weight is varied from 0 to infinity. The top plot of Fig. 8.5 shows the output results on a semi-log scale. The semi-log plot was chosen for its suitability to the results, and was generated by calculating the root mean square difference between the target and output distributions in homochoric space for OD and MD. The colored solid lines found in the semi-log plot are drawn with the RMS OD and MD differences summing to a constant total error. For each solid line, the constant total error value is arbitrarily adjusted until the first data point of the corresponding structure intersects with the solid lines. The constant total error value used for constructing each solid line is given in Table 8.1. The points of intersection between the data points and the

colored solid lines are the points at which the best combination of OD_weighting and MD_weighting is found for each corresponding structure.

Table 8.1 Total constant values used to draw the solid colored lines shown in the semi-log plot of Fig. 8.5.

Structure	M1	M2	M3	Zirconia	IN100	Plank	Tetrakaidecahedron
Constant total error	0.186	0.200	0.157	0.187	0.173	0.040	0.122

The letter designations for each pair of the Euler angle and Rodrigues-Frank plots matches with the letters marked on the semi-log plot in Fig. 8.5. The letter designations of a-d indicate the RMS OD and MD differences that resulted from using OD_weighting values of 0, 0.67, 1.82, and 1.99, and MD_weighting values of 2, 0.22, 0.031, and 0.00085 respectively. As can be seen from inspecting the Euler angle plots from (a) to (d), the output orientation distribution approaches the target distribution as OD_weighting increases. From observing the Rodrigues-Frank plots, as the MD_weighting decreases, the misorientation distribution moves away from the target distribution.

In the top plot of Fig. 8.5, the lower right portion of any data set is the smallest possible difference that can be achieved between the output and the specified target orientation distribution. The data point that lies farthest right in the plot correspond to results obtained from using weight values close to infinity, in other words, when only the OD was used to calculate the error function. On the other hand, the data points that have the highest RMS OD differences were obtained with weight values close to 0, which corresponds to using only the MD to calculate the error function. However, the most interesting observation is that even when only MD was used to calculate the error function, the lowest RMS MD difference was not achieved. This is an indication that when a weak texture is present, fewer re-orientation steps are needed for the orientation assignment algorithm to match the target MD. The algorithm was not able to

reach the most optimum OD and MD match between the target and output distributions because all simulations were performed with a constant number of annealing steps. If more annealing steps were to be included for the OD_weighting = 0 simulations, the RMS MD difference would be expected to decrease while the RMS OD difference would remain approximately constant. The black line in the graph traces the line that defines the locus of points for which the RMS OD difference is equal to the RMS MD difference. Since the major portion of all the data points exist below the black line, this indicates that, in optimizing the OD and MD in all the structures, it is easier for the algorithm to optimize the OD instead of the MD. This can be easily understood as grain orientations can always be independently assigned, whereas misorientations are highly dependent on the local arrangement of the orientations.

Another interesting feature of the semi-log plot in Fig. 8.5 is that below a RMS OD difference of approximately 0.05, there is always a linear portion in the plots. The linear relationship of $y = Ae^{mx}$ and the coefficient of determination values, R^2, have been solved and the detailed values are reported in Table 8.2. This linear relationship was obtained by only analyzing the data points from using weight values that were in the range of 0.3 to 10.0 or OD_weighting of 0.462 to 1.818 and MD_weighting of 0.0303 to 1.538. The R^2 values given in Table 8.2 not only report how accurately the linear relationship fits the data, but can also be used to interpret which structure, within the specified range, offers the most linear correlation between OD and the MD. From Table 8.2, the maximum R^2 value was obtained using the Plank structure. The data points produced by the Plank structure are also the points that lie closest to the lower left corner of the top graph shown in Fig. 8.5. This is an indication that it is easiest to match the target OD and MD using the Plank structure, as one might expect since each grain has only two nearest neighbors, which represents the least complicated neighborhood.

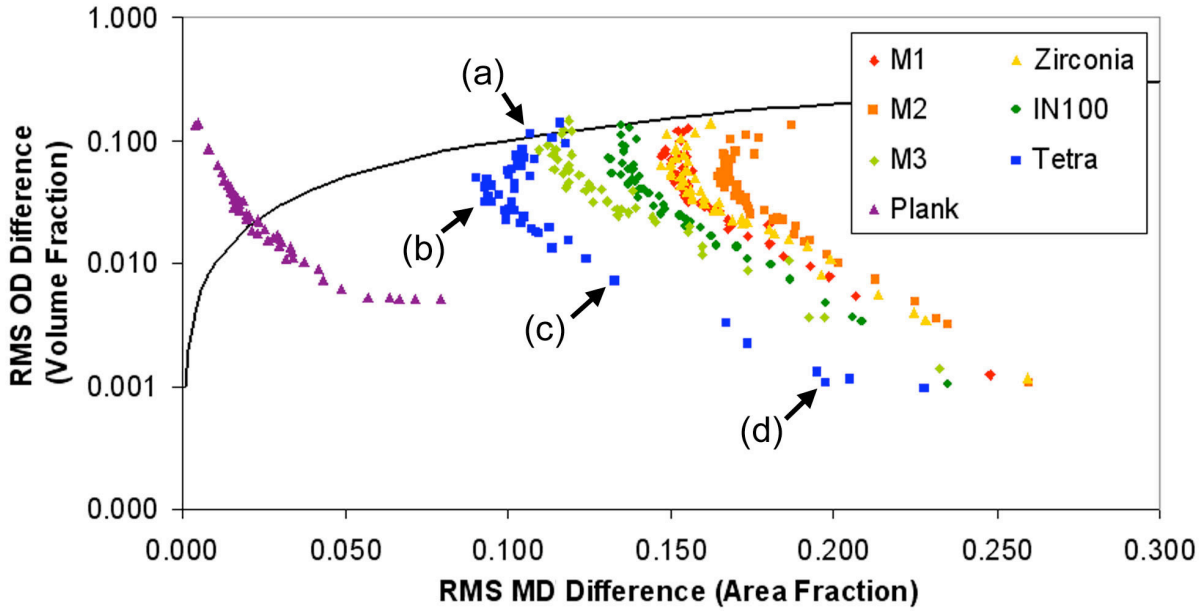

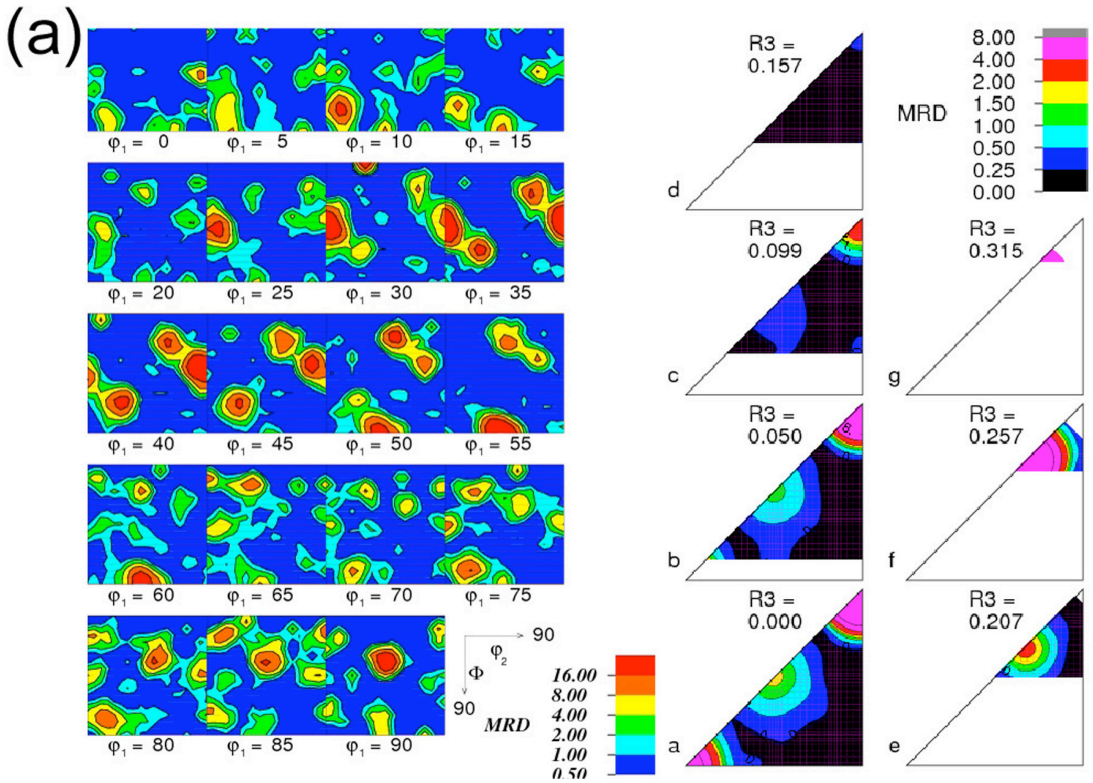

*image continues on following page

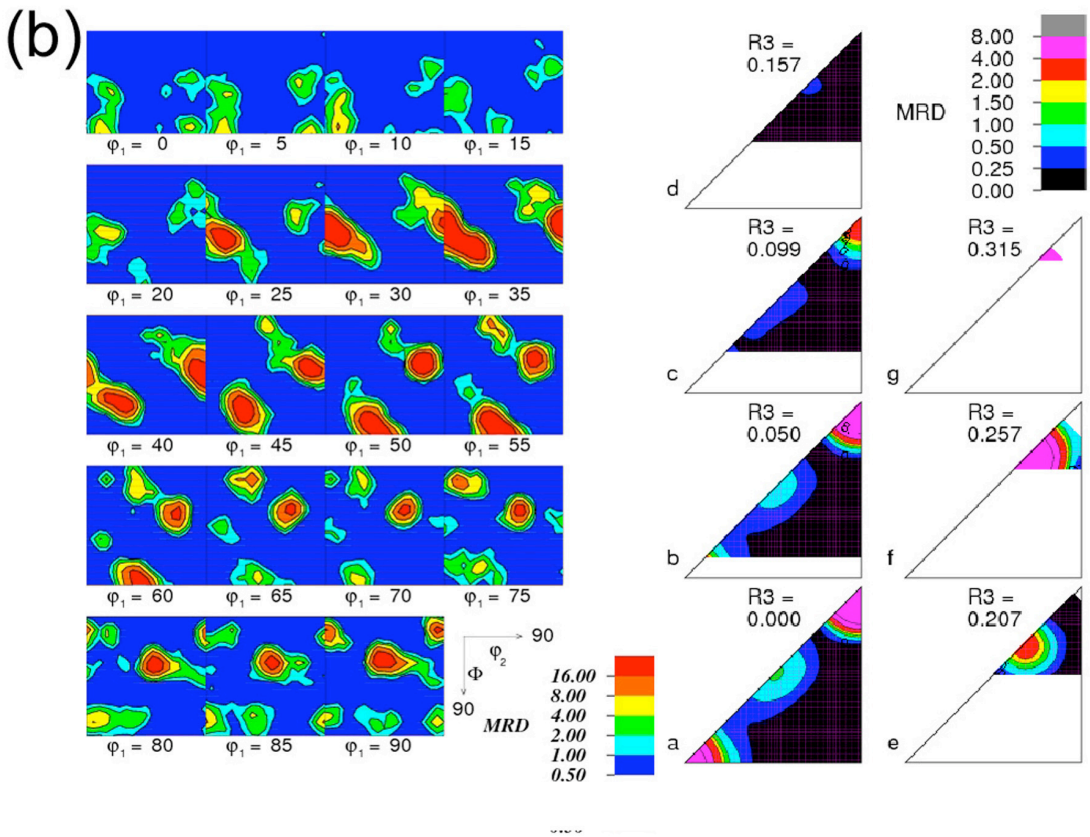

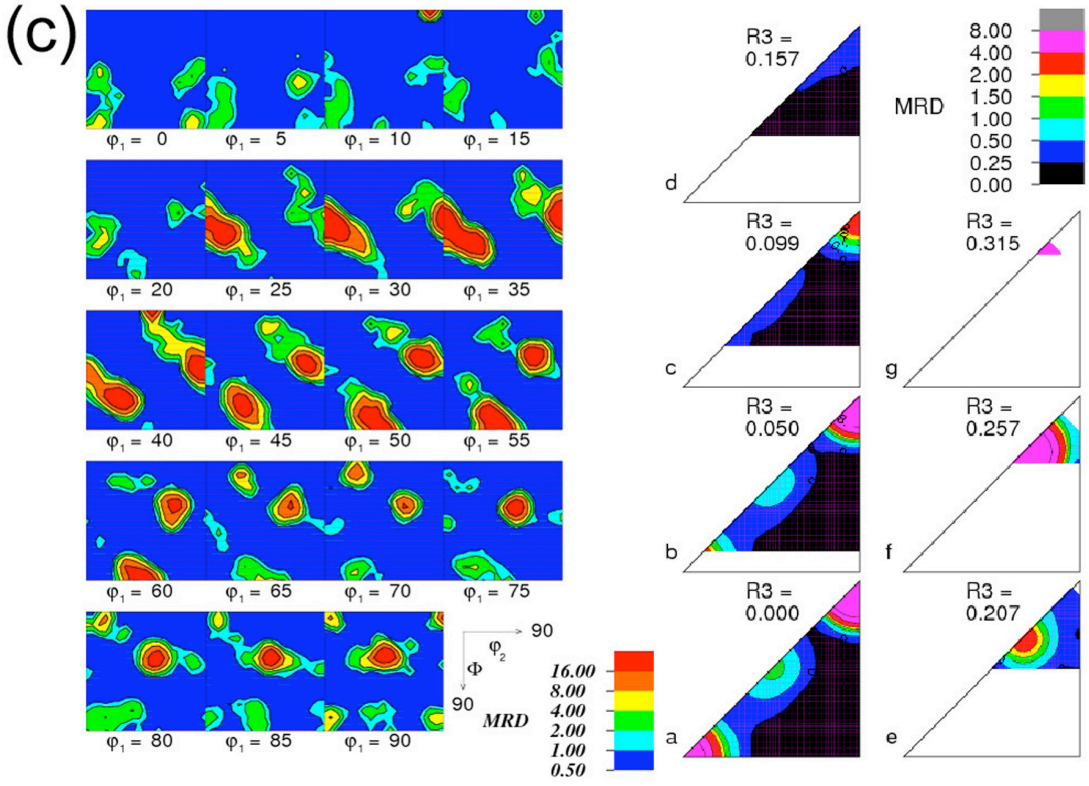

*image continues on following page

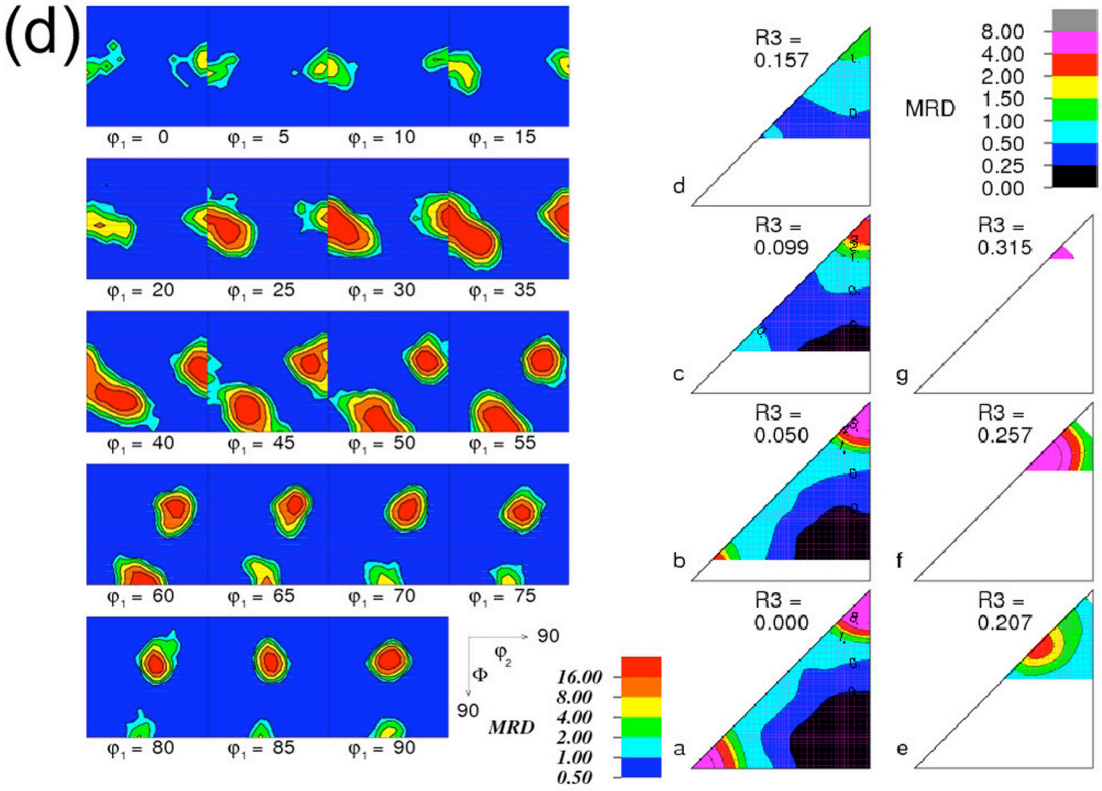

Figure 8.5 The plot of the root mean square difference between the target and output OD vs the root mean square difference between the target and output MD is shown at the top. The colored lines were plotted using constant total error values given in Table 8.1. The points of intersection between the constant total error curves and the data points indicate the most optimum fit between the OD and MD. The Euler angle plots and Rodrigues-Frank plots shown from a-d are the output distributions obtained from using weight values of 0, 0.5, 10, and 390 respectively with the tetrakaidecahedron structure.

Table 8.2 The variables fitting into the relationship of $y = Ae^{mx}$ for the linear portions of the top graph found in Fig. 8.5. The linear fit was obtained by using the results of the simulations that used weight values of 0.3-10, and both options of MD_weighting. The coefficients of determination (R^2) values for the fitting of the equations are also given for the different 3D microstructures.

Structure	A	M	R^2
M1	79.176	-48.246	0.869
M2	146.33	-47.692	0.842
M3	4.275	-36.444	0.885
Plank	0.0819	-56.251	0.942
Tetra	1.251	-38.432	0.926
Zirconia	29.888	-41.505	0.851
IN100	21.322	-43.920	0.905

The conclusion that can be drawn in this section is that there is an exponential relationship that exists between orientation and misorientation distributions. However, as can be seen in the plots, a weak texture allows the algorithm to match the maximum fraction of the

desired boundary types more easily. Also, there is always a compromise between obtaining the most desirable orientation distribution and misorientation distribution. As can be seen with the data points generated with the different structures, geometrical differences in the structure also play an important role in correlating the orientation and misorientation distributions.

8.4.2 Initiating simulations with random or non-random orientations

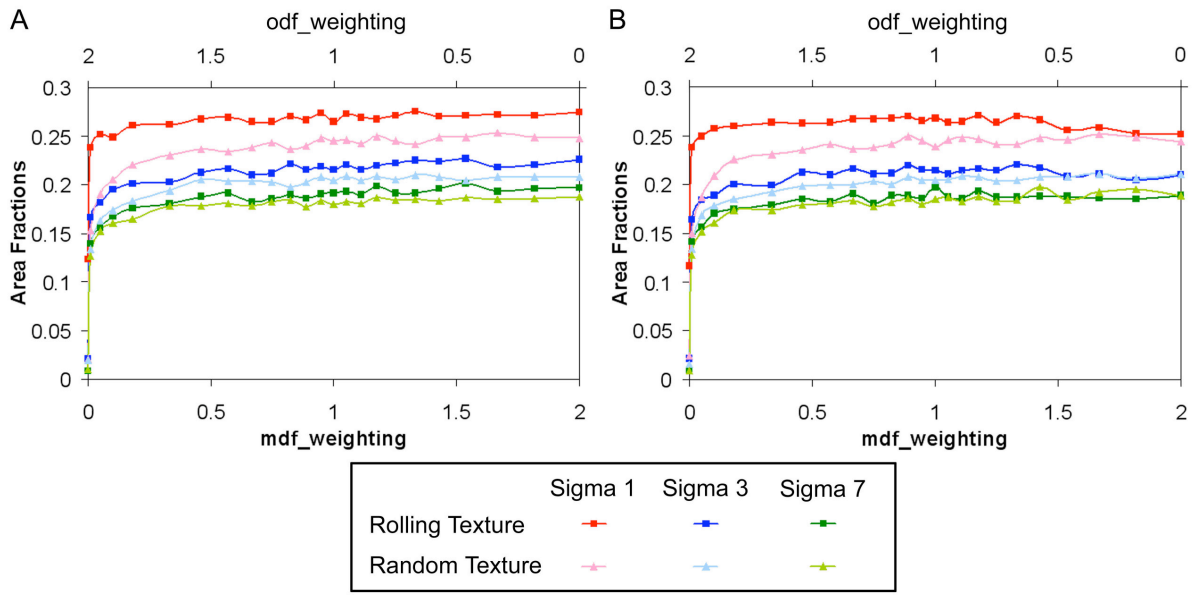

Figure 8.6 Area fractions of Σ1, 3, 7 boundaries plotted against MD_weighting and OD_weighting showing results obtained by (A) matching initial grain orientations to the input OD, and (B) having random initial grain orientations. The results obtained from rolling texture are shown in the bright colors while the results from random texture are shown in the lighter colors. For the number of annealing steps used, the initial orientation assignment does not influence the result.

Results from assigning grain orientations for the M1 structure with the target OD being either rolling or random texture, the target MD being the combination of Σ1, 3, and 7 types, and the two options of assigning initial grain orientations randomly or based on the target OD are shown in Fig. 8.6. Comparing the two plots shown in Fig. 8.6, it is evident that there is no difference between initializing the grain orientations with either of the two options. The reason is because regardless of the initial grain orientations, and assuming that enough iteration steps

were used in the simulated annealing based optimization method, the resulting texture always proceeds towards the target OD and MD.

8.4.3 Optimizations with changing or swapping of Orientations

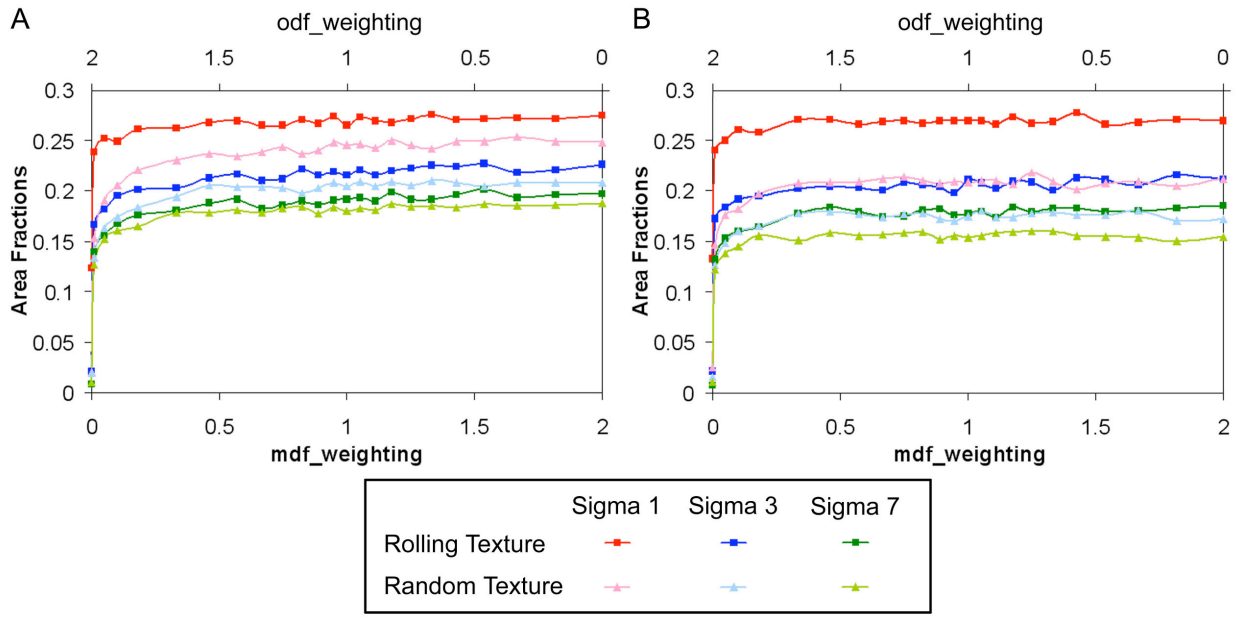

Figure 8.7 Area fractions of Σ1, 3, 7 boundaries plotted against MD_weighting and OD_weighting showing results obtained by (A) allowing the grain orientations to change and swap in the simulated annealing procedure, and (B) allowing only swapping of orientations. The results obtained from rolling texture are shown in the bright colors, while the results from random texture are shown in the lighter colors.

Figure 8.7 shows the results obtained from assigning grain orientations for the M1 structure with the target OD being either rolling or random texture, target MD being the Σ1, 3, and 7 list, and two different options of evolution mechanisms: changing and swapping grain orientations or only swapping orientations between grains. As seen in Fig. 8.7, when the evolution mechanism is limited to only the swapping of orientations, the area fractions of the desired CSL boundaries found in the structure are lower than if both changing and swapping of grain orientations were allowed. Once the grain orientations are initialized, the swapping evolution mechanism prevents the system from optimizing the misorientation distribution since the simulated annealing procedure becomes a simple reshuffling of the same list of grain

orientations. Therefore, even with an infinite number of iteration steps, the final misorientation distribution would be dictated only by the initial grain orientations.

8.4.4 Number of Iteration Steps

Figure 8.8 shows the total error plotted against the number of iteration steps obtained by assigning orientations for the M1 structure with the target OD being the rolling texture, and the target MD being the list of Σ1, 3, and 7 misorientations under equal weighting for the OD and MD. The graph shows that as the number of iteration steps increases, the error for the system, as calculated with Equation 6.1, decreases. This graph shows that at the end of the simulation run, the total error of the system is reduced to approximately 1% of the total initial error. Therefore, it appears that the choice of 50 annealing steps and a minimum of 10N, with N being the total number of grains, of successful evolutions per annealing step are acceptable values to use in optimizing the OD and MD.

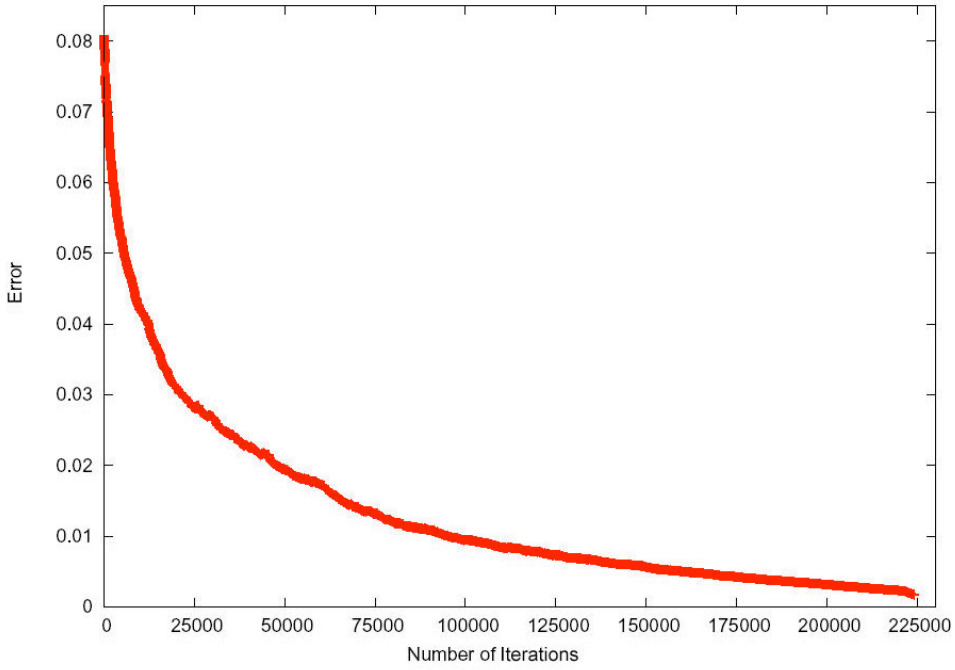

Figure 8.8 Plot of the total error of the system against the number of iterations as orientations were assigned to the M1 structure with the target OD being the rolling texture, target MD being the list of Σ1, 3, and 7 misorientations, and equal weighting for the OD and MD.

8.4.5 Annealing Temperature

Figure 8.9 shows orientation assignment performed on the M1 structure with the target OD being the rolling texture, the target MD being the list of Σ3 boundaries, and varying annealing temperatures. Once again, both Equations 8.4a and 8.4b were used to calculate MD_weighting as the weight value ranged from 0 to infinity. As seen in Equation 8.4, as the annealing temperature is increased, the probability of accepting an evolution step of either changing or swapping of grain orientations is also increased. Therefore, in the limit of increasing the annealing temperature to ~50, the simulation study accepts every proposed evolution step, and the output OD and MD become nearly random. The graph also indicate that temperatures lower than 0.0001 appear to be unlikely to result in a smaller error at the optimum point.

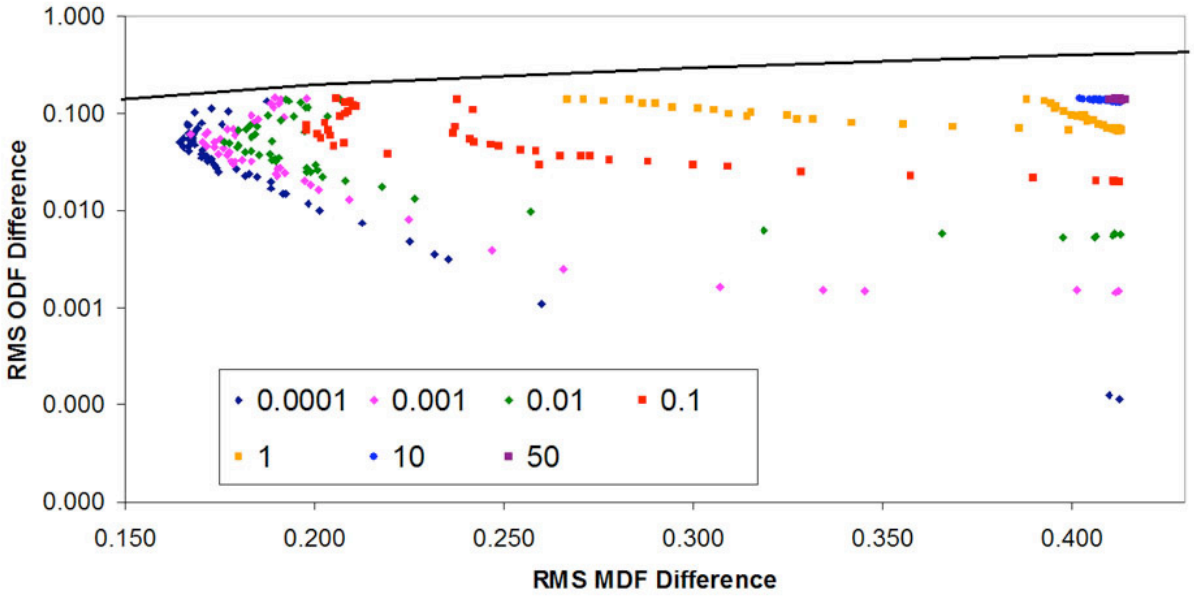

Figure 8.9 Plot of the summation of the root mean square difference of each bin in homochoric space between the output and target OD vs MD showing the effects of changing annealing temperature.

8.4.6 Summary

The effects of the variables used in the MD version of the grain orientation assignment algorithm have been investigated. Weighting values for OD_weighting in the range of 0.4 to 1.8, and MD_weighting in the range of 0.03 to 1.5 are all acceptable values to use when optimizing the orientation and misorientation distributions for a structure. In initiating the grain orientations with a random distribution or the target orientation distribution, either choice yields the same output distributions. Both evolution mechanisms of swapping orientations and randomly assigning new orientations are needed to achieve an optimum fitting of the OD and MD. Lastly, the default settings of 50 annealing steps with a maximum of 10N successful evolutions per annealing step, and an annealing temperature of 0.0001 are all reasonable values to use for the grain assignment algorithm.

8.5 Validation of the Algorithm – MD Version

One of the methods that can be used to validate the current method of assigning grain orientations through simulated annealing is by measuring and comparing the CSL boundary distributions with the results of Garbacz *et al.* and Gertsman *et al.* [108, 132, 133, 140]. To match the methods used by these researchers, the MD_weighting was set to 0 such that the OD would be matched exactly to the target distribution, and the orientations can be randomly assigned to the grains. For either the random or fiber texture simulations, only results from the Plank and tetrakaidecahedron structures are shown for clarity. Minor fluctuations were observed between the results from the other synthetic structures and the tetrakaidecahedron structure, which could have been caused by the geometrical differences between the structures. As a

reminder, the results from Pan *et al.* [141] and Morawiec *et al.* [142] were calculated with Equation 4.1 rather than measured with simulations, and are included in Fig. 8.10 for interest.

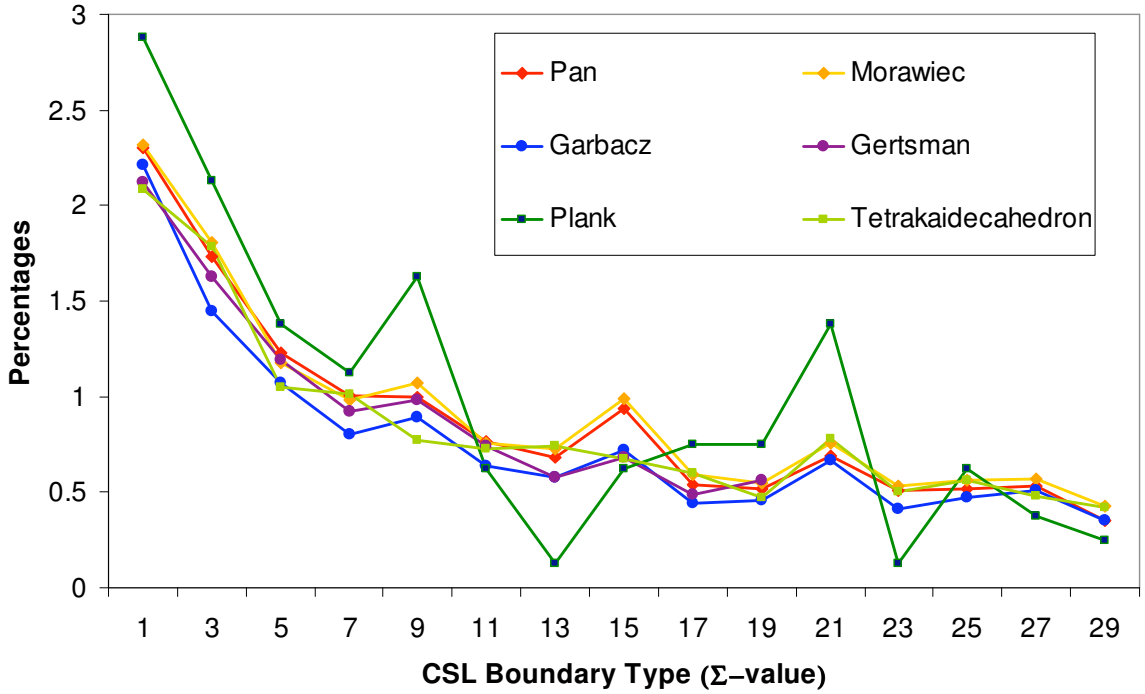

Figure 8.10 Plot of the percentage of sigma boundaries that are calculated by assigning random orientations to the Plank and tetrakaidecahedron structures, with results obtained from Gertsman *et al.* [108], Garbacz *et al.* [132], Pan *et al.* [141], and Morawiec *et al.* [142] for comparison.

The orientation assignment that used a random texture as the target OD is shown in Fig. 8.10. As seen in the figure, results from the tetrakaidecahedron structure closely resemble the results collected from the other researchers. The results from the Plank structure were kept in Fig. 8.10 to show the exception that was seen in this simulation, with significant errors for Σ9, Σ13, Σ21 and Σ23. The Plank structure is the unique structure where each grain only has a maximum of two grain neighbors with the same grain boundary area. Therefore, due to the limitation of having so few boundaries and no distribution of different grain boundary areas, only a very distinct set of orientations will allow a match to the reported results.

The results obtained from using the <111> fiber texture as the target OD are shown in Fig. 8.11. The percentages of CSL boundary types obtained from the current study fully match

Gertsman *et al.*'s [108] percentages. On the other hand, the percentages reported by Garbacz *et al.* [132] appear to overestimate the populations of the Σ1, 3, and 7 boundaries. Another observation to be made is that for the <111> fiber texture, the set of percentages of the CSL boundaries obtained from the Plank structure also matches Gertsman *et al.*'s distributions. This may be an indication that the <111> fiber texture poses a limit on the possible CSL boundary types, and even with many fewer grains in the Plank structure, the limitation is still evident.

Figure 8.12 shows the results generated by performing grain orientation assignments with the <100> and <110> fiber textures as the target orientation distributions. Once again, the percentages of the various CSL boundary types match very closely with the percentages reported by Gertsman *et al.* [108]. In fact, the percentages of the boundaries match up almost perfectly for the <100> fiber texture.

Since all the percentages of CSL boundary types generated with the current simulation method match the percentages reported by Gertsman *et al.*, the MDF version of the grain orientation assignment algorithm is verified to be an effective method in assigning grain orientations to digital microstructures.

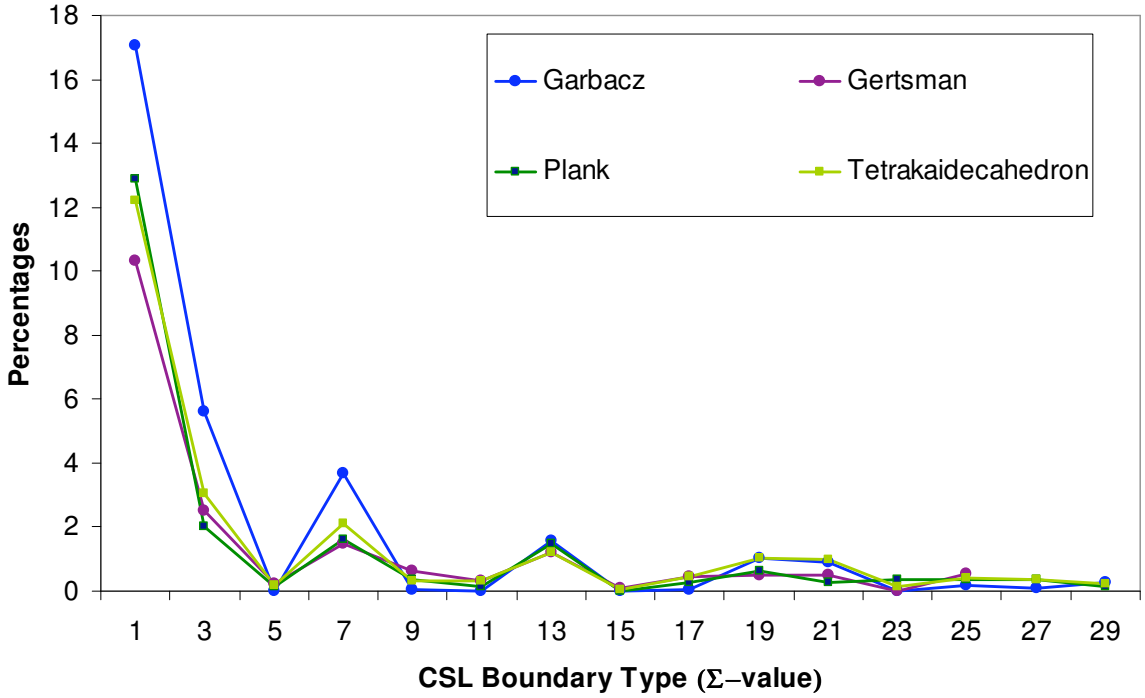

Figure 8.11 Plot of the percentage of sigma boundaries that is obtained by imposing the <111> fiber texture onto the Plank and tetrakaidecahedron structures, with results obtained from Gertsman *et al.* [108], and Garbacz *et al.* [132] for comparisons.

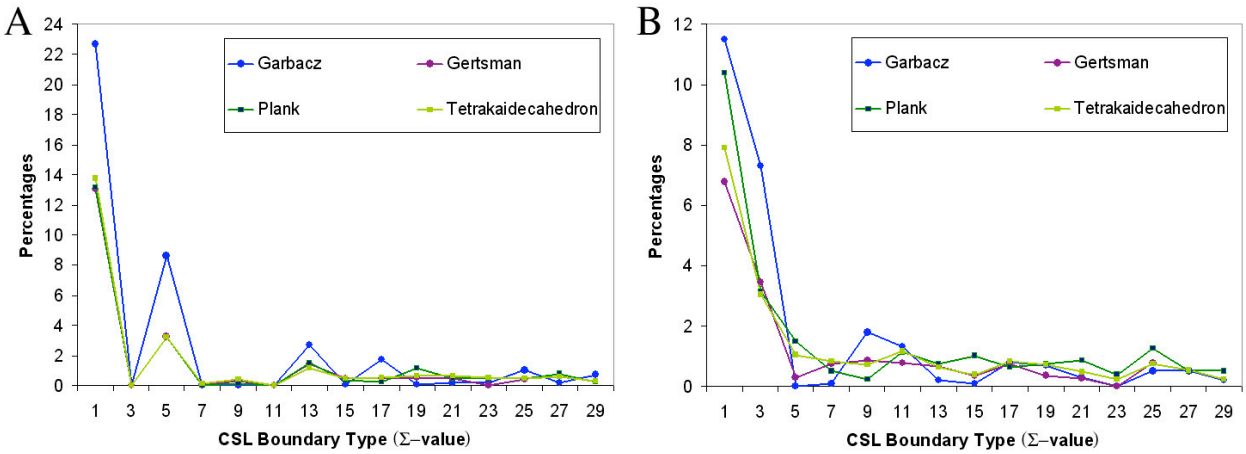

Figure 8.12 Plot of the percentage of sigma boundaries that is obtained by imposing the (A) <100> and (B) <110> fiber textures onto the Plank and tetrakaidecahedron structures, with results obtained from Gertsman *et al.* [108], and Garbacz *et al.* [133] for comparisons.

8.6 Application of the MD Version of the Grain Orientation Assignment Algorithm – Studying the Microstructure Geometrical Effects on OD and MD

The effects of the different microstructural parameters on the relationship between OD and MD can be explored with the grain orientation assignment algorithm. The geometrical features of the structure, such as the number of grains in the system, the grain size distribution, and the grain shape, can be varied as the target OD and MD remains constant while the algorithm is used to perform grain orientation assignments. To isolate the different microstructural parameters, different versions of the Plank and tetrakaidecahedron structures were used in the studies performed for this section. This includes changing the thickness of each square slice for the Plank structure to create a grain size distribution, and repeating each x-z slice in the tetrakaidecahedron structure to simulate the effects of elongating the grains, without changing the number of neighbors shared by each grain.

8.6.1 Number of Grains

Figure 8.13 shows the effects of changing the number of grains used in the simulation of fitting a target MD of Σ3 relationships, and target OD of rolling texture to the tetrakaidecahedron structure. Different versions of tetrakaidecahedron structures with varying number of grains in the same bounding cube size were created for this analysis. Periodic boundary conditions were also used to explore whether having surface grains would affect the relationship between OD and MD. The results show that as the number of grains increases, the OD and MD approach closer to the target distributions. However, periodic boundary conditions only have minor effects on the RMS OD and MD differences. When the use of periodic boundary conditions removes the effects of surface grains, the simulation does not optimize the OD and MD distributions as effectively, as seen by the shifting of the curves to the right. Surface grains should allow an

easier fit of the orientation and misorientation distributions to the structure since the surface grains add a degree of freedom. Thus, the surface grains have less effect on the misorientation distribution when the orientations of those grains change. Also noteworthy is that, when the surface grains are removed, the grain size distribution becomes uniform. Therefore, it is unclear as to how the surface grains truly affect the relationship between the OD and MD. However, it remains clear that when enough grains are included in the simulation, periodic boundary conditions do not need to be imposed to obtain an optimum match between the output and target distributions.

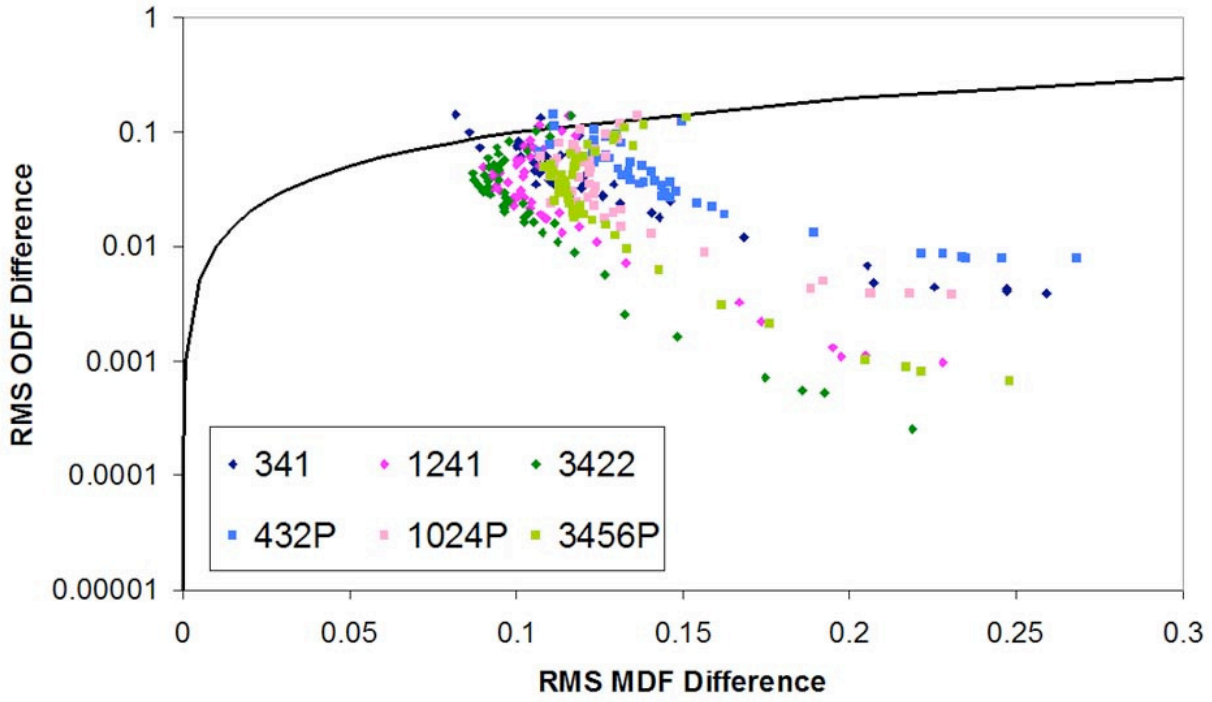

Figure 8.13 Plot of the summation of the root mean square difference of each bin in homochoric space between the output and target OD vs MD showing the effects of changing the number of grain included in the system. The P in the index denotes that periodic boundary condition was imposed on the structure.

8.6.2 Grain Size Distribution

Different variations of the Plank structure was used to study the effects of grain size distribution on the OD and MD relationship. In order to impose a grain size distribution onto the

structure without having to change any of the other microstructural variables, the Plank structure was the best choice for this analysis. The difference between the various versions of Plank structures is that the square slices in the structure are allowed to have different thicknesses to match the different grain size distributions shown in Fig. 8.14. In Fig. 8.14, the grain size distributions that are labeled as A and B were extracted from the previously mentioned experimentally reconstructed structures from the dual-beam FIB-SEM, the Zirconia and Inconel 100 structures respectively. The grain size distribution labeled C was arbitrarily created to match a normal distribution. Lastly, distribution D was extracted from the default Plank structure, where all the grains are of uniform size.

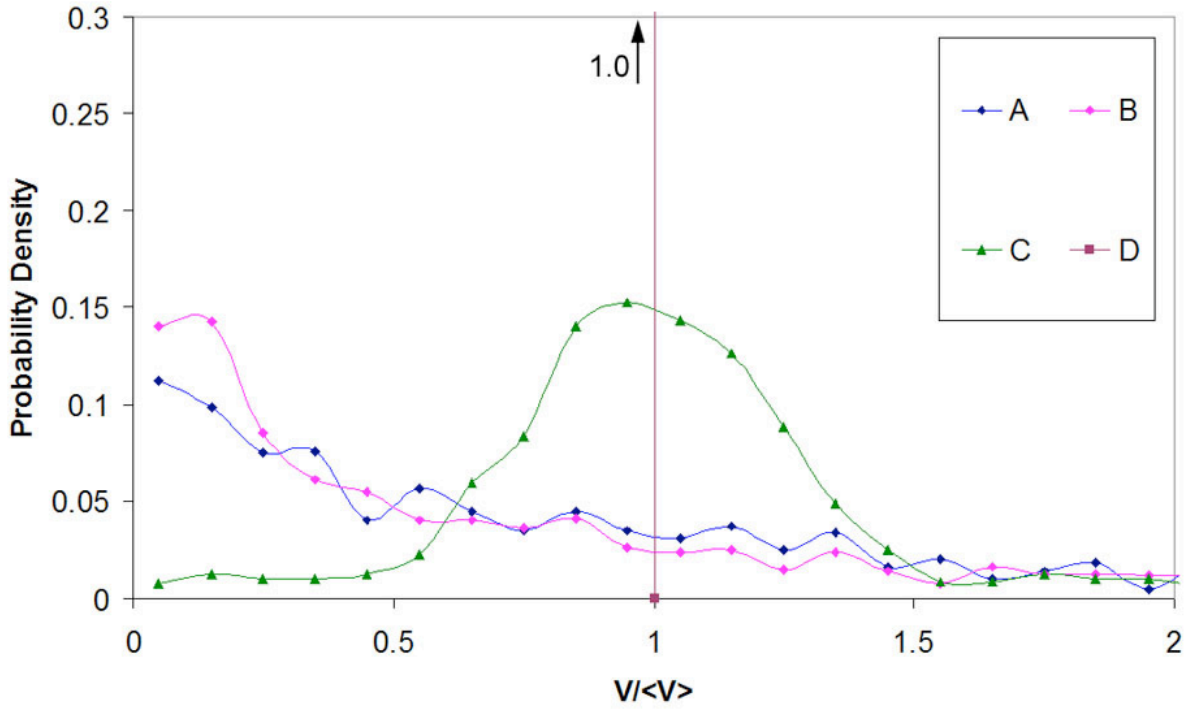

Figure 8.14 Probability density is plotted against normalized grain volume (volume/average volume). The grain size distributions A and B were obtained from the Zirconia and Inconel 100 structures respectively, while distribution C was created to resemble a normal distribution, and distribution D was obtained from the original Plank structure.

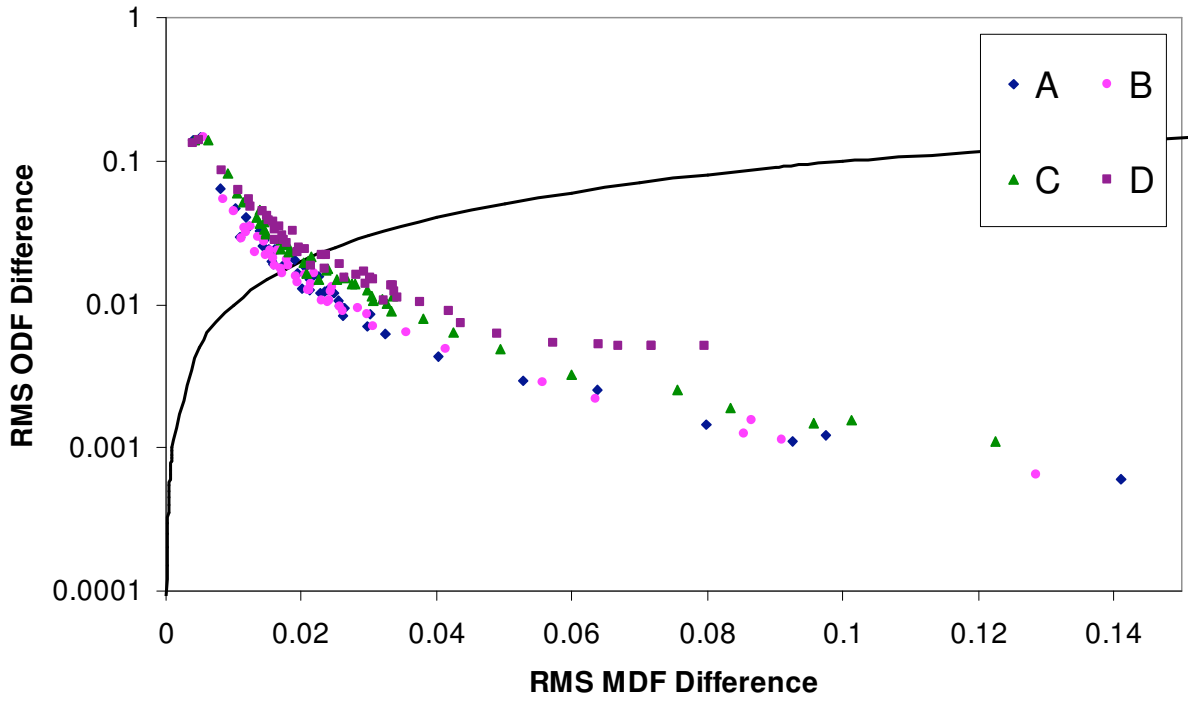

Figure 8.15 Plot of the summation of the root mean square difference of each bin in homochoric space between the output and target OD vs MD. The results were created by performing the simulation on different versions of the Plank structure that contains the various grain size distributions shown in Fig. 8.14. Little sensitivity to the grain size distribution is evident.

The simulation results shown in Fig. 8.15 indicate that the OD and MD relationship has only a weak dependence on the grain size distribution. The OD can be optimized slightly more easily with a wider grain size distribution, as seen with the shifting of the data points down towards a lower RMS OD difference. Distribution D is the limit to this study since it probably should not even be considered a distribution when all the grains in the population have exactly the same size. The rationalization of this observation is that volume and area weighted orientation and misorientation distributions are used to calculate the error in the system. When different volumes exist in the system, orientations that increase the error of the system do not necessarily need to be removed. Instead, the program can rely on the swapping evolution mechanism to reassign these orientations to grains that have a much smaller volume. For the case when all the grains are the same size however, the simulation is forced to remove the

erroneous orientations and find the exact orientation that results in a lower system error. No effect can be seen on the fitting of the misorientation distribution. This is due to the fact that the number of neighbors per grain was set to be constant. Even though different grain sizes were imposed onto the structures, the grain boundary areas remained constant in the four different structures.

8.6.3 Grain Shape

In order to adjust the grain shapes without affecting the other microstructural parameters, different variations of the tetrakaidecahedron structure were used in this study. As seen in Fig. 8.16, the difference between the variations of tetrakaidecahedron structures simply involves the number of times each x-z slice in the structure was duplicated. This act of duplicating each layer in the voxel structure allows a rolled structure to be created while maintaining the number of grain in the system and the number of neighbors shared by each grain constant.

The results shown in Fig. 8.17 were obtained by performing the simulation on the structures shown in Fig. 8.16, using the rolling texture as the target OD, and the list of Σ3 relationships as the target MD. As seen in Fig. 8.17, the change in grain shape has no effect on the relationship between rolling texture and sigma 3 misorientations. However, the result may be different if a fiber texture is imposed along the different directions for the various structures.

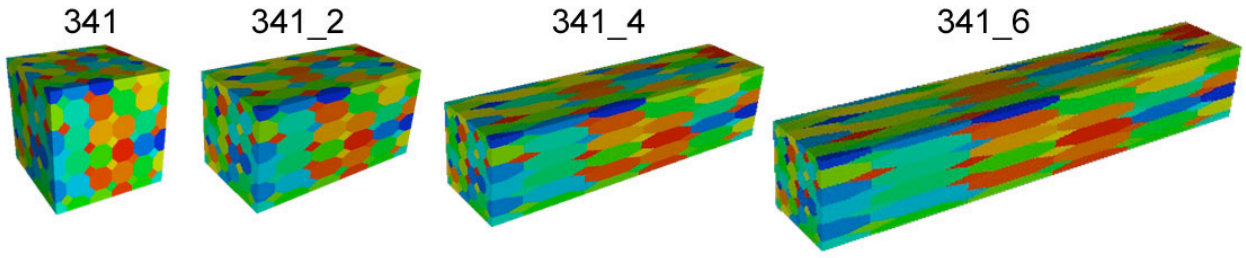

Figure 8.16 The four different variations of tetrakaidecahedron structure with each number following the underscore denoting how many times the x-z slice has been duplicated.

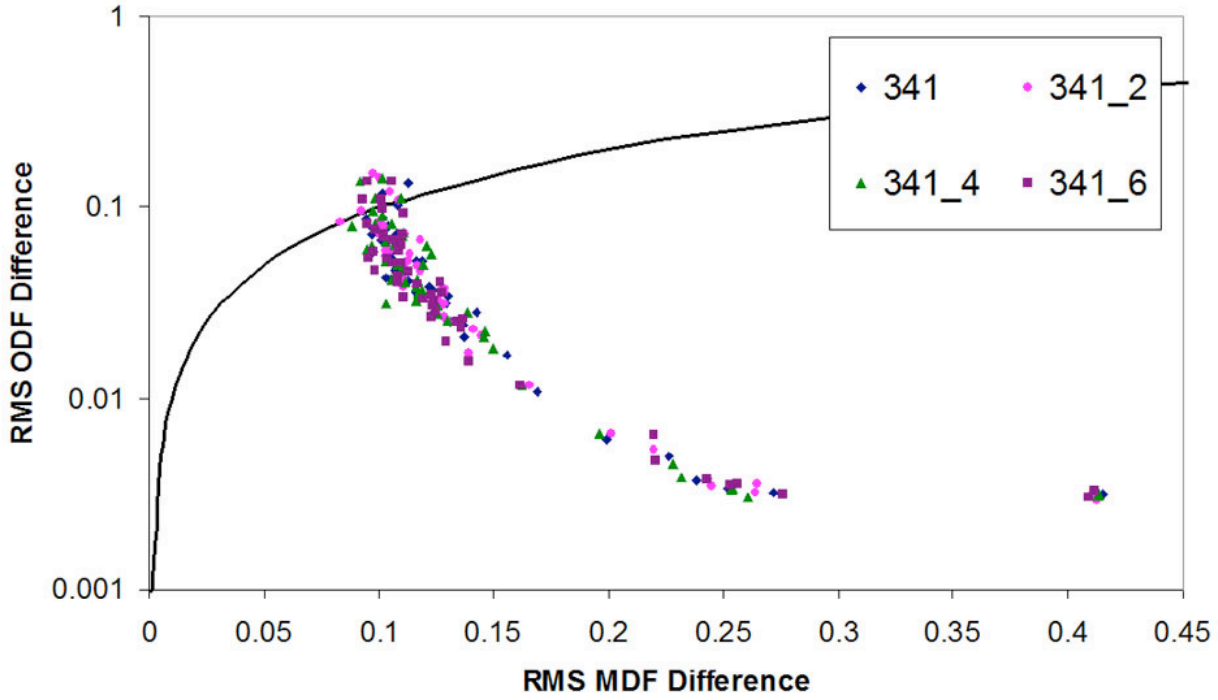

Figure 8.17 Plot of the root mean square difference between the output and target OD vs MD showing the effects of changing the grain shape. The results were obtained by performing simulations on the structures shown in the previous figure. No sensitivity to grain shape is evident.

8.6.4 Summary

The geometric effects on the grain orientation assignments and resulting misorientation distributions have been analyzed. The results show that structures with a larger number of grains have minor effects on the orientation and misorientation distributions. However, as seen in Section 8.6.1, when periodic boundary conditions are imposed on the system, a large number of grains is necessary for improving the OD and MD fitting. The grain shape and the grain size distribution did not appear to have any effects on the ability of the structures to obtain any specified misorientation distributions with the fixed orientation distribution. This observation may be a consequence of the constraint of the number of neighbors shared per grain.

8.7 Application of the MD Version of the Grain Orientation Assignment Algorithm – Studying the Effects of Orientation Distribution on Misorientation Distribution

The effects of the orientation distribution on the misorientation distribution can be explored with the grain orientation assignment algorithm by matching different target ODs with different target MDs. For this purpose, the results in Fig. 8.18 were obtained by performing grain orientation assignment on the M2 structure with the target OD being the rolling texture or random texture, and the target MD being the MD obtained from the rolled commercial-purity copper, the list of Σ1, 3, and 7 relationships, or the list of Σ3 boundaries. It is evident in Fig. 8.18 that the MD constructed with combinations of Σ1, 3, and 7 boundaries is much easier to attain than the unrealistic target that requires the entire grain boundary network to be constructed of only Σ3 boundaries. This is indicated by the data points, obtained from using Σ3 boundaries as the target MD, being located on the right side of the plot. However, the plot also shows that when both the OD and MD were experimentally extracted from the rolled commercial-purity copper, there is almost no difference between the output and target distributions. The RMS differences are not exactly zero due to the error in binning the orientations and misorientations into homochoric space.

When comparing the differences between fitting the random and rolling texture to the structure, the minimum RMS ODF difference observed for fitting random texture is 0.01, while for fitting rolling texture is 0.0001. The higher RMS difference in ODF fitting is due to the fact that the algorithm mathematically compares the target and output OD. The output ODs obtained from assigning grain orientations to the M2 structure with the three different MD and OD_weighting of 0 are shown in Fig. 8.19. Figure 8.19 illustrates that when the target OD was not taken into consideration, the most optimum fit between the target and output MD required

slight orientation preferences as seen in the pole figures. Even though qualitatively, the pole figures all show a random texture, mathematically however, any small preferences away from exact randomness would be penalized by the grain orientation assignment algorithm.

When comparing the data points obtained between using the rolling and random texture in conjunction with either the target MD constructed with the list of Σ1, 3, and 7 boundaries, or the list of Σ3 boundaries, the random texture always yielded higher RMS MDF differences. The higher RMS MDF differences can be attributed to the association of the texture with the fraction of CSL boundaries. As seen in Fig. 8.20, assigning grain orientations based on the rolling texture yields higher fractions of Σ1 and Σ3 boundaries than based on the random texture.

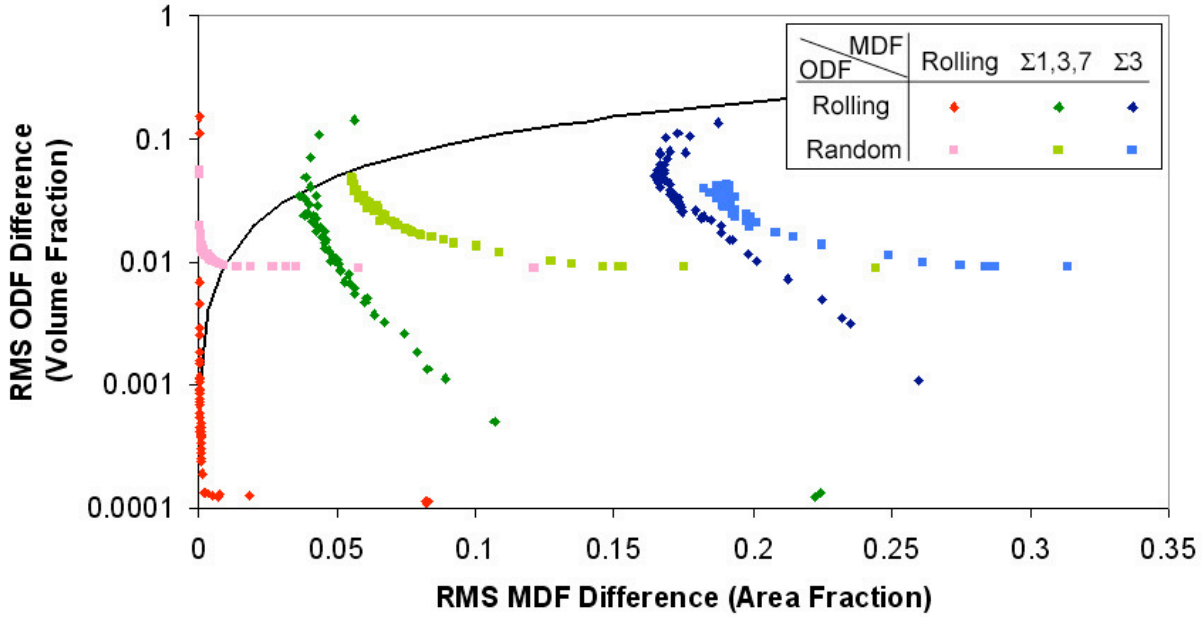

Figure 8.18 The plot of the root mean square difference between the target and output OD vs MD. The results were obtained by performing simulations on the M2 structure using rolling texture and random texture as the target OD and the rolling MD, the list of Σ1, 3, and 7 boundaries, and the list of Σ3 orientations as the target MD. In all cases the rolling texture target resulted in better fits to the target MD.

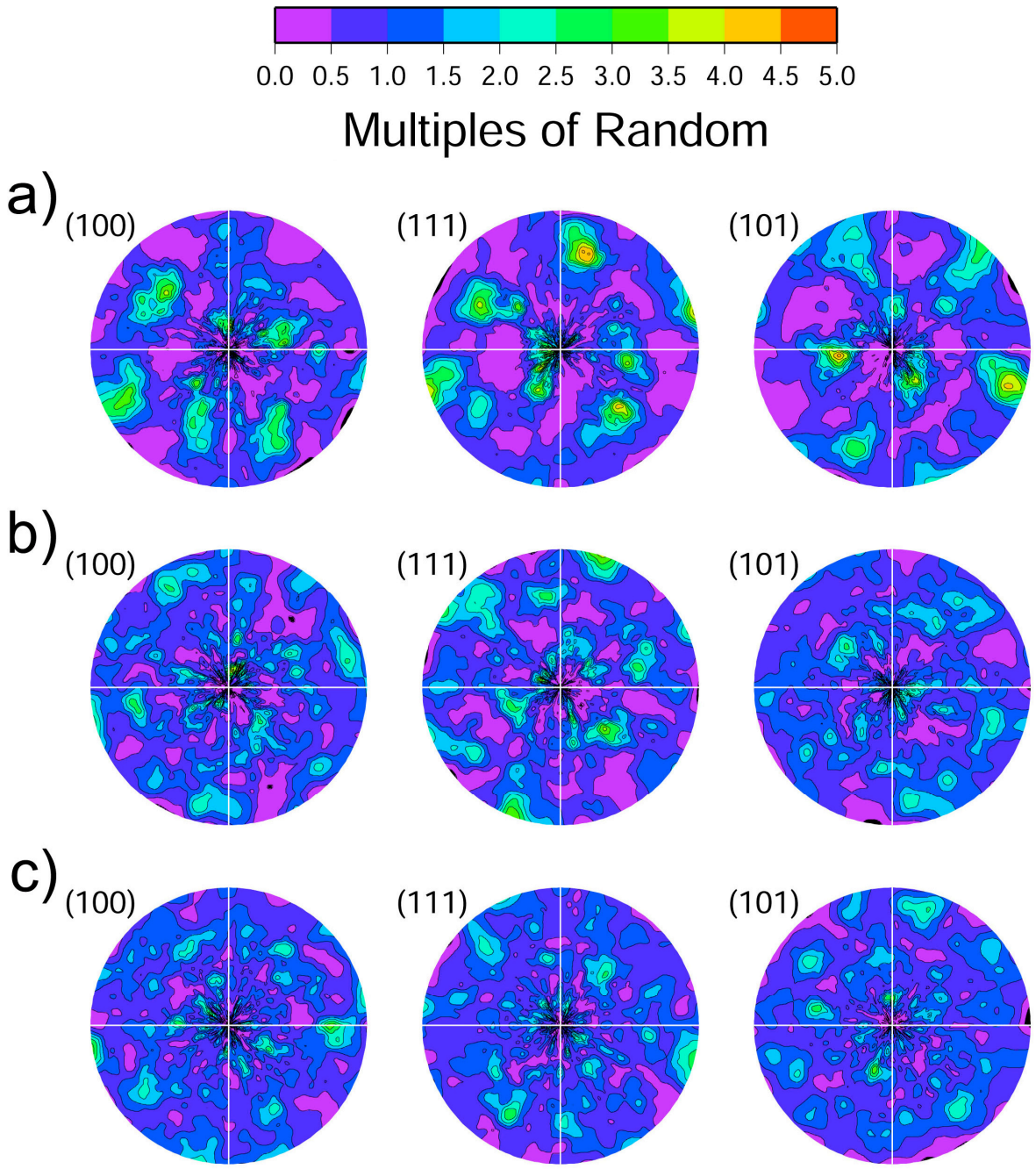

Figure 8.19 Pole figures obtained from assigning grain orientations to the M2 structure with OD_weighting of 0 and target MD of (a) Rolling MD, (b) Σ1, 3, 7, and (c) Σ3.

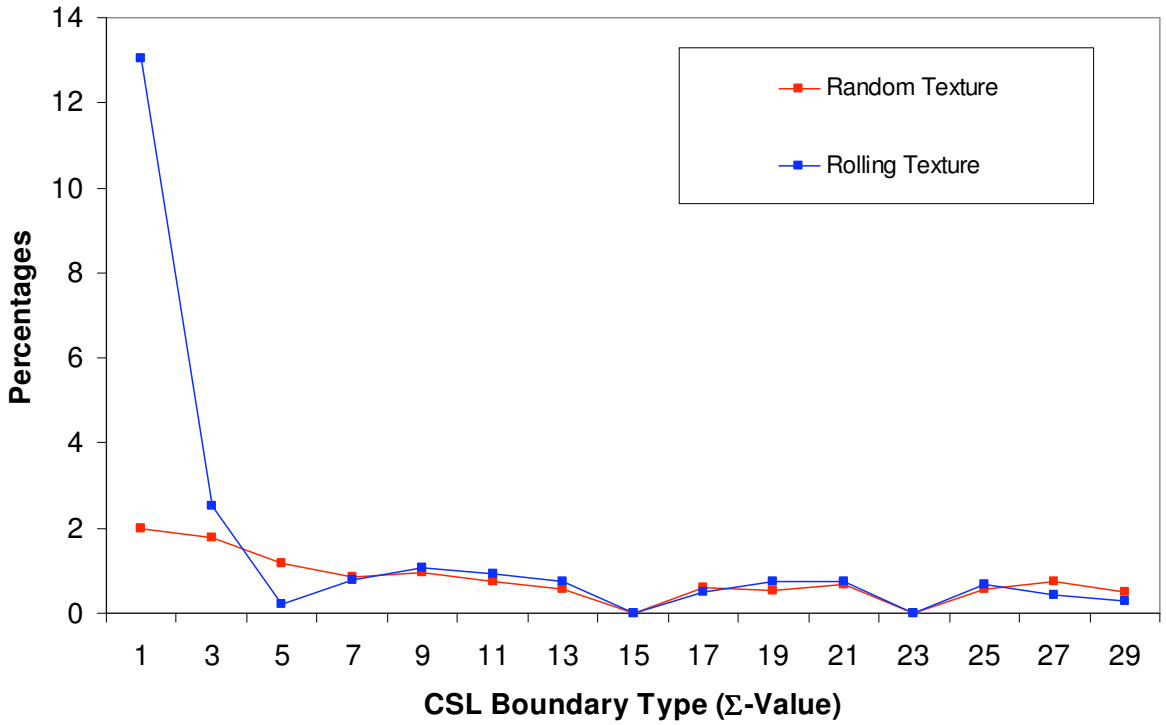

Figure 8.20 The percentage of sigma boundaries that are calculated by assigning random and rolling textures without target MD to the M2 structure.

8.8 Application of the GBCD Version of the Grain Orientation Assignment Algorithm – Studying the Effects of Grain Shape on Grain Boundary Character Distribution

To investigate the effects grain shapes have on the grain boundary character distribution, grain orientations were assigned to the M1 structure, which contains 1512 grains, a tetrakaidecahedron structure that contains 1594 grains, and a plank structure that contains 1594 grains of uniform grain size. The rolling texture was set as the target OD, while a GBCD obtained from a commercially pure nickel sample [139] was set as the target GBCD. The grain assignment algorithm was terminated simultaneously after 6 days of assigning orientations to the three structures. The error values obtained from the grain assignment algorithm with respect to the number of iterations is shown in Fig. 8.21. It is evident from Fig. 8.21 that within the same amount of "real", or wall-clock time, more iterations were made in fitting the grain orientations

to the M1 structure than to the plank or tetrakaidecahedron structures. The larger number of iterations per "real" time may be attributed to the number of successful changes to the grain orientations. In the M1, plank, and tetrakaidecahedron structures, the fractions of iterations that were successful in changing the grain orientations are 0.06, 0.16, and 0.26 respectively. After each successful iteration step, the GBCD must be calculated to reflect the change in grain orientation. Therefore, the more successful iterations there are, the longer the "real" time required to calculate the changed GBCD. Also, since the M1 structure contains variable grain boundary areas, a reduction in the GBCD calculation time may be observed when the affected boundary areas are relatively small. The iterations per "real" time observation may be different if an exception was made to the grain assignment algorithm when assigning grain orientations to the plank structure. Since the plank structure contains flat interfaces of the same area between all the grains, the calculation time of the GBCD can be greatly improved if all the triangular elements of the surface mesh were grouped into one boundary normal representation.

The output OD is represented by the Euler angle plots shown in Fig. 8.22. As seen in Fig. 8.22, the output OD from the M1 structure matches the closest to the target OD. The scatter observed in the output OD from the plank structure is due to the uniform grain sizes of the grains, which did not allow much freedom for the algorithm to have incorrectly matching grain orientations. The output GBCD plots are shown in Fig. 8.23. As seen in Fig. 8.23, the tetrakaidecahedron structure achieved the highest MRD of coherent Σ3 boundaries while only the M1 structure was able to match the Σ3, 9 and 27a boundary plane distributions observed in the target GBCD.

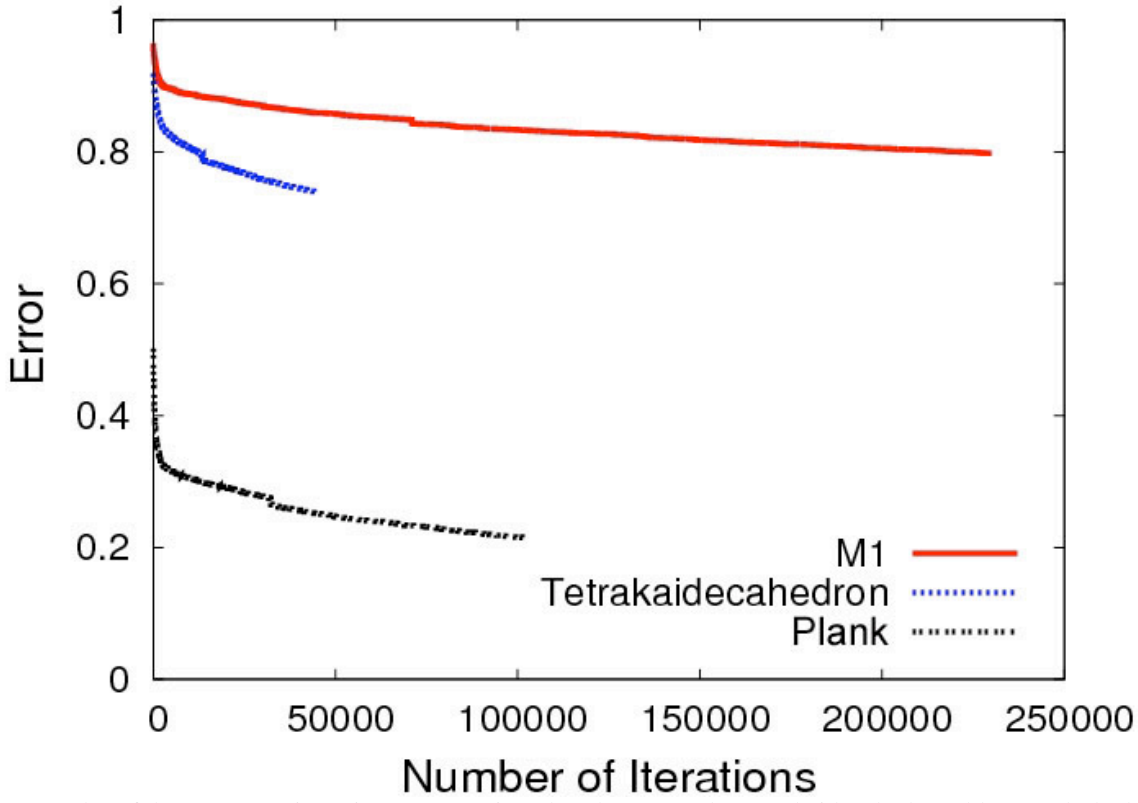

Figure 8.21 Plot of the error as orientations were assigned to the M1 (red), Tetrakaidecahedron (blue), and Plank (black) structures with the target OD being the rolling texture, and target GBCD obtained from a nickel sample that contains annealing twins. Simulation time was set to be the same for all three structures. The number of iterations performed on the M1 structure is 230,074, on the tetrakaidecahedron structure is 44,278, and on the plank structure is 102,440.

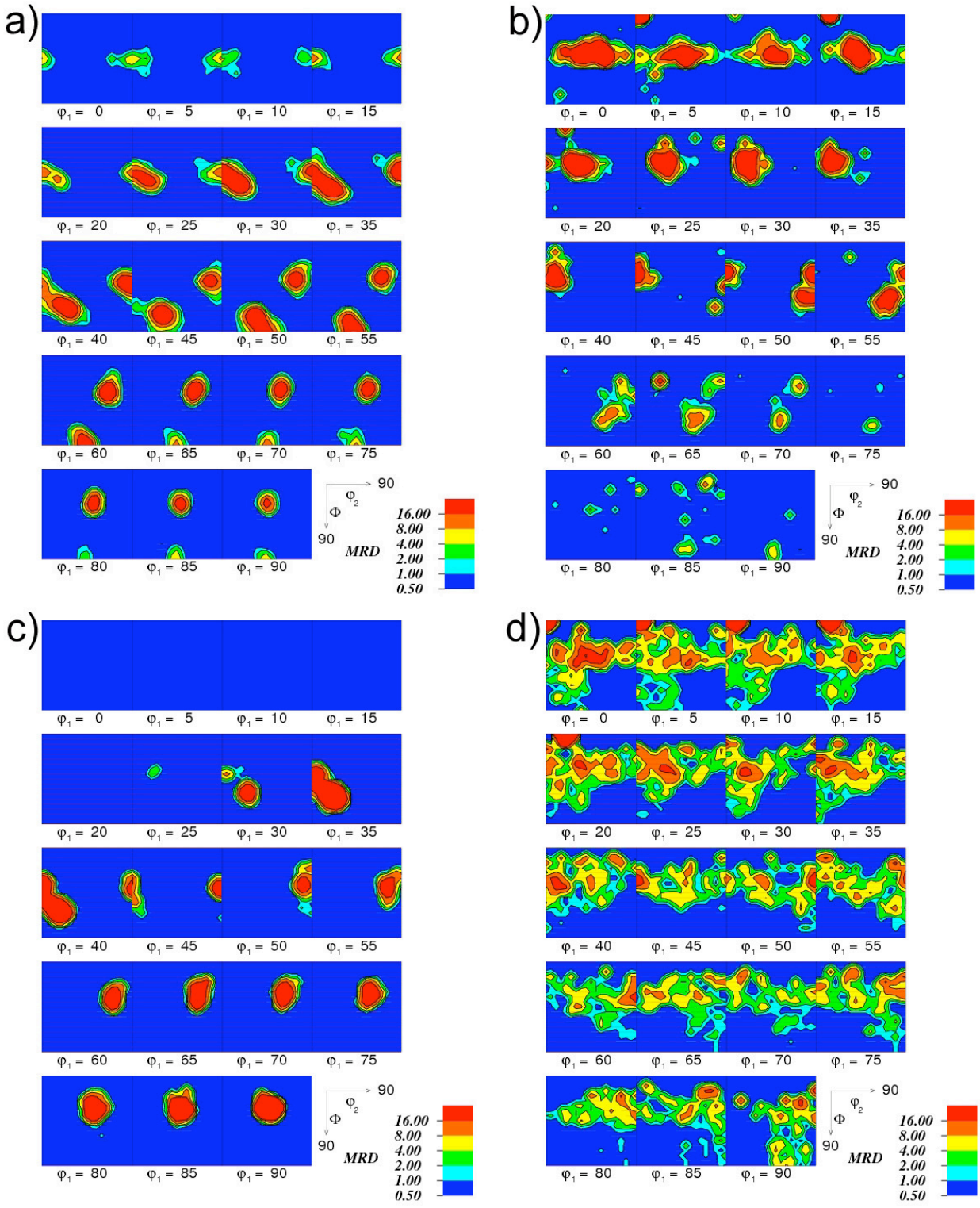

Figure 8.22 Euler angle plots showing the (a) target OD, rolling texture obtained from a rolled commercially pure copper, and assigned OD obtained after performing orientation assignment with the GBCD version of the algorithm on the (b) M1 structure, (c) Tetrakaidecahedron structure, and (d) Plank structure.

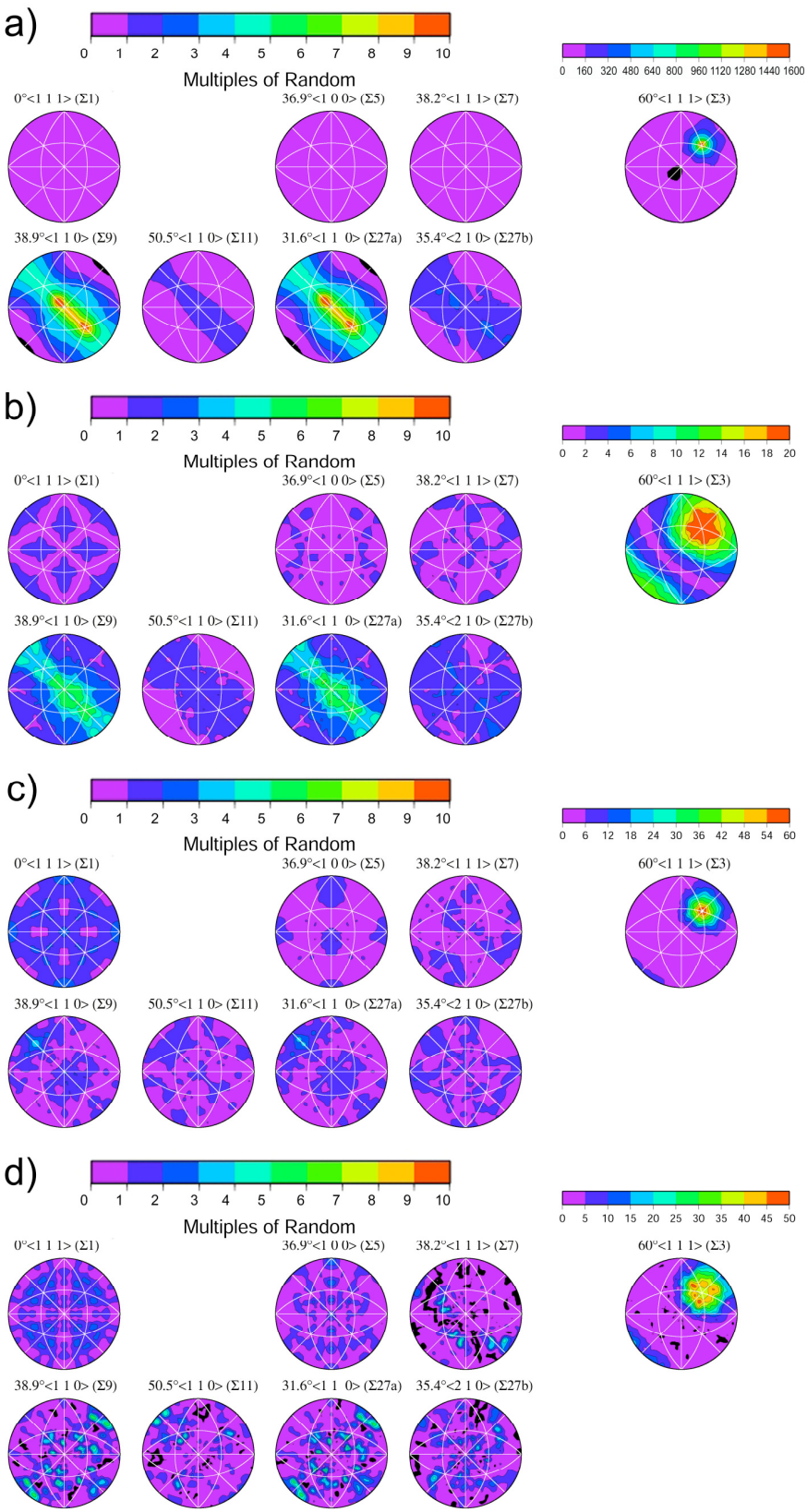

Figure 8.23 (a) Target GBCD plots measured from a commercially pure nickel sample, and output GBCD plots after performing the GBCD version of the grain assignment algorithm on the (b) M1, (c) Tetrakaidecahedron, and (d) Plank structures.

Chapter 9 Synthesizing Annealing Twins

9.1 Twin Insertion Algorithm

In many of the FCC materials that are studied, annealing twins are an important feature of the structure, and as mentioned in Section 2.2.3, twinning events are one of the most important aspects of grain boundary engineering. After the microstructure geometry has been defined by one of the microstructure generation methods described in Section 5.1, the twin insertion algorithm presented here will take the voxel structure and add additional grains to simulate the annealing twins. The twin insertion algorithm assumes that twin grains always completely section the parent grain, and the parent grain will reside on either side of the inserted twin or that the twin does not reside on the edge of the parent grain. The method of creating twins in the digital microstructures will help produce digital structures that are more representative of the experimentally observed microstructures that contain annealing twins.

Prior to inserting annealing twins into the specified microstructure, the Σ3 cluster distribution must be characterized in order to facilitate the twin insertion algorithm. Once the Σ3 cluster distribution is characterized (referred to as the preexisting Σ3 cluster distribution), the algorithm will synthesize annealing twins in the structure such that the final Σ3 cluster distribution will match the target distribution. To specify the target Σ3 distribution, Σ3 cluster sizes are listed in decreasing size. At each iteration step, the algorithm will only attempt to match one specified Σ3 cluster size by inserting annealing twins into the grains and rotating the grain orientations to create incoherent Σ3 grain boundaries. Therefore, the number of iterations is equivalent to the desired number of target Σ3 clusters.

After the target Σ3 cluster size is specified, the algorithm initiates the Σ3 clusters by utilizing the preexisting Σ3 clusters. If the target cluster size is smaller than the preexisting Σ3 cluster, the grains in the preexisting Σ3 cluster are used as the seed grains for synthesizing twins and initiating the Σ3 cluster growth. If no preexisting clusters satisfy the size criteria, a grain is chosen at random to initiate the Σ3 cluster.

Once the grain has been specified, twin insertion begins by identifying all the voxel positions that belong to the chosen grain, and calculating the center of mass and spherical equivalent radius of the grain. If the radius of the grain is smaller than 5 voxels, the algorithm does not attempt to insert twins into the grain. One of the eight variants of the <111> is chosen at random and the corresponding grain orientation for the twin is calculated by rotating the orientation of the parent grain 60° about the same <111> variant that was chosen. A fixed number of attempts is made (arbitrarily set to 40) to insert up to 6 twins into the chosen grain by identifying the orientation of the grain and calculating the <111> (the variant that was chosen) boundary plane for the grain in the sample reference frame. The calculation of the <111> boundary plane to insert into the grain is based on the basic definition of a plane in geometry, where a plane is a set of points that fulfill,

$$a(x - x_o^{'}) + b(y - y_o^{'}) + c(z - z_o^{'}) < \text{tolerance} \quad (9.1)$$

$$(x_o, y_o, z_o) = \text{centroid of the grain} \quad (9.2)$$

$$(x_o^{'}, y_o^{'}, z_o^{'}) = (x_o, y_o, z_o) + (D \infty \mathbf{n}) \quad (9.3)$$

where D is the distance between the plane and the centroid of the grain, and the other definitions of the variables are based on Fig. 9.1 [143] . The tolerance in Equation 9.1 determines the thickness of the grain, and is typically set as the minimum tolerance required by the grain with an additional random value that ranges from 0.8-1.3. The distance from the centroid of the grain

(D) in Equation 9.3 is also chosen at random to have a value that is in the range of 0 to 5 voxels away from the spherical equivalent radius of the grain. The choice of limiting the maximum value for D to be 5 voxels smaller than the grain radius is to avoid inserting twins on the edges of the chosen grain. The D value is tracked as each twin is inserted into the grain such that any subsequently added twins are not allowed to appear within approximately 3 voxels from any previously inserted twins. This ensures that as more twins are added into the grain, the twins will not intersect or overlap with one another. The intersection of the twins is avoided to allow easier tracking of the Σ3 clusters.

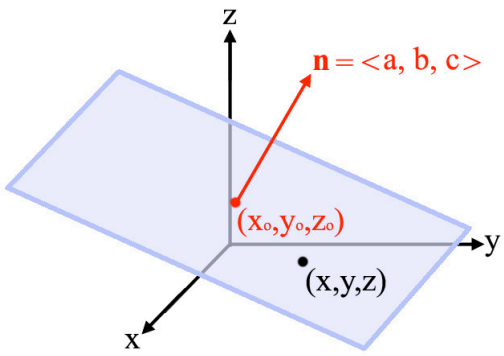

Figure 9.1 Schematic showing the calculation of the equation of a plane.

Once twin insertion completes on the specified grain(s), all the neighbors of every grain included in the current Σ3 cluster, with priority given to the neighbors around the first and last grains in the cluster, are tested as potential candidates for connecting to the current cluster through an incoherent Σ3 grain boundary. To be accepted into the Σ3 cluster, the potential candidate must not cause the current Σ3 cluster to exceed the target cluster size. If the potential grain belongs to a preexisting Σ3 cluster or a Σ3 cluster that was constructed during an earlier iteration step, the clusters are allowed to merge if the final cluster size does not exceed the target cluster size. When two Σ3 clusters need to be merged, the grain orientations of the smaller-sized

cluster will be rotated such that the grain boundary between the two clusters will be an incoherent Σ3 boundary. If the merged cluster was a preexisting cluster or if the single potential grain is accepted, annealing twins are synthesized in the accepted grain(s). All the boundaries surrounding the current cluster are then analyzed to ensure that if any rotations performed on the grain orientations generated new Σ3 boundary relationships, the related grains are included in the current cluster count. The procedure of finding potential candidates to add to the cluster is then repeated until either the current cluster size is larger or equal to the current target cluster size or no grains can be added further to the current cluster. The pseudo code for the algorithm can be found in Algorithm 9.1.

An alternative to using Σ3 cluster sizes as the target for twin synthesis is to use only the number of twins as the target. When only a desired number of twins is declared, the algorithm randomly chooses the grains in the structure and performs the same twin insertion method outlined above. Once twins are synthesized in a grain, the grain is removed from the list of potential grains for inserting the next set of twins.

Input: Structure, list of target cluster size, and list of preexisting Σ3 clusters

Output: Structure with annealing twins

```
for number of target clusters, do
    Define target cluster size from input
    if current cluster size = 0
        if preexisting cluster exist and is smaller than target cluster size, then
            adopt preexisting cluster into current cluster list
            insert twins in the grains that reside in the preexisting cluster
        else
            randomly pick a grain and insert twins
        end
     else
        while current cluster size < target size do
            check all boundaries surrounding cluster to ensure all Σ3 have been accounted for
            for neighbors of all grains in current cluster do
```

```
                if neighbor is part of preexisting cluster and adoption will not exceed target size, do
                    adopt neighbor and preexisting cluster into current cluster list
                    insert twins in the newly adopted grains
                else
                    randomly pick a neighbor to adopt and insert twin
                end
            end for
        end while
    end
end for
```

Algorithm 9.1 The method for creating annealing twins in the structure to match Σ3 cluster distributions.

9.2 Controlling Twin Width and Placement of the Annealing Twin

The variables of tolerance and D found in Equations 9.1 and 9.3 allow the control of twin width and the location of the annealing twin respectively. Figure 9.2a to c shows the increase in twin width or twin thickness as the tolerance value is increased from 0.5 to 3.0. Because the method of inserting the twins only relies on performing a dot product between the voxel positions and the <111> normal, there are no resolution concerns associated with the twin width. The only concern involved with choosing an inappropriate tolerance value is that if the chosen parent grain is small, a large tolerance value may convert the entire parent grain to a "twin" grain, while a small tolerance value may result in creating a twin that consists of a string of 5 voxels. Therefore, a reasonable tolerance value is in the range of 0.5 to 2.

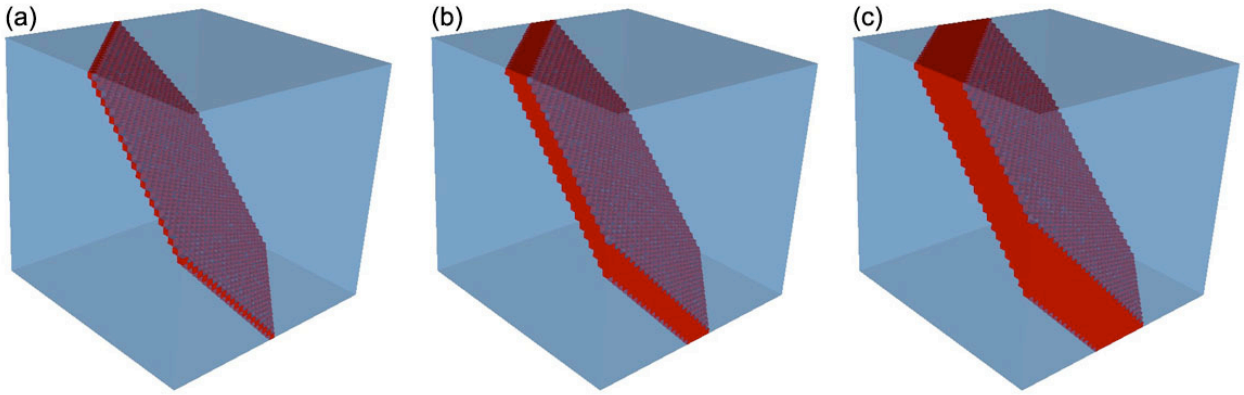

Figure 9.2 Synthesized twin grain (red) with D=0 and tolerance values of (a) 0.5, (b) 1.5, and (c) 3.0.

Figure 9.3 shows the various placements of the synthesized twin (colored in red) as the distance from the center of the grain, D, is changed. The green colored twin in Fig. 9.3 represents a twin that is inserted with D=0. From Fig. 9.3, it is clear that the variable D is a direct representation of the number of voxels to shift the center of the twin grain from the center of the parent grain. As can be seen in Fig. 9.3c, as the D value approaches the radius of the parent grain, the twin grain approaches the edges of the parent grain.

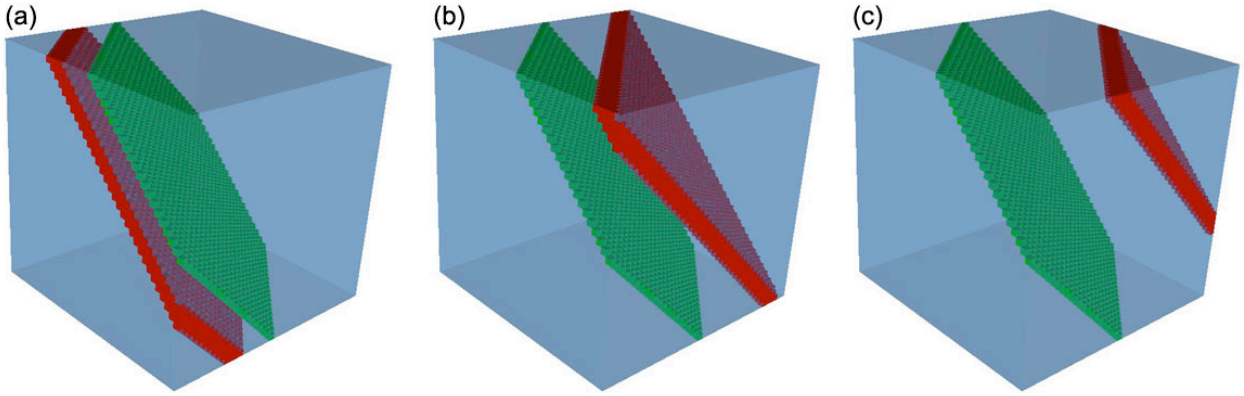

Figure 9.3 Synthesized twin grain (red) with tolerance=1.0 and D values of (a) -5, (b) 10, and (c) 20. The green twin grain marks the location of where the twin grain would be if D was set at 0.

Chapter 10 Case Study – Large Inconel 100

To demonstrate the capability of the twin insertion algorithm, the large experimental Inconel 100 structure was processed to remove the twin grains and was then regenerated with the twin insertion algorithm. The texture measurements and twin statistics mentioned in Chapter 6 are used as quantitative measures for determining whether the twin insertion algorithm was able to match the statistics observed in the experimental structure.

10.1 Characterization of the Large Inconel 100 Structure

The large Inconel 100 structure consists of 8518 grains, and is shown in Fig. 10.1. As seen in Fig. 10.1, the Inconel 100 structure contains a substantial populations of annealing twins.

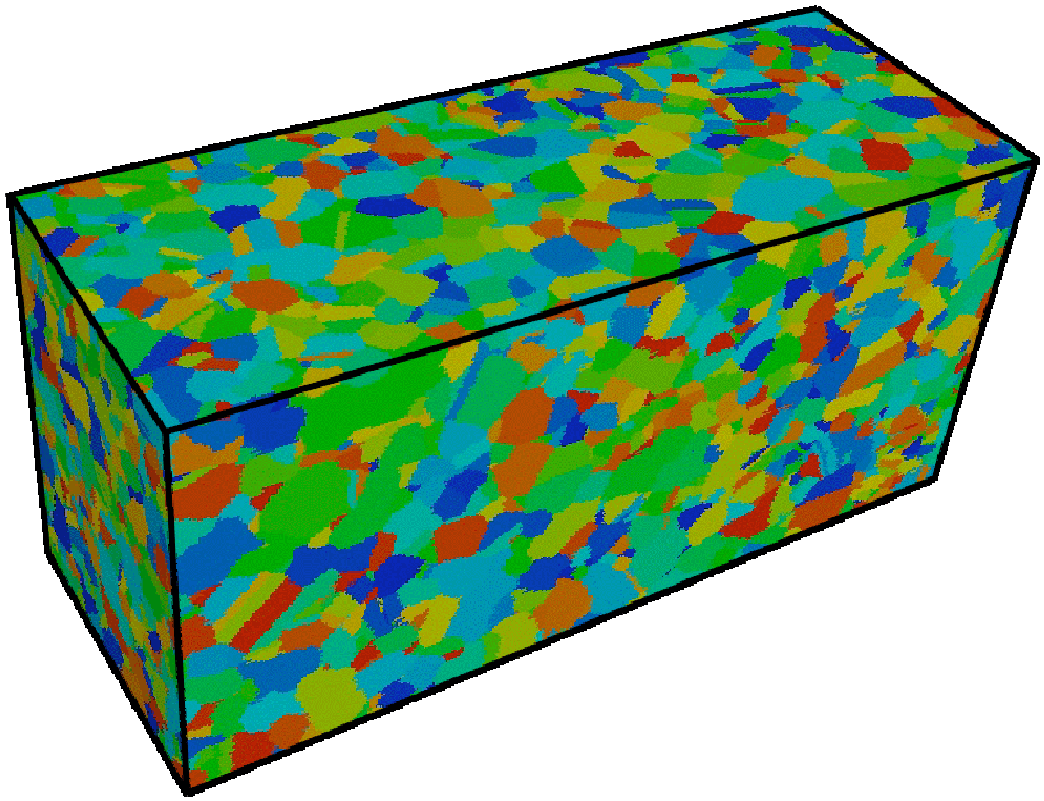

Figure 10.1 The large Inconel 100 structure that consists of 8518 grains with dimensions (389 x 146 x 184 voxels).

10.1.1 Texture and GBCD Measurements

The pole figures for the large Inconel 100 structure is shown in Fig. 10.2. As seen in the pole figures, random texture is found in the material. The GBCD for the Inconel 100 structure is plotted in Fig. 10.3. The GBCD plots indicate the relative areas of the boundaries with the specified misorientation and interface normals. The 900 MRD peak observed in the Σ3 plot is found at the location where the [111] vector is located on the stereogram. Therefore, a relatively high area fraction of coherent Σ3 or twin boundaries were found in the material. A slightly higher than random area fraction of Σ7 and Σ11 grain boundaries were also found.

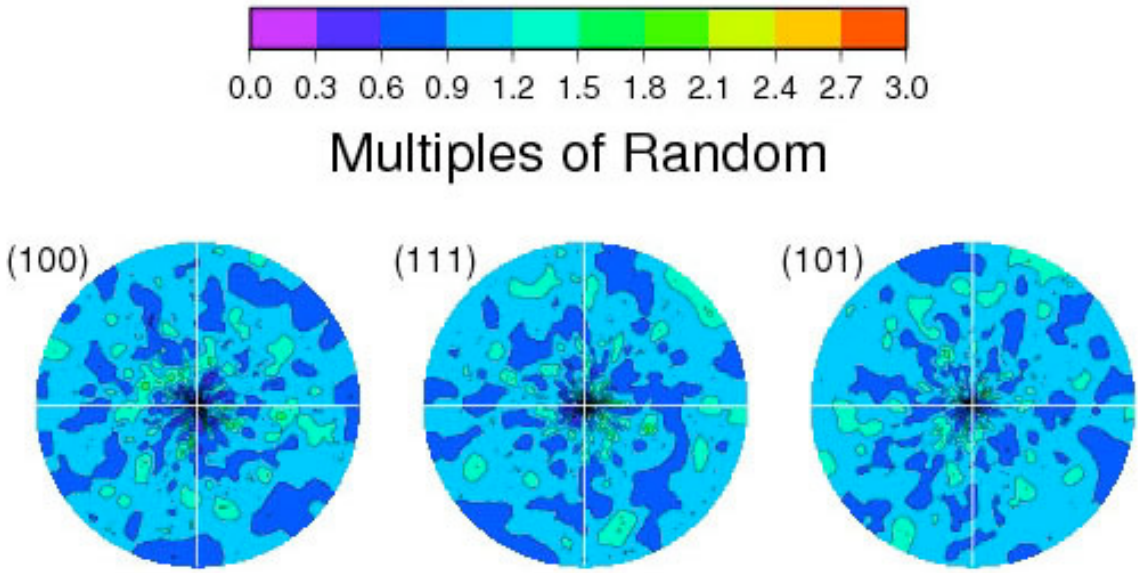

Figure 10.2 Pole figures indicating a random texture was measured in the large Inconel 100 structure.

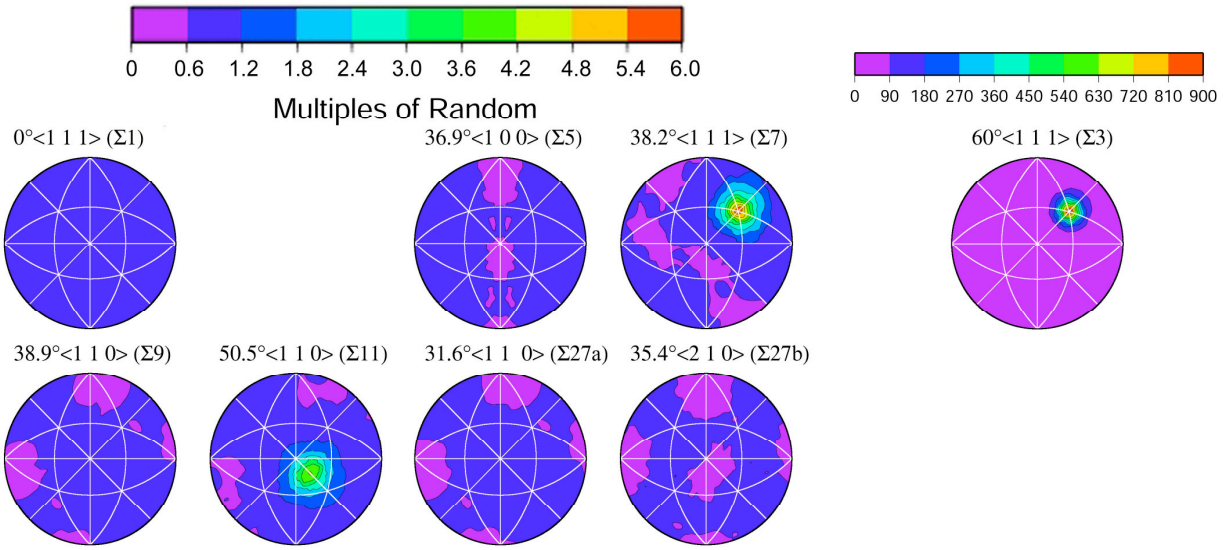

Figure 10.3 GBCD plots measured in the large Inconel 100 structure showing a very high population of coherent Σ3 grain boundaries while there is a slightly higher population of Σ7 and Σ11 boundaries than the other CSL boundaries.

10.1.2 Σ3 and Twin Boundary Fractions

As mentioned in Section 6.2, the number and length fractions of the Σ3 and twin boundaries are measured by analyzing the triangular elements of the smoothed conformed surface mesh. After the analysis, it was found that the number fractions of Σ3 and twin boundaries are 0.10 and 0.07 respectively. The area fractions of Σ3 and twin boundaries are 0.27 and 0.18 respectively in the experimental structure. The twin boundary fractions will always have a lower value than the fractions of all Σ3 boundaries since the twin boundaries have the additional coherency requirement. When comparing the difference between number and area fraction, the number fraction is much smaller than the area fractions for both the Σ3 and coherent Σ3 boundaries. This indicates that the Σ3 boundaries have a larger average area than other boundary types.

10.1.3 Σ3 Cluster Distribution

The Σ3 cluster distributions measured from the large experimental Inconel 100 structure with the correct grain orientations and with randomly assigned grain orientations are shown in Fig. 10.4. The Σ3 cluster distribution for the experimental structure shown in Fig. 10.4 is used as the target distribution for the twin insertion algorithm. It should be noted that when the experimentally collected grain orientations were used, the largest Σ3 cluster is 98 grains, but when random grain orientations were used, the largest Σ3 cluster is 9 grains. The high frequency of two-grain clusters indicates that many incoherent Σ3 boundaries were found in the structure. On the other hand, the high frequency of three-grain clusters can be attributed to the case where the parent grain has a single twin grain that separates the two halves of the original (single) grain.

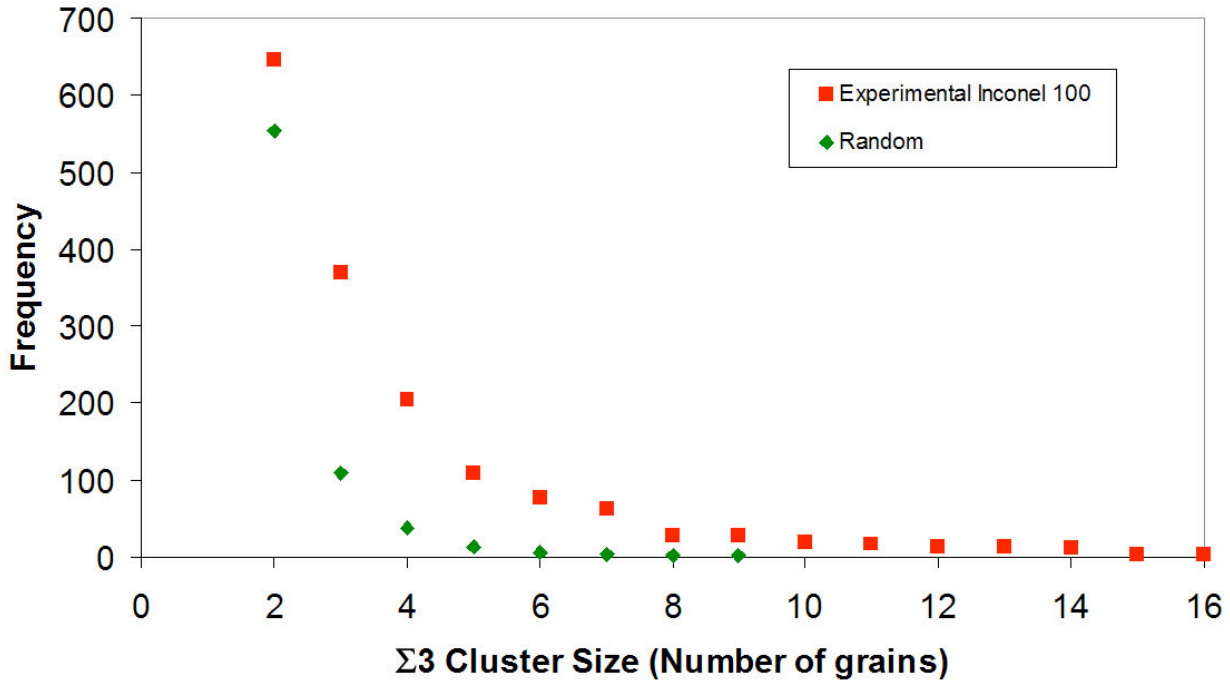

Figure 10.4 Σ3 cluster size distribution measured from the large experimental Inconel 100 structure. It should be noted that the largest cluster size found was 98 grains where as for a random set of orientations, the maximum cluster size is only 9.

10.1.4 Grain Size

The average spherical equivalent radii measured for the large experimental Inconel 100 structure with the twins identified as individual grains and with the twins ignored are 5.41 voxels and 5.91 voxels respectively. As mentioned in Section 6.4.1, the average grain size obtained with the twin grains included will yield smaller grain sizes, as consistent with the current values. The spherical equivalent grain size distributions for the experimental structure with and without including the twins as grains are shown in Fig. 10.5. The two spherical equivalent radius distributions are very similar to each other with the exception that a higher fraction of the relatively larger grains can be found in the distribution where the twins were ignored. The number fraction of grains with radii of approximately 2 voxels appears to be constant in the two distributions obtained with and without including the twin grains. This is an indication that grains with radii measurements of approximately 2 voxels and below do not contain twin grains.

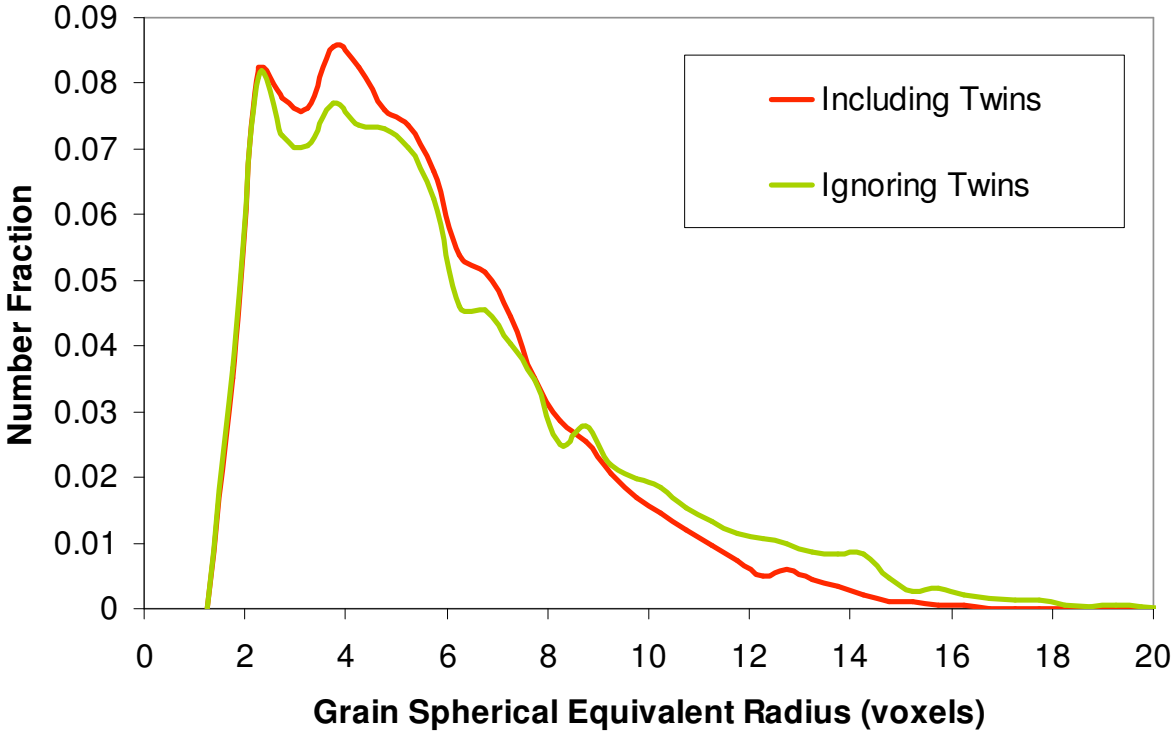

Figure 10.5 The normalized grain spherical equivalent grain size distribution for the experimental Inconel 100 structure with the twins included as individual grains and with the twins ignored.

10.1.5 Twin Density

The average twin density measured from the large Inconel 100 structure is 2 twins per grain, and the number fractions of twin clusters that have the corresponding number of twins per grain is shown in Fig. 10.6. The plot in Fig. 10.6 indicates that the limit of inserting a maximum of 6 twins in any grain in the twin insertion algorithm is a reasonable value since there are very few grains that contain more than 6 twins in the Inconel 100 structure.

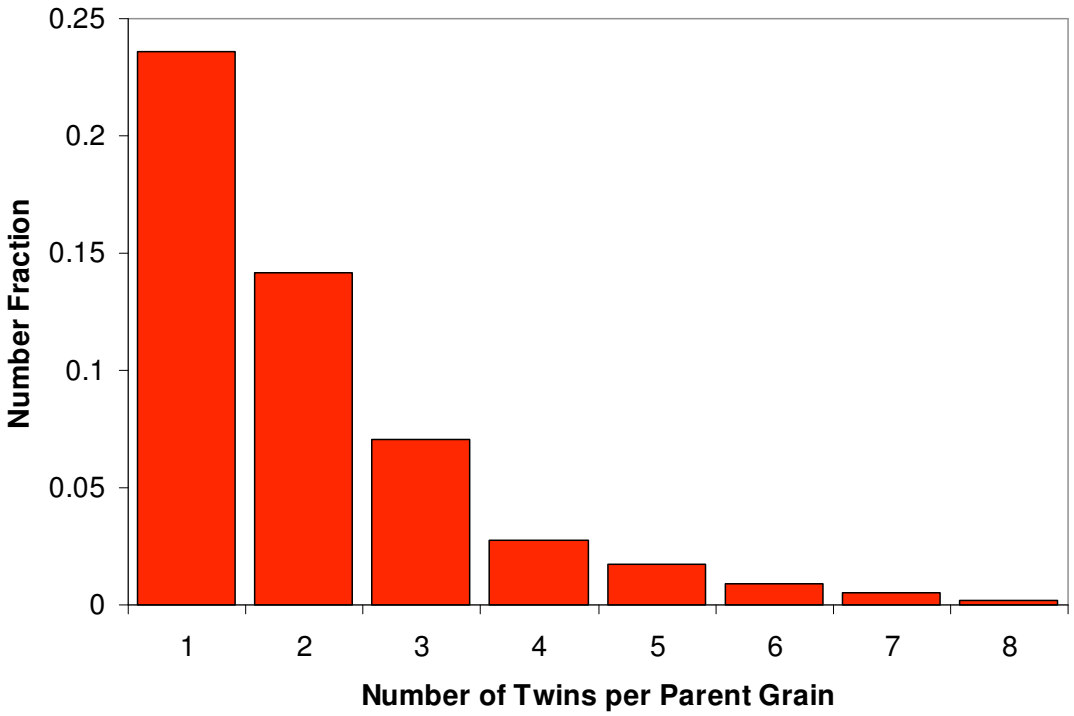

Figure 10.6 Number fractions of twin clusters that have the corresponding number of twins per parent grain found in the large experimental Inconel 100 structure.

10.2 Twin Grain Removal

The removal of the twin grains from the large Inconel 100 structure resulted in the cleaned structure shown in Fig. 10.7 that consists of 5665 grains. Texture and GBCD measurements for the cleaned structure can be found below in Section 10.2.2. Other twin statistics, such as grain size and twin boundary fractions can be found throughout Section 10.3.

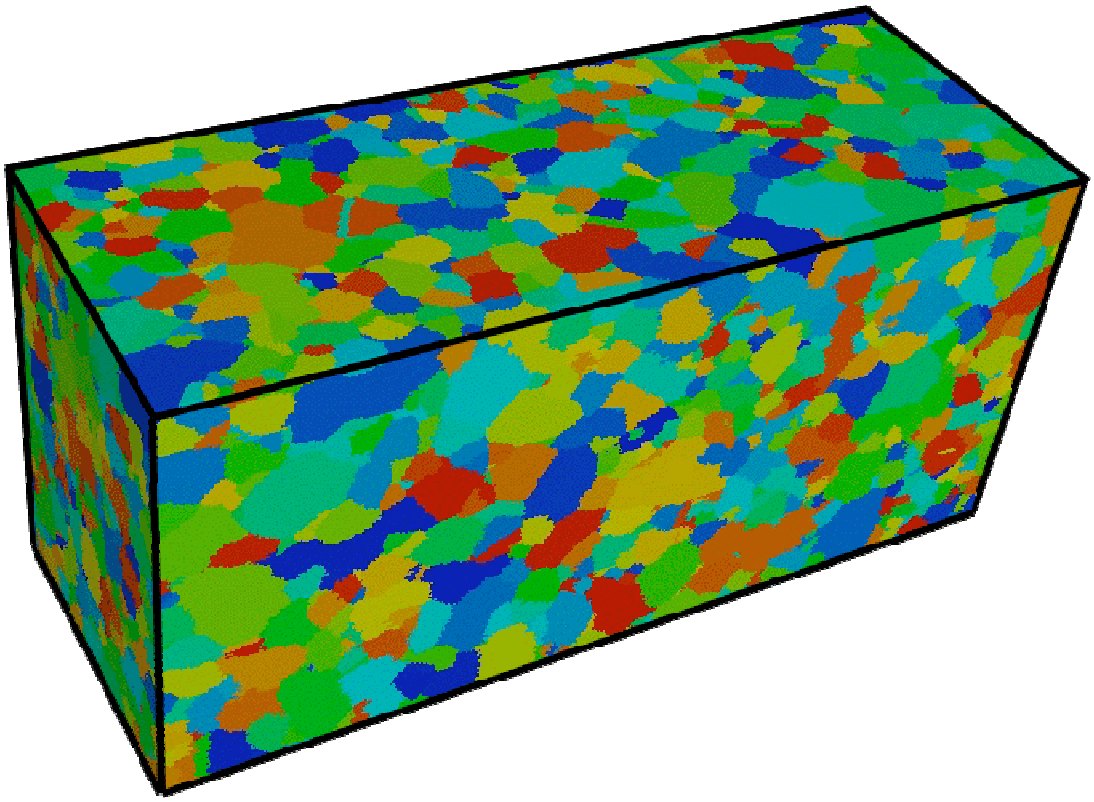

Figure 10.7 The cleaned structure after having the twin grains removed by the technique outlined in Section 6.4.1. The cleaned structure contains 5665 grains.

10.2.1 Classification of Coherent Σ3 Boundaries

The twin removal method described in Section 6.4.1 relies on the ability to identify coherent Σ3 grain boundaries in the structure. A triangular element is considered coherent when the angle between the misorientation axis and the interface normal is less than 15°. Since the smoothed conformed surface mesh contains artifacts, the mesh of a truly incoherent Σ3 boundary may contain a few coherent triangles while not all the triangular elements that make up a truly coherent boundary may pass the coherency test. Fig. 10.8 shows the frequency of boundaries having specified fractions of coherent Σ3 triangular elements. As seen in Fig. 10.8, most of the coherent boundaries have approximately 0.7 of their respective triangular elements satisfying the coherent Σ3 relationship. Various threshold fractions can then be chosen to limit the number of

boundaries that will be classified as coherent Σ3 boundaries. The twin cluster distributions were evaluated after imposing the various threshold fraction values on the classification of twin boundaries, and are shown in Fig. 10.9. As the threshold value increases from 0 to 0.5, the frequency of large grain clusters decreases while the two-grain clusters increases. This is due to the elimination of incorrectly classifying some of the incoherent Σ3 boundaries as twin boundaries. When the threshold value becomes 0.7 however, the criteria is too restrictive and truly coherent Σ3 boundaries are being ignored. For that reason, not enough twin boundaries were correctly classified, and twin clusters of all sizes decrease in frequency.

After identifying the coherent Σ3 boundaries with the threshold for coherent triangular elements set at 0.5, the triangular elements that belong to these boundaries were isolated and plotted in the GBCD plot shown in Fig. 10.10. As evident in Fig. 10.10, the coherent Σ3 boundaries were correctly identified.

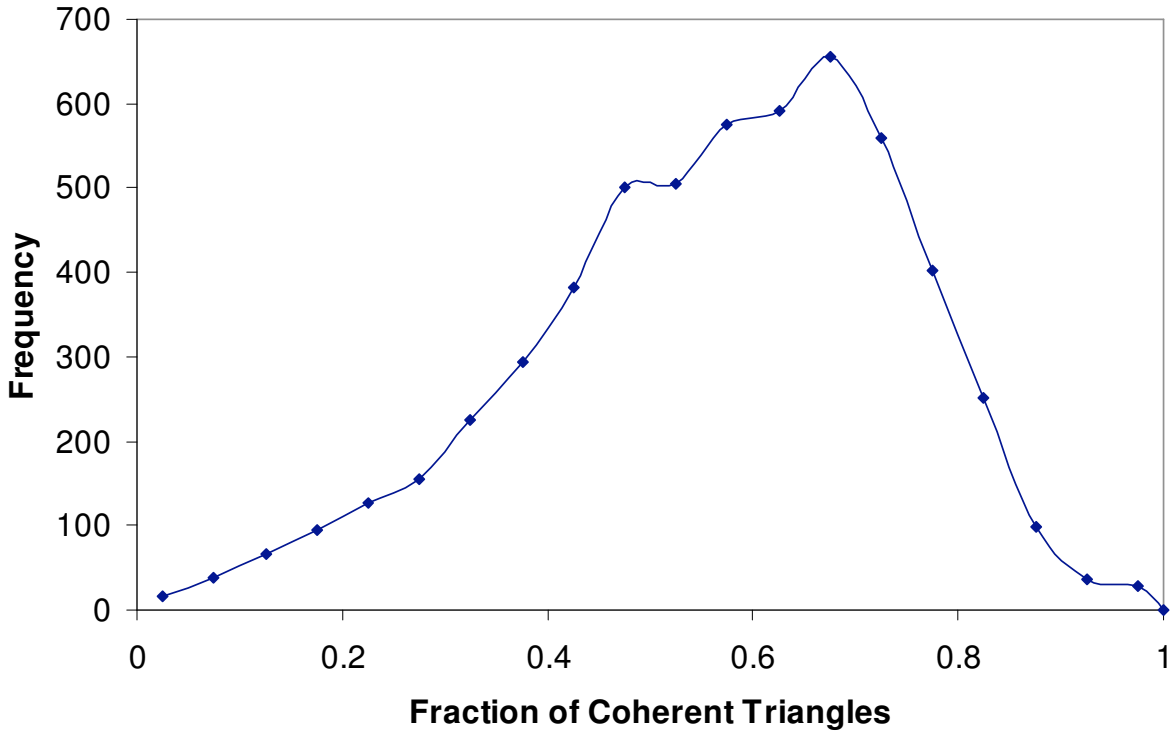

Figure 10.8 The number of grain boundaries found with the corresponding fraction of triangles that have the coherent Σ3 relationship.

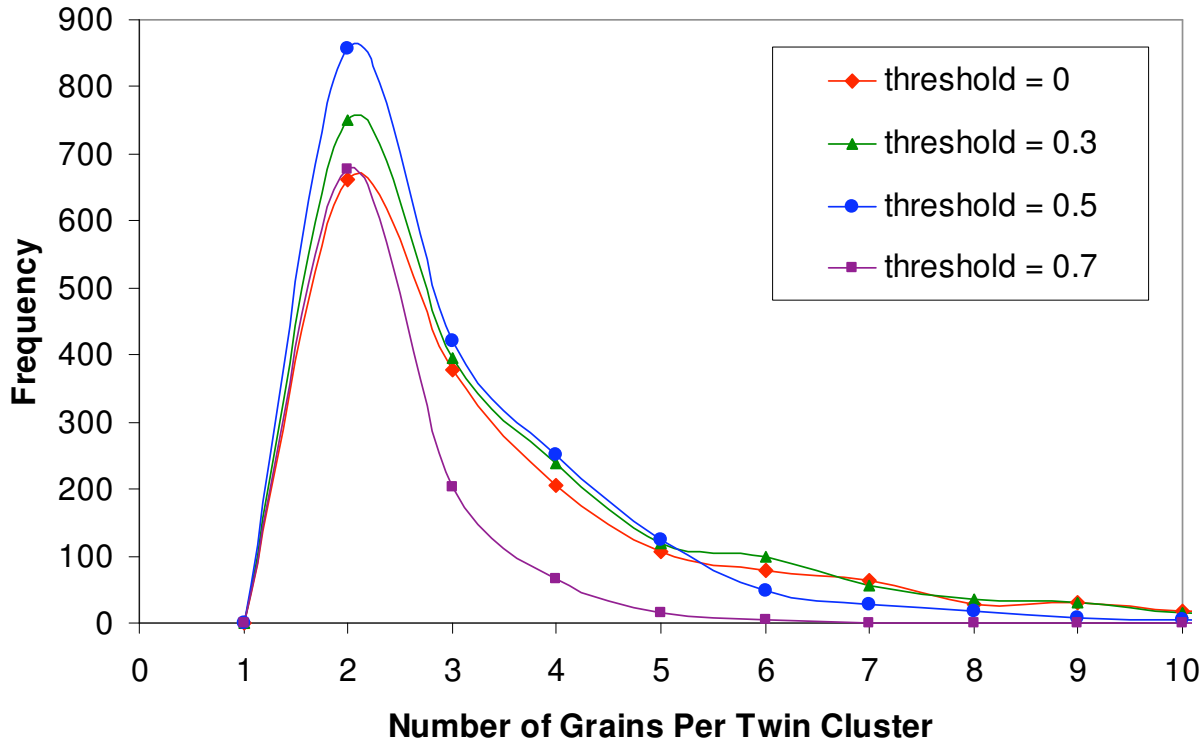

Figure 10.9 The number of twin clusters containing the corresponding number of grains.

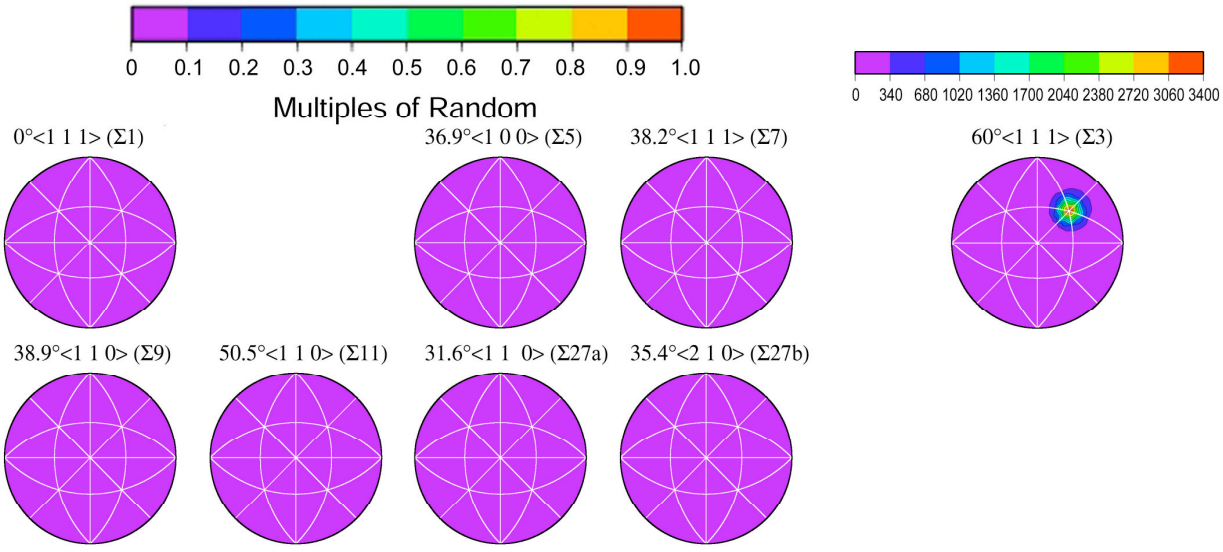

Figure 10.10 GBCD plots showing the grain boundaries that were identified as coherent Σ3 boundaries and removed from the experimental Inconel 100 structure.

10.2.2 Texture and GBCD Measurements

The pole figures and GBCD plots for the cleaned structure are shown in Figs. 10.11 and 10.12 respectively. As seen in Fig. 10.11, the texture is not significantly affected by the removal of the twin grains and the random texture remains after twin removal. In Fig. 10.12, it can be seen that the coherent Σ3 peak has been reduced from 900 MRD in the experimental structure to 200 MRD in the cleaned structure, indicating that a large portion of the twin boundaries have been removed. The remaining 200 MRD of twin boundaries is contributed by the coherent Σ3 triangular elements that were ignored during the classification of the coherent Σ3 boundaries.

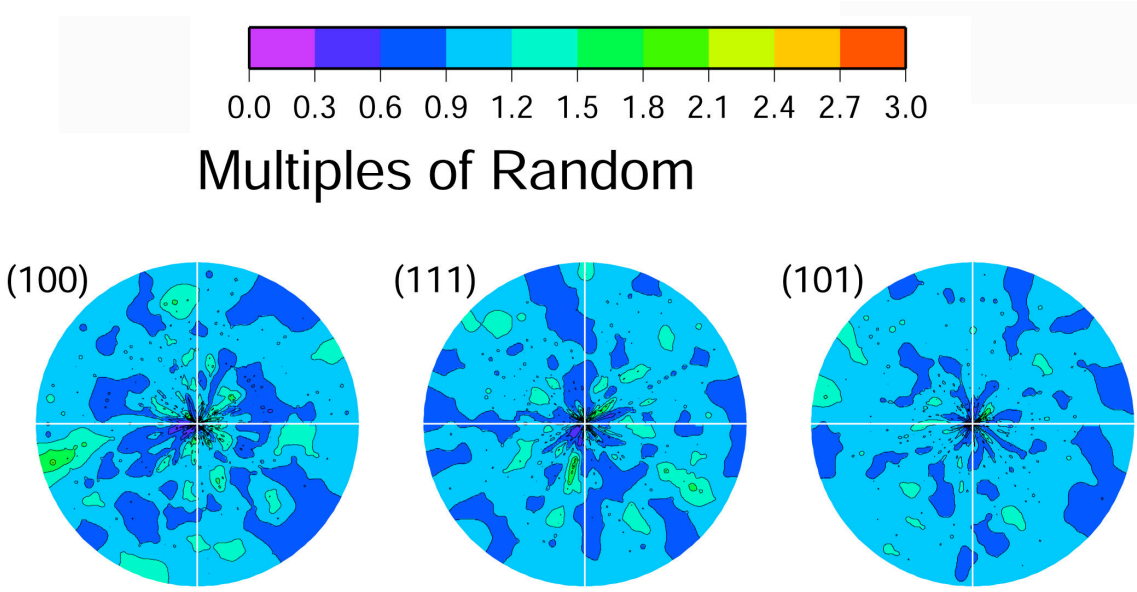

Figure 10.11 Pole figures showing random texture was measured from the cleaned structure (experimental Inconel 100 after twin grains have been removed).

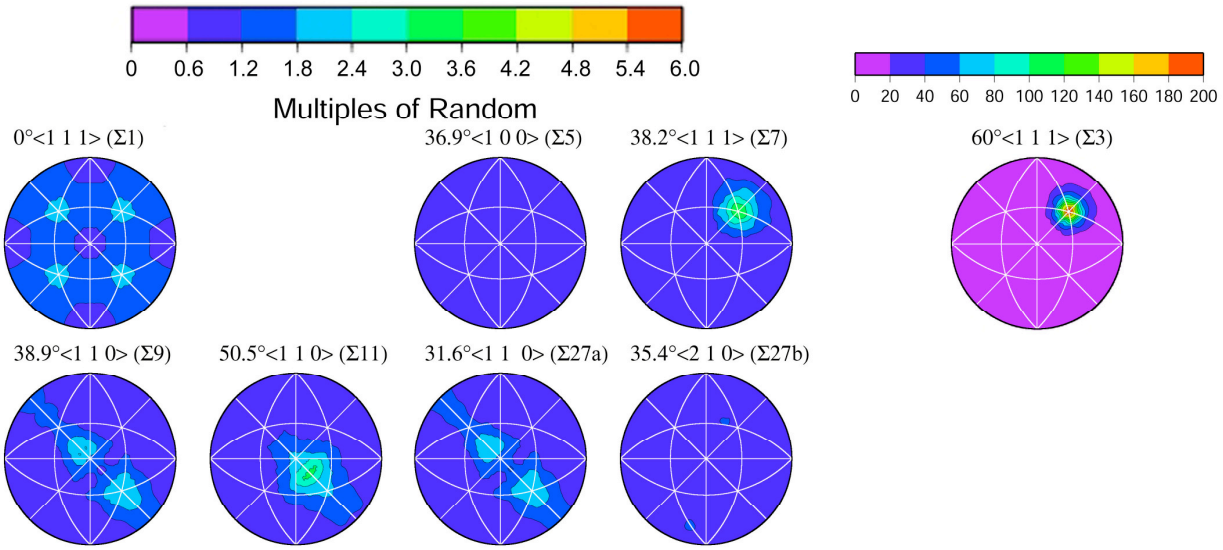

Figure 10.12 GBCD plots showing the remaining coherent Σ3 grain boundaries that were not removed by the twin grain removal method mentioned in Section 6.4.1.

10.2.3 Problems of the Twin Removal Technique

As is evident in Fig. 10.7, it appears that some twin grains have remained after the twin removal process. The top surface shown in Fig. 10.7 has been repeated in Fig. 10.13a. The twin and parent grain pair of interest is circled in black in Fig. 10.13a. The green colored twin grain and the orange colored parent grain can be seen in more detail in Fig. 10.13b, and with a rotated view in Fig. 10.13c. As observed in Fig. 10.13c, the green colored twin does not span the entire orange colored parent grain. The main assumption of the twin boundary identification algorithm is that all twin boundaries span the entire parent grain. Because the twin grain did not span the parent grain, the algorithm only sees one twin boundary since the grains on either side of the twin boundaries have the same identification number.

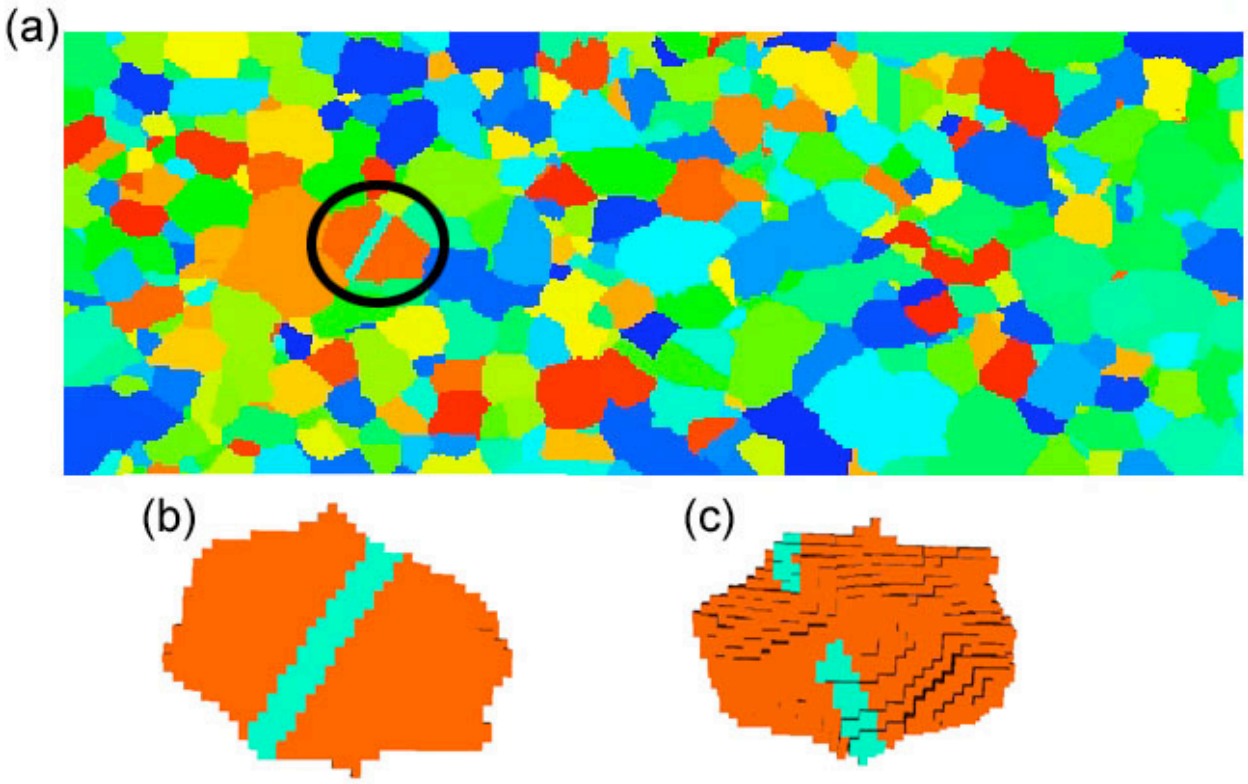

Figure 10.13 Demonstration of a twin grain that was not removed during the twin removal process. The twin-parent grain pair of interest is highlighted in (a) with the black circle, and is shown in (b), and with a rotated view in (c).

10.3 Twin Synthesis Results

After inserting twins into the cleaned structure, the twin inserted structure contains 7942 grains and is shown in Fig. 10.14. As seen in Fig. 10.14, many flat twin grains can be seen throughout the structure.

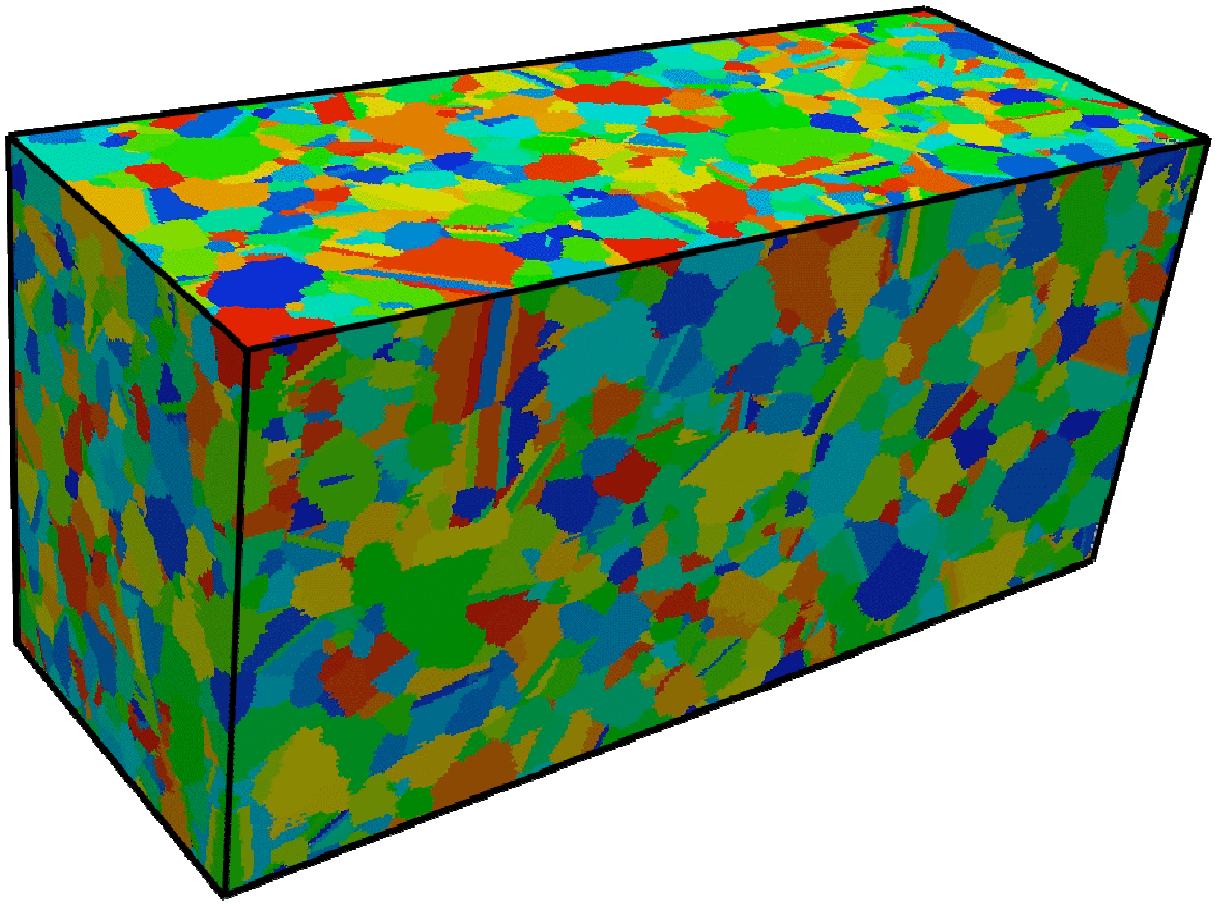

Figure 10.14 The twin inserted structure obtained by inserting twins into the cleaned structure of Inconel 100. The twin inserted structure contains 7942 grains.

10.3.1 Texture and GBCD Measurements

The pole figures and GBCD plots for the twin inserted structure are shown in Figs. 10.15 and 10.16 respectively. As seen in Fig. 10.15, the random texture observed previously in both the experimental and cleaned structure remains unchanged. In Fig. 10.16, it can be seen that the coherent Σ3 peak has increased from 25 MRD in the cleaned structure to 2000 MRD in the twin inserted structure, indicating that a large area fraction of coherent Σ3 boundaries have been created in the cleaned structure. The coherent Σ3 boundary population of 2000 MRD in the twin inserted structure is double the MRD value found in the experimental structure. The higher MRD value may be caused by the exact twin relationships used to create the annealing twins in

the structure. In the experimental structure, the uncertainty in measuring the grain orientations in the OIM and the cleanup procedures used on the structures creates coherent boundaries that can have both the lattice misorientation and boundary normal deviate from the exact twin boundary relationship. In the twin insertion algorithm, no deviation was allowed in the lattice misorientation or the boundary plane orientation. Hence in the GBCD plots for the twin inserted structure, the coherent Σ3 peak has less of a spread around the exact coherent Σ3 position than in the GBCD plots for the experimental structure.

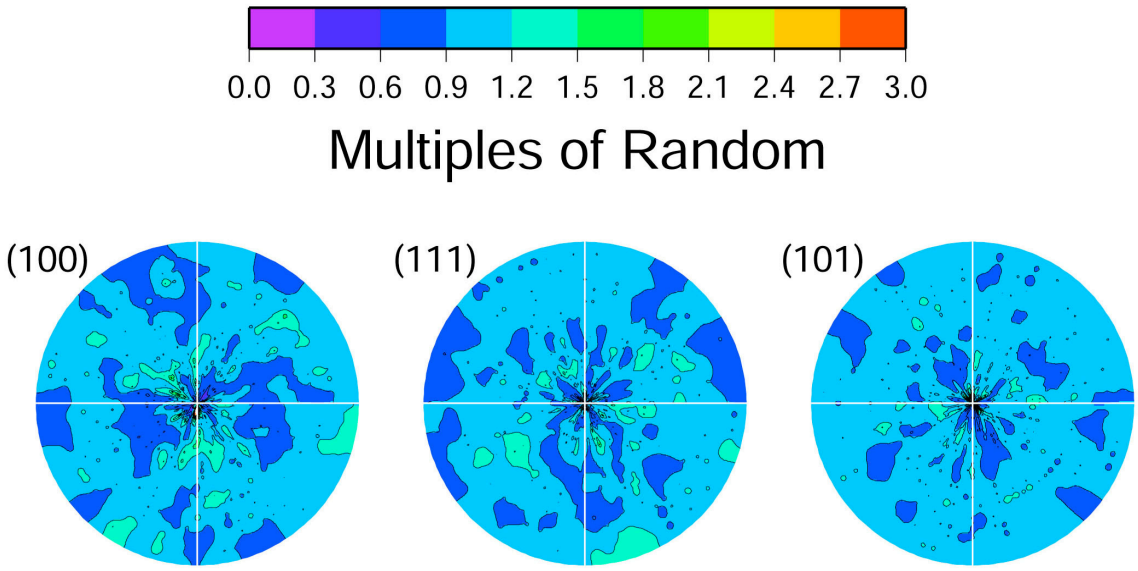

Figure 10.15 Pole figures indicating a random texture was obtained in the twin inserted structure.

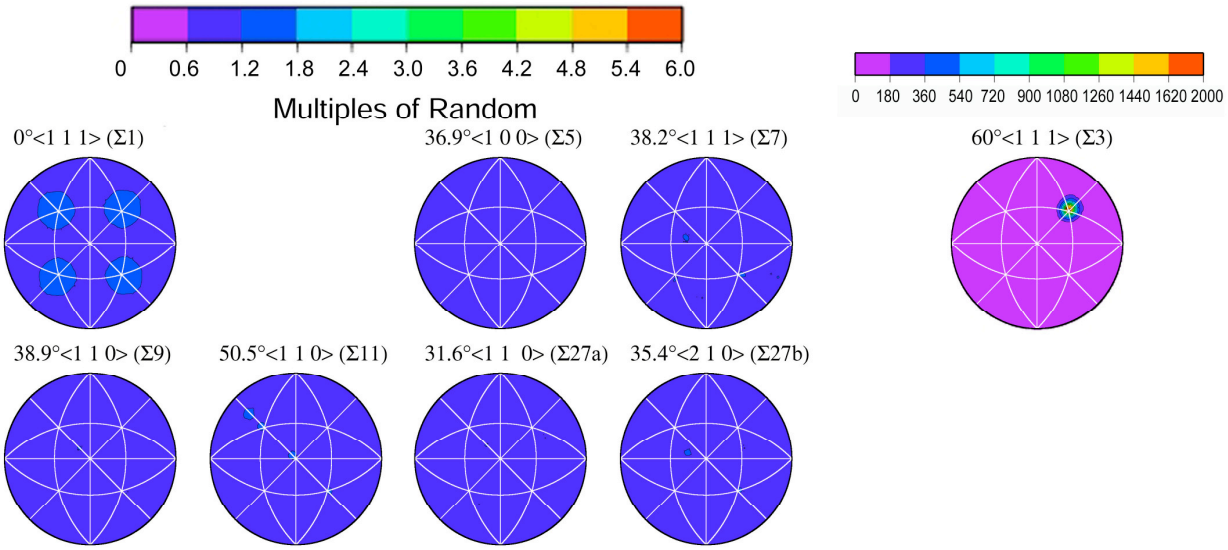

Figure 10.16 GBCD plots measured in the twin inserted structure showing a very high population of coherent Σ3 grain boundaries.

10.3.2 Σ3 and Twin Boundary Fractions

The number and area fractions of Σ3 and twin boundaries found in the experimental, cleaned, and twin inserted structures are summarized in Table 10.1. By comparing the number and area fractions of the Σ3 and twin boundaries for the cleaned structure and the experimental structure, it is clear that a high fraction of the coherent Σ3 boundaries were successfully removed from the experimental structure. The number and area fractions of both the Σ3 and twin boundaries between the experimental and twin inserted structures are very similar with only a maximum difference of 0.02. This indicates that the twin insertion code was very successful in creating both coherent and incoherent Σ3 boundaries in the cleaned structure.

Table 10.1 Summary of the number and area fractions of the Σ3 and twin boundaries found in the experimental, cleaned, and twin inserted structures.

	Number Fraction		Area Fraction	
Structure	**Σ3 boundaries**	**Coherent Σ3 boundaries**	**Σ3 boundaries**	**Coherent Σ3 boundaries**
Experimental Inconel 100	0.10	0.07	0.27	0.18
Cleaned Structure	0.09	0.03	0.09	0.05
Twin Inserted Structure	0.09	0.06	0.25	0.20

10.3.3 Σ3 Cluster Distribution

The Σ3 cluster distributions measured in the experimental, cleaned, and twin inserted structures are plotted in Fig. 10.17. As seen in the plot, after the removal of the twins, the Σ3 cluster distribution observed in the cleaned structure becomes very similar to a distribution expected with randomly oriented grains. It should be noted that the largest cluster size found in the experimental Inconel 100 consists of 98 grains while the largest cluster size found in the twin inserted structure consists of 103 grains. Since the Σ3 cluster distribution measured in the experimental Inconel 100 was used as the target distribution for twin insertion, it is not surprising that the two Σ3 distributions observed in the two structures should be so similar. However, the major differences to note are that the twin inserted structures contains a higher frequency of three-grain clusters and much lower frequency of four-grain clusters. The reason for this discrepancy may be that a four-grain Σ3 cluster requires insertion of one twin in an isolated pair of grains, which is more difficult to perform when compared to inserting a twin in one isolated grain to form a three-grain Σ3 cluster.

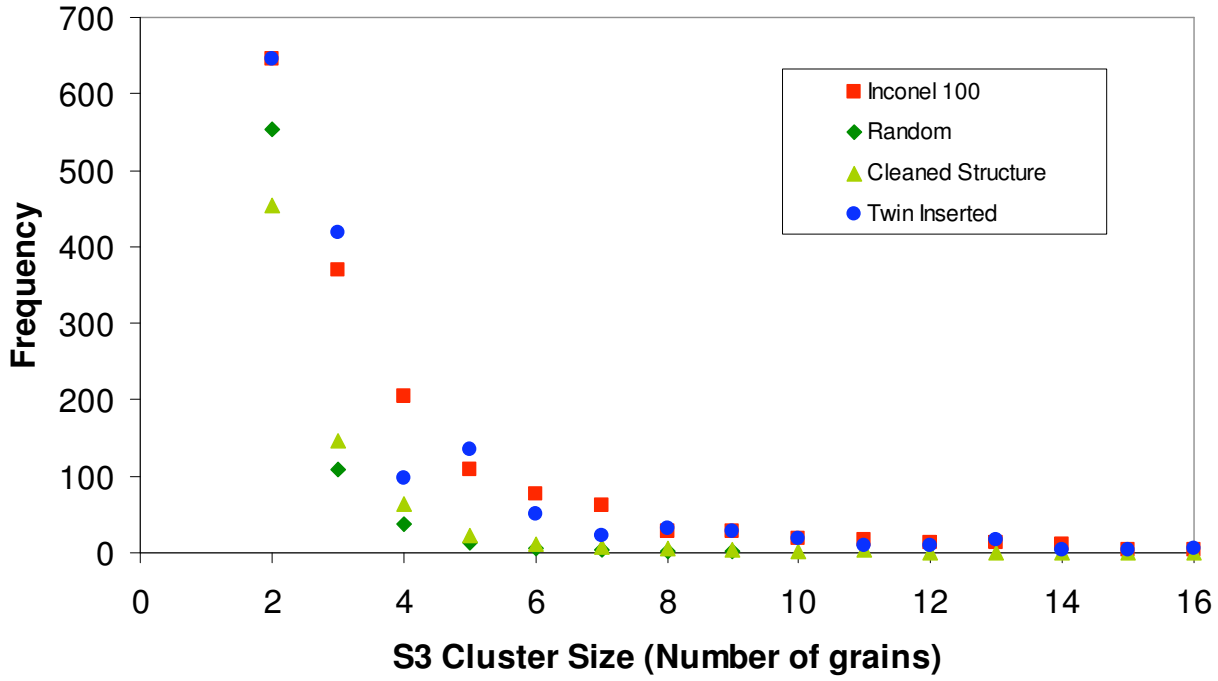

Figure 10.17 Σ3 cluster size distributions measured from the large experimental Inconel 100, the experimental Inconel 100 structure with random orientations, cleaned, and the twin inserted structures. It should be noted that the largest cluster size found for the experimental Inconel 100 is 98 grains, for a random set of orientations is 9 grains, for the cleaned structure is 17 grains, and for the twin inserted structure is 103 grains.

10.3.4 Grain Size

The average spherical equivalent radius measured for the twin inserted structure is 5.51 voxels. Since the twins were included in the average grain size measurement, the value is skewed towards a smaller grain size as compared to the average spherical equivalent radius of 5.91 voxels observed in the cleaned structure. The spherical equivalent grain size distributions for the experimental, cleaned, and twin inserted structures are shown in Fig. 10.18. As seen in Fig. 10.18 the grains found in the twin inserted structures have a more uniform distribution than the cleaned or experimental structures. This is because the twin insertion algorithm inserts twin grains of a fixed thickness into the cleaned structure. If a distribution of twin thicknesses were

inserted, the grain size distribution would become more spread out and approach closer to the distributions observed for the experimental structure.

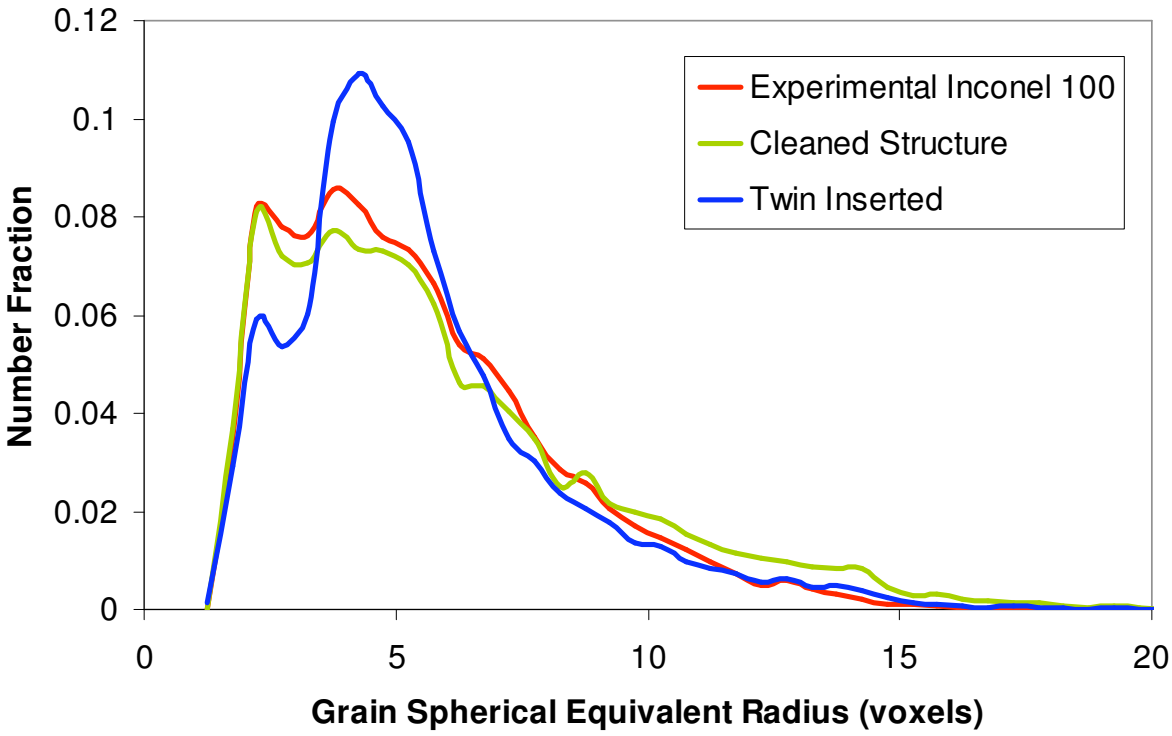

Figure 10.18 The distribution of spherical equivalent radius of the grains obtained from the experimental Inconel 100, cleaned, and twin inserted structures.

10.3.5 Twin Density

The average twin density measured from the twin inserted structure is two twins per grain, which is the same as the value observed in the Inconel 100 structure. However, from observing the number fractions of twin clusters that have the corresponding number of twins per grain in Fig. 10.19, there is a much higher fraction of twin clusters that have one twin per parent grain than the values observed for the Inconel 100 structure. Consequently, the fractions of twin clusters that have 2 or more twins per parent grain are lower than the values observed in the experimental structure. Despite the attempt to insert up to 6 twins per parent grain in the twin

insertion algorithm, perhaps the restriction of not allowing twins to reside within 3 voxels of each other is too high a threshold value.

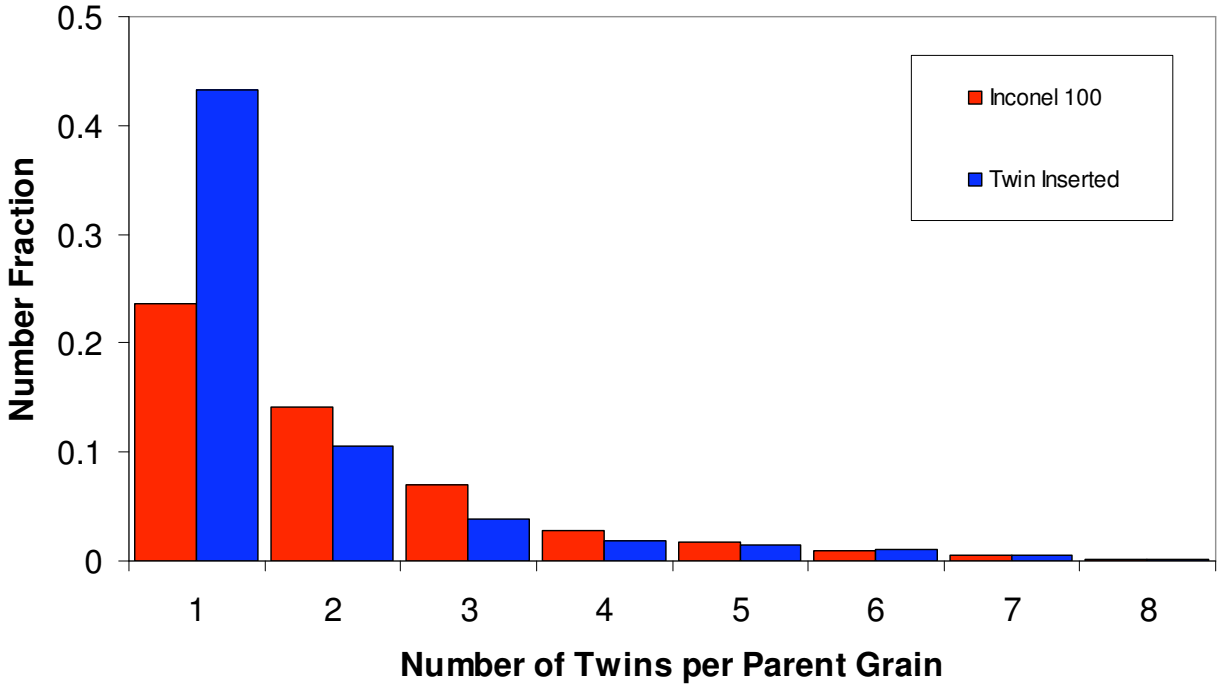

Figure 10.19 Number fractions of the number of twins found per parent grain in the experimental and twin inserted microstructures.

Chapter 11 Conclusions

By eliminating (or decreasing) the need to perform multiple thermal mechanical treatments on a material, computer simulation can speed up or make more thorough the study of the relationship between the GBCD and the material properties. However, before these material property simulations can be performed, statistically representative microstructures, especially ones that contain annealing twins, must first be generated. This dissertation focuses on creating synthetic microstructures that match the five-parameter GBCD obtained from experimentally observed microstructures.

The main algorithm used in this dissertation is the grain orientation assignment algorithm. The orientation assignment algorithm has the capability to match the OD and the MD or the GBCD simultaneously. The inclusion of weight variables in the simulated annealing method allows for user specification of the degree of matching in the OD and MD or GBCD.

Through assigning grain orientations with using different textures and MD as the target distributions, a relationship was found between the OD and MD. When the OD and MD are compatible with each other, both distributions can be fitted to the microstructures with ease. On the other hand, when incompatible orientation and misorientation distributions are used as targets to fit in a structure, a compromise must be made. The matching of the OD and MD is also dependent on the grain structure. Even though the change of grain shape and grain size distribution had no measurable effect on the fitting of the OD and MD, the microstructural feature that most strongly affects the fitting is the number of neighbors shared per grain or an equivalent number of facets per grain.

Even though an experimental GBCD was successfully fitted to a synthetic microstructure, the target and output GBCDs only matched qualitatively. Quantitatively, it is impossible for a

microstructure with equiaxed grains to attain the same area fraction of coherent Σ3 boundaries as a microstructure that is dominated with twin grains. Therefore, to achieve a high fraction of coherent Σ3 boundaries, additional twin boundaries must be created in the microstructure. During the investigation of fitting the GBCD to various microstructures, it was found that having a distribution of grain boundary areas allows closer fitting of both the OD and GBCD to a synthetic structure. However, a decrease in the number of neighbors shared per grain allows an easier matching of the OD and GBCD. Therefore, the neighbors per grain and grain boundary areas have significant effects on the possible OD and GBCD that can exist in the structure.

Through the case study of removing and regenerating annealing twins in the experimentally reconstructed Inconel 100, it was demonstrated that by using the Σ3 cluster distribution as the target, the twin insertion algorithm was able to match some of the experimentally observed statistics. Even though the random texture was maintained, a higher area fraction of coherent Σ3 boundaries was measured in the twin inserted microstructure as compared to the original experimental structure. The higher MRD of the coherent Σ3 boundary can be attributed to the lack of deviation allowed for the orientation of the boundary plane as well as the lattice misorientation. Since the twin insertion algorithm only regenerates Σ3 boundaries, the Σ7 and Σ11 distributions could not be matched to the experimental distributions. The twin inserted structure was able to match experimentally measured number and area fractions of Σ3 and coherent Σ3 boundaries to within a value of 0.01. The Σ3 cluster distributions obtained from the twin inserted structure and the experimental structure were very closely matched with the exception of the three-grain and four-grain clusters. By measuring the Σ3 cluster distribution, the largest cluster was found to contain 98 grains in the experimental

structure. Any observation of a two-dimensional section would not be able to reproduce the large cluster size that was observed in the fully-reconstructed 3D structure.

Chapter 12 Future Work

12.1 Grain Orientation Assignment Algorithm

In Section 8.8, the fitting of a rolling texture and a twin dominated GBCD to various microstructures indicated that the neighbors per grain and the distribution of grain boundary areas have an effect on the possible OD and GBCD that can exist in the structure. However, the exact relationship between the boundary areas, OD and GBCD are still unknown. If different microstructures with various distributions of boundary areas and neighbors per grain can be generated, further studies can be performed with the GBCD version of the grain orientation assignment algorithm to isolate the different microstructural parameters that may affect the possible GBCDs that can exist in the structures.

One of the major barriers involved with the GBCD version of the grain orientation assignment algorithm is that the time required by the code to perform the assignment is much too long for a single CPU. The GBCD version of the code requires a run time of approximately six days to fit a set of OD and GBCD to a 200x200x200 voxel structure that contains 1550 grains. The first step to optimizing the code is to use performance analysis tools to identify the time spent on each function, and subsequently adjust certain lines of the code such that the run-time of the program will decrease. The second step will involve parallelizing the code such that the work load can be distributed among multiple computers. Once the code is parallelized, the synthetic microstructure should be enlarged such that approximately 15,000 grains can be used to more accurately describe the GBCD. Therefore an estimate of three days will be needed to fit a set of OD and GBCD to a structure with 15,000 grains over 20 CPUs.

12.2 Twin Insertion Algorithm

Future work will involve fine tuning the variables involved in the twin insertion algorithm such that twin density and the distribution of grain sizes will match closer to the values observed in the experimental structure. Controlled deviations of the lattice misorientation and twin boundary plane orientation from the exact definition of a coherent Σ3 boundary can be included in the twin insertion algorithm to create a GBCD that is closer to the experimentally observed GBCD. Also, a distribution of twin thicknesses can be imposed on the twin grains such that the distribution of grain sizes will become more widely distributed following the experimental distribution.

12.3 Studies of Grain Boundary Networks

As mentioned in Section 6.3, the bond percolation theory is frequently used to analyze the percolation threshold [19, 119-127, 144]. In the future, the combination of the GBCD version of the grain assignment algorithm and the twin insertion algorithm will be able to generate many different grain boundary networks with various fractions of CSL boundaries. Percolation thresholds can then be easily analyzed as the five-parameter GBCD is varied. On a similar note, homology metrics can also be used to describe the connectivity of the CSL boundaries in the different grain boundary networks [145].

References

[1] Meyers, M. A. and K. K. Chawla. Imperfections: Interfacial and Volumetric Defects. *Mechanical Behavior of Materials.* Prentice-Hall, Inc., Uppder Saddle River, 247-290, 1999.

[2] Ohring, M. Structure of Solids. *Engineering Materials Science.* Academic Press, Inc., San Diego, 71-134, 1995.

[3] Randle, V. Grain Boundary Properties. *The Role of the Coincidence Site Lattice in Grain Boundary Engineering.* The Institute of Materials, London, 22-31, 1996.

[4] Davies, P. and V. Randle. Grain boundary engineering and the role of the interfacial plane. *Materials Science and Technology,* 17 (6): 615-626, 2001.

[5] Watanabe, T. An Approach to Grain Boundary Design for Strong and Ductile Polycrystals. *Res Mechanica,* 11 47-84, 1984.

[6] Aust, K. T., U. Erb and G. Palumbo. Interface Control for Resistance to Intergranular Cracking. *Materials Science & Engineering A - Structural Materials Properties Microstructure and Processing,* 176 (1-2): 329-334, 1994.

[7] Lehockey, E. M. On the creep behavior of grain boundary engineered nickel. *Materials Science and Engineering A - Structural Materials Properties Microstructure and Processing,* 237 (2): 168-172, 1997.

[8] Lin, H. and D. P. Pope. Weak Grain Boundaries in Ni_3Al. *Materials Science & Engineering A - Structural Materials Properties Microstructure and Processing,* 193 394-398, 1995.

[9] Gao, Y., M. Kumar, R. K. Nalla and R. O. Ritchie. High-cycle fatigue of nickel-based superalloy ME3 at ambient and elevated temperatures: Role of grain-boundary engineering. *Metallurgical and Materials Transactions A - Physical Metallurgy and Materials,* 36A (12): 3325-3333, 2005.

[10] Randle, V. Grain Boundary Planes. *The Role of the Coincidence Site Lattice in Grain Boundary Engineering.* The Institute of Materials, London, 65-83, 1996.

[11] Randle, V. The Role of the Grain Boundary Plane in Cubic Polycrystals. *Acta Materialia,* 46 (5): 1459-1480, 1997.

[12] Palumbo, G., K. T. Aust, U. Erb, P. J. King, A. M. Brennenstuhl and P. C. Lichtenberger. On Annealing Twins and CSL Distributions in FCC Polycrystals. *Physica Status Solidi A - Applied Research,* 131 (2): 425-428, 1992.

[13] Bi, H. Y., H. Kokawa, Z. J. Wang, M. Shimada and Y. S. Sato. Suppression of chromium depletion by grain boundary structural change during twin-induced grain boundary engineering of 304 stainless steel. *Scripta Materialia,* 49 (3): 219-223, 2003.

[14] Fang, X. Y., K. Zhang, H. Guo, W. G. Wang and B. X. Zhou. Twin-induced grain boundary engineering in 304 stainless steel. *Materials Science and Engineering A - Structural Materials Properties Microstructure and Processing,* 487 (1-2): 7-13, 2008.

[15] Michiuchi, M., H. Kokawa, Z. J. Wang, Y. S. Sato and K. Sakai. Twin-induced grain boundary engineering for 316 austenitic stainless steel. *Acta Materialia,* 54 (19): 5179-5184, 2006.

[16] Randle, V. Mechanism of twinning-induced grain boundary engineering in low stacking-fault energy materials. *Acta Materialia,* 47 (15-16): 4187-4196, 1999.

[17] Shimada, M., H. Kokawa, Z. J. Wang, Y. S. Sato and I. Karibe. Optimization of grain boundary character distribution for intergranular corrosion resistant 304 stainless steel by twin-induced grain boundary engineering. *Acta Materialia,* 50 (9): 2331-2341, 2002.

[18] Gertsman, V. Y. and S. M. Bruemmer. Study of Grain Boundary Character Along Intergranular Stress Corrosion Crack Paths in Austenitic Alloys. *Acta Materialia,* 49 (9): 1589-1598, 2001.

[19] Henrie, A. J., B. L. Adams and R. J. Larsen. Creating a model for percolation of grain boundaries in polycrystalline materials. *Materials Science Forum,* 408-412 (1): 419-424, 2002.

[20] Lin, H. and D. P. Pope. The Influence of Grain Boundary Geometry On Intergranular Crack Propagation in Ni_3Al. *Acta Metallurgica et Materialia,* 41 (2): 553-562, 1993.

[21] Tsurekawa, S., S. Nakamichi and T. Watanabe. Correlation of grain boundary connectivity with grain boundary character distribution in austenitic stainless steel. *Acta Materialia,* 54 (13): 3617-3626, 2006.

[22] Lehockey, E. M., A. M. Brennenstuhl and I. Thompson. On the relationship between grain boundary connectivity, coincident site lattice boundaries, and intergranular stress corrosion cracking. *Corrosion Science,* 46 (10): 2383-2404, 2004.

[23] Xia, S., B. X. Zhou and W. J. Chen. Grain Cluster Microstructure and Grain Boundary Character Distribution in Alloy 690. *Metallurgical and Materials Transactions A - Physical Metallurgy and Materials,* 40A (12): 3016-3030, 2009.

[24] Randle, V., G. S. Rohrer and Y. Hu. Five-parameter grain boundary analysis of a titanium alloy before and after low-temperature annealing. *Scripta Materialia,* 58 (3): 183-186, 2008.

[25] Randle, V., G. S. Rohrer, H. M. Miller, M. Coleman and G. T. Owen. Five-parameter grain boundary distribution of commercially grain boundary engineered nickel and copper. *Acta Materialia,* 56 (10): 2363-2373, 2008.

[26] Rohrer, G. S., V. Randle, C. S. Kim and Y. Hu. Changes in the five-parameter grain boundary character distribution in alpha-brass brought about by iterative thermomechanical processing. *Acta Materialia,* 54 (17): 4489-4502, 2006.

[27] Rohrer, G. S., D. M. Saylor, B. El Dasher, B. L. Adams, A. D. Rollett and P. Wynblatt. The distribution of internal interfaces in polycrystals. *Zeitschrift Fur Metallkunde,* 95 (4): 197-214, 2004.

[28] Bunge, H. J. Zur Darstellung Allgemeiner Texturen. *Zeitschrift Fur Metallkunde,* 56 (12): 872-874, 1965.

[29] Roe, R. J. Description of crystallite orientation in polycrystalline Materials III, general solution to pole figure inversion. *Journal of Applied Physics,* 36 (6): 2024-2031, 1965.

[30] Kocks, U. F. A symmetric set of Euler angles and oblique orientation space sections. Eighth International Conference on Textures of Materials, Warrendale, PA, 31-36, 1988.

[31] Rohrer, G. S. *Structure and Bonding in Crystalline Materials.* Cambridge University Press, Cambridge, UK, 2001.

[32] Smallman, R. E. and D. Green. Dependence of Rolling Texture On Stacking Fault Energy. *Acta Metallurgica,* 12 (2): 145-154, 1964.

[33] Kocks, U. F., C. N. Tomé and H.-R. Wenk. Relation between Pole Figures and the OD. *Texture and Anisotropy.* Cambridge University Press, Cambridge, U.K., 104-107, 1998.

[34] Hirsch, J. and K. Lücke. Mechanism of Deformation and Development of Rolling Textures in Polycrystalline FCC Metals 1. Description of Rolling Texture Development in Homogeneous CuZn Alloys. *Acta Metallurgica,* 36 (11): 2863-2882, 1988.

[35] Heinz, A. and P. Neumann. Representation of Orientation and Disorientation Data for Cubic, Hexagonal, Tetragonal and Orthorhomic Crystals. *Acta Crystallographica Section A,* 47 (6): 780-789, 1991.

[36] Frank, F. C. Orientation Mapping. *Metallurgical Transactions A - Physical Metallurgy and Materials Science,* 19 (3): 403-408, 1988.

[37] Rodrigues, O. Des lois géométriques qui régissent les déplacements d'un système solide dans l'espace, et de la variation des coordonnées provenant de ces déplacements considérés indépendamment des causes qui peruvent les produire. *Journal de Mathématiques,* 5 380-440, 1840.

[38] Kronberg, M. L. and F. H. Wilson. Secondary Recrystallization in Copper. *Transactions of the American Institute of Mining and Metallurgical Engineers,* 185 (8): 501-514, 1949.

[39] Humphreys, F. J. and M. Hatherly. *Recrystallization and related annealing phenomena.* Elsevier, Boston, 2004.

[40] Warrington, D. H. Formal Geometrical Aspects of Grain Boundary Structure. *Grain Boundary Structure and Kinetics.* American Society for Metals, ASM Metals Park, Ohio, 1-12, 1979.

[41] Ranganathan, S. On the Geometry of Coincidence-Site Lattices. *Acta Crystallographica,* 21 (2): 197-199, 1966.

[42] Mykura, H., P. S. Bansal and M. H. Lewis. Coincidence-Site-Lattice Relations for MgO-CdO Interfaces. *Philosophical Magazine A - Physics of Condensed Matter Structure Defects and Mechanical Properties,* 42 (2): 225-233, 1980.

[43] Read, W. T. *Dislocations in Crystals.* McGraw-Hill, New York, 1953.

[44] Read, W. T. and W. Shockley. Dislocation Model of Crystal Grain Boundaries. *Physical Review,* 78 (3): 275-289, 1950.

[45] Palumbo, G. and K. T. Aust. Structure-Dependence of Intergranular Corrosion in High-Purity Nickel. *Acta Metallurgical et Materialia,* 38 (11): 2343-2352, 1990.

[46] Brandon, D. G. Structure of High-Angle Grain Boundaries. *Acta Metallurgica,* 14 (11): 1479-1484, 1966.

[47] Ishibashi, R., T. Horiuchi, J. Kuniya, M. Yamamoto, S. Tsurekawa, H. Kokawa, T. Watanabe and T. Shoji. Effect of grain boundary character distribution on stress corrosion cracking behavior in austenitic stainless steels. *Materials Science Forum,* 475-479 (1-5): 3863-3866, 2005.

[48] Palumbo, G., P. J. King, K. T. Aust, U. Erb and Lichtenberger. Grain Boundary Design and Control for Intergranular Stress-Corrosion Resistance. *Scripta Metallurgica,* 25 (8): 1775-1780, 1991.

[49] Goux, C. Structure des joints de grains: considérations cristallographiques et méthodes de calcul des structures. *Canadian Metallurgical Quaterly,* 13 (1): 9-31, 1974.

[50] Fujita, H. and T. Mori. A Formation Mechanism of Mecahnical Twins in F.C.C. Metals. *Scripta Metallurgica,* 9 (6): 631-636, 1975.

[51] Mahajan, S., C. S. Pande, M. A. Imam and B. B. Rath. Formation of annealing twins in f.c.c. crystals. *Acta Materialia,* 45 (6): 2633-2638, 1997.

[52] Meyers, M. A. and L. E. Murr. Model for Formation of Annealing Twins in FCC Metals and Alloys. *Acta Metallurgica,* 26 (6): 951-962, 1978.

[53] Bystrzycki, J. and W. Przetakiewicz. 3-Dimensional Reconstructure of Annealing Twins Shape in FCC Metals by Serial Sectionning. *Scripta Metallurgica et Materialia,* 27 (7): 893-896, 1992.

[54] Bystrzycki, J., W. Przetakiewicz and K. J. Kurzydlowski. Study of Annealing Twins and Island Grains in F.C.C. Alloy. *Acta Metallurgical et Materialia,* 41 (9): 2639-2649, 1993.

[55] Autodesk, I. Autodesk - 2D and 3D Design and Engineering Software for Architecture, Manufacturing, and Digital Entertainment, [Online] Available at: http://usa.autodesk.com.

[56] Groeber, M. A., S. Ghosh, M. D. Uchic and D. M. Dimiduk. A Framework For Automated Analysis and Simulation of 3D Polycrystalline Microstructures. Part 1: Statistical Characterization. *Acta Materialia,* 56 (6): 1257-1273, 2008.

[57] Groeber, M. A., B. K. Haley, M. D. Uchic, D. M. Dimiduk and S. Ghosh. 3D reconstruction and characterization of polycrystalline microstructures using a FIB-SEM system. *Materials Characterization,* 57 (4-5): 259-273, 2006.

[58] Kirkpatrick, S., C. D. Gelatt and M. P. Vecchi. Optimization by Simulated Annealing. *Science,* 220 (4598): 671-680, 1983.

[59] Dunham, B., D. Frisdshal, R. Frisdshal and J. H. North. Design by natural selection. *Synthese,* 15 (1): 254-259, 1963.

[60] Lin, S. Heuristic programming as an aid to network design. *Networks,* 5 (1): 33-43, 1975.

[61] Metropolis, N., A. W. Rosenbluth, M. N. Rosenbluth and A. H. Teller. Equations of State Calculations by Fast Computing Machines. *Journal of Chemical Physics,* 21 (6): 1087-1092, 1953.

[62] Kirkpatrick, S. Optimization by Simulated Annealing: Quantitative Studies. *Journal of Statistical Physics,* 34 (5-6): 975-986, 1984.

[63] Press, W. H., S. A. Teukolsky, W. T. Vetterling and B. P. Flannery. Simulated Annealing Methods. *Numerical Recipes in C.* Cambridge University Press, New York, 444-445, 1992.

[64] *Annual Book of ASTM Standards.* ASTM International, West Conshohocken, PA, 2002.

[65] TSL. *OIM Version 4.6 OIM Analysis Help*. TSL, Draper, UT, 2006.

[66] Torquato, S. Computer Simulations, Image Analyses, and Reconstructions. *Random Heterogeneous Materials: Microstructure and Macroscopic Properties.* Springer-Verlag, New York, 269-302, 2002.

[67] Yeong, C. L. Y. and S. Torquato. Reconstructing random media II. Three-dimensional media from two-dimensional cuts. *Physical Review E,* 58 (1): 224-233, 1998.

[68] Yeong, C. L. Y. and S. Torquato. Reconstructing random media. *Physical Review E,* 57 (1): 495-506, 1998.

[69] Basanta, D., M. A. Miodownik, E. A. Holm and P. J. Bentley. Evolving 3D microstructures using a Genetic Algorithm. *Materials Science Forum,* 467-470 (1-2): 1019-1024, 2004.

[70] Basanta, D., M. A. Miodownik, E. A. Holm and P. J. Bentley. Using genetic algorithms to evolve three-dimensional microstructures from two-dimensional micrographs. *Metallurgical and Materials Transactions A - Physical Metallurgy and Materials,* 36A (7): 1643-1652, 2005.

[71] Rollett, A. D., S.-B. Lee, R. Campman and G. S. Rohrer. Three-dimensional characterization of microstructure by electron back-scatter diffraction. *Annual Review of Materials Research,* 37 627-658, 2007.

[72] Decker, L. and D. Jeulin. Simulation 3D de matériaux aléatoires polycristallins. *Revue de Metallurgie,* 97 (2): 271-275, 2000.

[73] Kanit, T., S. Forest, I. Galliet, V. Mounoury and D. Jeulin. Determination of the size of the representative volume element for random composites: statistical and numerical approach. *International Journal of Solids and Structures,* 40 (13-14): 3647-3679, 2003.

[74] Voronoi, G. Nouvelles applications des paramètres continus à la théorie des formes quadratiques. *Journal für die Reine und Angewandte Mathematik,* 133 97-178, 1908.

[75] Fan, Z. G., Y. G. Wu, X. H. Zhao and Y. Z. Lu. Simulation of polycrystalline structure with Voronoi diagram in Laguerre geometry based on random closed packing of spheres. *Computational Materials Science,* 29 (3): 301-308, 2004.

[76] Brahme, A., M. H. Alvi, D. M. Saylor, J. Fridy and A. D. Rollett. 3D reconstruction of microstructure in a commerical purity aluminum. *Scripta Materialia,* 55 (1): 75-80, 2006.

[77] Groeber, M. A., S. Ghosh, M. D. Uchic and D. M. Dimiduk. Developing a Robust 3-D Characterization-Representation Framework for Modeling Polycrystalline Materials. *JOM,* 59 (9): 32-36, 2007.

[78] Groeber, M. A., S. Ghosh, M. D. Uchic and D. M. Dimiduk. A Framework For Automated Analysis and Simulation of 3D Polycrystalline Microstructures. Part 2: Synthetic Structure Generation. *Acta Materialia,* 56 (6): 1274-1287, 2008.

[79] Saylor, D. M., J. Fridy, B. S. El-Dasher, K. Y. Jung and A. D. Rollett. Statistically representative three-dimensional microstructures based on orthogonal observation sections. *Metallurgical and Materials Transactions A - Physical Metallurgy and Materials Science,* 35A (7): 1969-1979, 2004.

[80] St-Pierre, L., E. Heripre, M. Dexet, J. Crepin, G. Bertolino and N. Bilger. 3D simulations of microstructure and comparison with experimental microstructure coming from O.I.M analysis. *International Journal of Plasticity,* 24 (9): 1516-1532, 2008.

[81] Pan, Y., B. L. Adams, T. Olson and N. Panayotou. Grain-boundary structure effects on intergranular stress corrosion cracking of Alloy X-750. *Acta Materialia,* 44 (12): 4685-4695, 1996.

[82] Field, D. P., H. Weiland and K. Kunze. Intergranular Cracking in Alumunium Alloys. *Canadian Metallurgical Quaterly,* 34 (3): 203-210, 1995.

[83] Ohfuji, T., S. Suzuki, S. Takaki and H. Kimura. Low-Temperature Fracture of High-Purity Iron and Its Relationship to the Grain-Boundary Character *Materials Transactions JIM,* 33 (2): 138-142, 1992.

[84] Miyamoto, H., K. Ikeuchi and T. Mimaki. The role of grain boundary plane orientation on intergranular corrosion of symmetric and asymmetric [110] tilt grain boundaries in directionally solidified pure copper. *Scripta Materialia,* 50 (12): 1417-1421, 2004.

[85] Carpenter, H. C. H. and S. Tamura. The formation of twinned metallic crystals. *Proceedings of the Royal Society of London Series A - Containing Papers of a Mathematical and Physical Character,* 113 (763): 161-182, 1926.

[86] Meyers, M. A. and C. McCowan. The Formation of Annealing Twins: Overview and New Thoughts. Interface Migration and Control of Microstructure, Detriot, Michigan, 99-123, 1984.

[87] Burke, J. E. The Formation of Annealing Twins. *Transactions of the American Institute of Mining and Metallurgical Engineers,* 188 (11): 1324-1328, 1950.

[88] Fullman, R. L. and J. C. Fisher. Formation of Annealing Twins During Grain Growth. *Journal of Applied Physics,* 22 (11): 1350-1355, 1951.

[89] Gleiter, H. Formation of Annealing Twins. *Acta Metallurgica,* 17 (12): 1421-1428, 1969.

[90] Baro, G. and H. Gleiter. Formation of Annealing Twins. *Zeitschrift Fur Metallkunde,* 63 (10): 661-663, 1972.

[91] Rath, B. B., M. A. Imam and C. S. Pande. Nucleation and Growth of Twin Interfaces in FCC Metals and Alloys. *Materials Physics and Mechanics,* 1 (2): 61-66, 2000.

[92] Farkas, D., E. Bringa and A. Caro. Annealing twins in nanocrystalline fcc metals: A molecular dynamics simulation. *Physical Review B,* 75 (18): 1-5, 2007.

[93] Burgers, W. G. Stimulation Crystals and Twin Formation in Recrystallized Aluminum. *Nature,* 157 (3977): 76-77, 1946.

[94] Burgers, W. G. Crystal Growth in the Solid State (Recystallization). *Physica,* 15 (1-2): 92-106, 1949.

[95] Nielsen, J. P. Origin of Annealing Twins. *Acta Metallurgica,* 15 (6): 1083-1085, 1967.

[96] Dash, S. and N. Brown. An Investigation of Origin and Growth of Annealing Twins. *Acta Metallurgica,* 11 (9): 1067-1075, 1963.

[97] Merklen, P., E. Furubayashi and H. Yoshida. Formation of Annealing Twins and Stacking Faults During Primary Recrystallization of Pure Nickel. *Transactions of the Japan Institute of Metals,* 11 (4): 252-256, 1970.

[98] Goodhew, P. J. Annealing Twin Formation by Boundary Dissociation. *Metal Science,* 13 (3-4): 108-112, 1979.

[99] Plimpton, S. Fast Parallel Algorithm for Short-Range Molecular Dynamics. *Journal of Computational Physics,* 117 (1): 1-19, 1995.

[100] Plimpton, S. Computational Limits of Classical Molecular Dynamics Simulations. *Computational Materials Science,* 4 (4): 361-364, 1995.

[101] Liao, X. Z., F. Zhou, E. J. Lavernia, D. W. He and Y. T. Zhu. Deformation twins in nanocrystalline Al. *Applied Physics Letters,* 83 (24): 5062-5064, 2003.

[102] Yamakov, V., D. Wolf, S. R. Phillpot and H. Gleiter. Deformation twinning in nanocrystalline Al by molecular dynamics simulation. *Acta Materialia,* 50 (20): 5005-5020, 2002.

[103] Yamakov, V., D. Wolf, S. R. Phillpot, A. K. Mukherjee and H. Gleiter. Dislocation processes in the deformation of nanocrystalline aluminium by molecular-dynamics simulation. *Nature Materials,* 1 (1): 45-48, 2002.

[104] Cao, A. J. and Y. G. Wei. Molecular dynamics simulation of plastic deformation of nanotwinned copper. *Journal of Applied Physics,* 102 (8): 1-5, 2007.

[105] Froseth, A. G., P. M. Derlet and H. Van Swygenhoven. Grown-in twin boundaries affecting deformation mechanisms in nc-metals. *Applied Physics Letters,* 85 (24): 5863-5865, 2004.

[106] Shabib, I. and R. E. Miller. A molecular dynamics study of twin width, grain size and temperature effects on the toughness of 2D-columnar nanotwinned copper. *Modelling and Simulation in Materials Science and Engineering,* 17 (5): 1-14, 2009.

[107] Gertsman, V. Y. and K. Tangri. Computer Simulation Study of Grain Boundary and Triple Junction Distribution in Microstructures Formed by Multiple Twinning. *Acta Metallurgica et Materialia,* 43 (6): 2317-2324, 1995.

[108] Gertsman, V. Y., K. Tangri and R. Z. Valiez. On the Grain Boundary Statistics in Metals and Alloys Susceptible to Annealing Twinning. *Acta Metallurgica et Materialia,* 42 (6): 1785-1804, 1994.

[109] Reed, B. W. and M. Kumar. Mathematical methods for analyzing highly-twinned grain boundary networks. *Scripta Materialia,* 54 (6): 1029-1033, 2006.

[110] Mahin, K. W., K. Hanson and J. J. W. Morris. Comparative-Analysis of the Cellular and Johnson-Mehl Microstructures Through Computer-Simulation *Acta Metallurgica,* 28 (4): 443-453, 1980.

[111] Rickman, J. M., W. S. Tong and K. Barmak. Impact of Heterogeneous Boundary Nucleation on Transformation Kinetics and Microstructure. *Acta Materialia,* 45 (3): 1153-1166, 1997.

[112] Lee, S.-B., J. M. Rickman and K. Barmak. Phase transformation kinetics and self-patterning in misfitting thin films. *Acta Materialia,* 51 (20): 6415-6427, 2003.

[113] Dillon, S. and S.-B. Lee, Personal Communication 2008.

[114] Uchic, M. D., M. A. Groeber, D. M. Dimiduk and J. P. Simmons. 3D Microstructural Characterization of Nickel Superalloys Via Serial-Sectioning Using a Dual-Beam FIB-SEM. *Scripta Materialia,* 55 (1): 23-28, 2006.

[115] Lee, S.-B., A. D. Rollett and G. S. Rohrer. Three-Dimensional Microstructure Reconstruction Using FIB-OIM. *Materials Science Forum,* 558-559 915-920, 2007.

[116] Peralta, P., L. Llanes, A. Czapka and C. Laird. Effect of Texture and Grain size as Independent Factors in the Cyclic Behavior of Polycrystalline Copper. *Scripta Metallurgica et Materialia,* 32 (11): 1877-1881, 1995.

[117] Wu, Z. and J. M. Sullivan. Multiple material marching cubes algorithm. *International Journal for Numerical Methods in Engineering,* 58 (2): 189-207, 2003.

[118] Lorensen, W. E. and H. E. Cline. Marching cubes: a high resolution 3D surface construction algorithm. *Computer Graphics,* 21 (4): 163-169, 1987.

[119] Basinger, J. A., E. R. Homer, D. T. Fullwood and B. L. Adams. Two-dimensional grain boundary percolation in alloy 304 stainless steel. *Scripta Materialia,* 53 (8): 959-963, 2005.

[120] Frary, M. and C. A. Schuh. Percolation and statistical properties of low- and high-angle interface networks in polycrystalline ensembles. *Physical Review B,* 69 (13): 134115, 2004.

[121] Frary, M. and C. A. Schuh. Modeling and Simulation of the Percolation Problem in High-Tc Superconductors: Role of Crystallographic Constraints on Grain Boundary Connectivity. Interfacial Engineering for Optimized Properties III, San Francisco, 291-296, 2004.

[122] Frary, M. and C. A. Schuh. Connectivity and percolation behaviour of grain boundary networks in three dimensions. *Philosophical Magazine A - Physics of Condensed Matter Structure Defects and Mechanical Properties,* 85 (11): 1123-1143, 2005.

[123] Fullwood, D. T., J. A. Basinger and B. L. Adams. Lattice-based structures for studying percolation in two-dimensional grain networks. *Acta Materialia,* 54 (5): 1381-1388, 2006.

[124] Gaudett, M. A. Applicability of Bond Percolation Theory to Intergranular Stress-Corrosion Cracking of Sensitized ALSL 304 Stainless-Steel. *Metallurgical and Materials Transactions A - Physical Metallurgy and Materials,* 25 (4): 775-787, 1994.

[125] Schuh, C. A., M. Kumar and W. E. King. Analysis of grain boundary networks and their evolution during grain boundary engineering. *Acta Materialia,* 51 (3): 687-700, 2003.

[126] Schuh, C. A., R. W. Minich and M. Kumar. Connectivity and percolation in simulated grain-boundary networks. *Philosophical Magazine,* 83 (6): 711-726, 2003.

[127] Wells, D. B., J. Stewart, H. A.W., P. M. Scott and D. E. Williams. The Use of Percolation Theory to Predict the Probability of Failure of Sensitized Austenitic Stainless-Steels by Intergranular Stress-Corrosion Cracking. *Corrosion,* 45 (8): 649-660, 1989.

[128] Wright, S. I. and R. J. Larsen. Extracting twins from orientation imaging microscopy scan data. *Journal of Microscopy,* 205 (3): 245-252, 2002.

[129] Pande, C. S., M. A. Imam and B. B. Rath. Annealing Twins in f.c.c. Metals and Alloys. Interface Migration and Control of Microstructure, Detroit, Michigan, 125-129, 1984.

[130] Pande, C. S., M. A. Imam and B. B. Rath. Study of Annealing Twins in FCC Metals and Alloys. *Metallurgical and Materials Transactions A - Physical Metallurgy and Materials,* 21 (11): 2891-2896, 1990.

[131] Smith, C. S. and L. Guttman. Measurement of Internal Boundaries in Three-Dimensional Structures By Random Sectioning. *Transactions of the American Institute of Mining and Metallurgical Engineers,* 197 (1): 81-87, 1953.

[132] Garbacz, A. and M. W. Grabski. Modelling of CSL Boundaries Distribution in Polycrystals. *Scripta Metallurgica* 23 (8): 1369-1374, 1989.

[133] Garbacz, A. and M. W. Grabski. The Relationship Between Texture and CSL Boundaries Distribution in Polycrystalline Materials - II. Analysis of the Relationship Between

Texture and Concidence Grain Boundary Distribution. *Acta Metallurgica et Materialia,* 41 (2): 475-483, 1993.

[134] Kiemele, M. J., S. R. Schmidt and R. J. Berdine. Normal Distribution. *Basic Statistics.* Air Academy Press & Associates, LLC., Colorado Springs, 37-54, 2000.

[135] Press, W. H., S. A. Teukolsky, W. T. Vetterling and B. P. Flannery. Uniform Deviates. *Numerical Recipes in C.* Cambridge University Press, New York, 275-286, 1992.

[136] Zhao, J. and B. L. Adams. Definition of an Asymmetric Domain for Intercrystalline Misorientation in Cubic Materials in the Space of Euler Angles. *Acta Crystallographica,* A44 (3): 326-336, 1988.

[137] Saylor, D. M., B. El-Dasher, B. L. Adams and G. S. Rohrer. Measuring the Five Parameter Grain Boundary Distribution From Observations of Planar Sections. *Metallurgical and Materials Transactions A - Physical Metallurgy and Materials Science,* 35A (7): 1981-1989, 2004.

[138] Miodownik, M., A. W. Godfrey, H. E.A. and D. A. Hughes. On boundary misorientation distribution functions and how to incorporate them into three-dimensional models of microstructural evolution. *Acta Materialia,* 47 (9): 2661-2668, 1999.

[139] Miller, H., Personal Communication 2009.

[140] Garbacz, A. and M. W. Grabski. The Relationship Between Texture and CSL Boundaries Distribution in Polycrystalline Materials - I. The Grain Boundary Misorientation Distribution in Random Polycrystal. *Acta Metallurgica et Materialia,* 41 (2): 469-473, 1993.

[141] Pan, Y. and B. L. Adams. On the CSL Grain Boundary Distributions in Polycrystals. *Scripta Metallurgica et Materialia,* 30 (8): 1055-1060, 1994.

[142] Morawiec, A., J. A. Szpunar and D. C. Hinz. Texture Influence of the Frequency of Occurence of CSL-Boundaries in Polycrystalline Materials. *Acta Metallurgica et Materialia,* 41 (10): 2825-2832, 1993.

[143] Fenn, R. *Geometry.* Springer-Verlag London Limited, Great Britain, 2001.

[144] Stauffer, D. *Introduction to Percolation Theory.* Taylor & Francis Inc., Philadelphia, 1985.

[145] Tomasz, K., M. Konstantin and M. Marian. *Computational Homology.* Springer-Verlag, New York, 2004.

[146] Montgomery, D. C., G. C. Runger and N. D. Hubele. Continuous Random Variables. *Engineering Statistics.* John Wiley & Sons, Danvers, MA, 53-57, 2006.

Appendix A Probability Density Function, Cumulative Distribution Function, and Multiples of Random Distribution

The probability density function is used to describe the probability distribution of a continuous function, *f(x)*, and has the properties of

$$f(x) \geq 0 \text{ and } \int_{-\infty}^{\infty} f(x) = 1. \tag{A.1}$$

The probability of having value *X* between the range of *a* to *b* is calculated as the area under the curve between values *a* and *b* in the probability density function plot with [146],

$$P(a < X < b) = \int_{a}^{b} f(x)dx. \tag{A.2}$$

A direct way of obtaining the probability distribution is through the cumulative distribution function. The cumulative distribution function, *F(x)*, is the integration of the probability density function as shown by,

$$F(x) = \int_{-\infty}^{x} f(x)dx. \tag{A.3}$$

The probability of having value *X* between *a* and *b* can then be directly obtained from the cumulative distribution function with,

$$P(a < X < b) = F(b) - F(a). \tag{A.4}$$

Since the cumulative distribution function provides probabilities, it is always a positive value ($F(x) \geq 0$), and as x approaches infinity or the limits of the integral, the cumulative distribution function approaches 1 as can be seen in Fig. A.1(B).

The orientation distribution function is very similar to the probability density function with the exception that the summation of the function multiplied by the bins being equal to the

summation of the volume of the bins over the range of the orientation space rather than equal to 1, as shown with,

$$\int_0^{\Omega} f(x)dx = \int_0^{\Omega} dx, \tag{A.5}$$

where Ω is the range of the bins in orientation space. Such a normalization of the orientation distribution function means that the area under the curve will depend on the range of the bins. Multiples of random is used as the units to negate the effects of the range of orientation space and to allow easy comparison with the distributions expected from a random material.

Figure A.1 shows the visual comparisons between the three different methods of representing the distribution of misorientation angles obtained from the MacKenzie distribution and an experimental data set. In all the plots, the blue lines show the standard MacKenzie distribution of misorientation angles expected in a random material, while the pink lines show the distribution of misorientation angles obtained from the corroded 2124 aluminum alloy sample discussed in Section 3.1.1. Since the MacKenzie distribution represents the distribution of misorientation angles that is expected of a random material, the characteristic curve observed in the probability density function becomes a horizontal line of 1 MRD across all misorientation angles. To obtain the corresponding MRD plot of the experimental data set, the probability density function is divided by the MacKenzie probability density function and subsequently normalized with Equation A.5. As seen in Fig. A.1(C), experimentally observed materials often show larger populations of low angle grain boundaries than expected from the MacKenzie distribution.

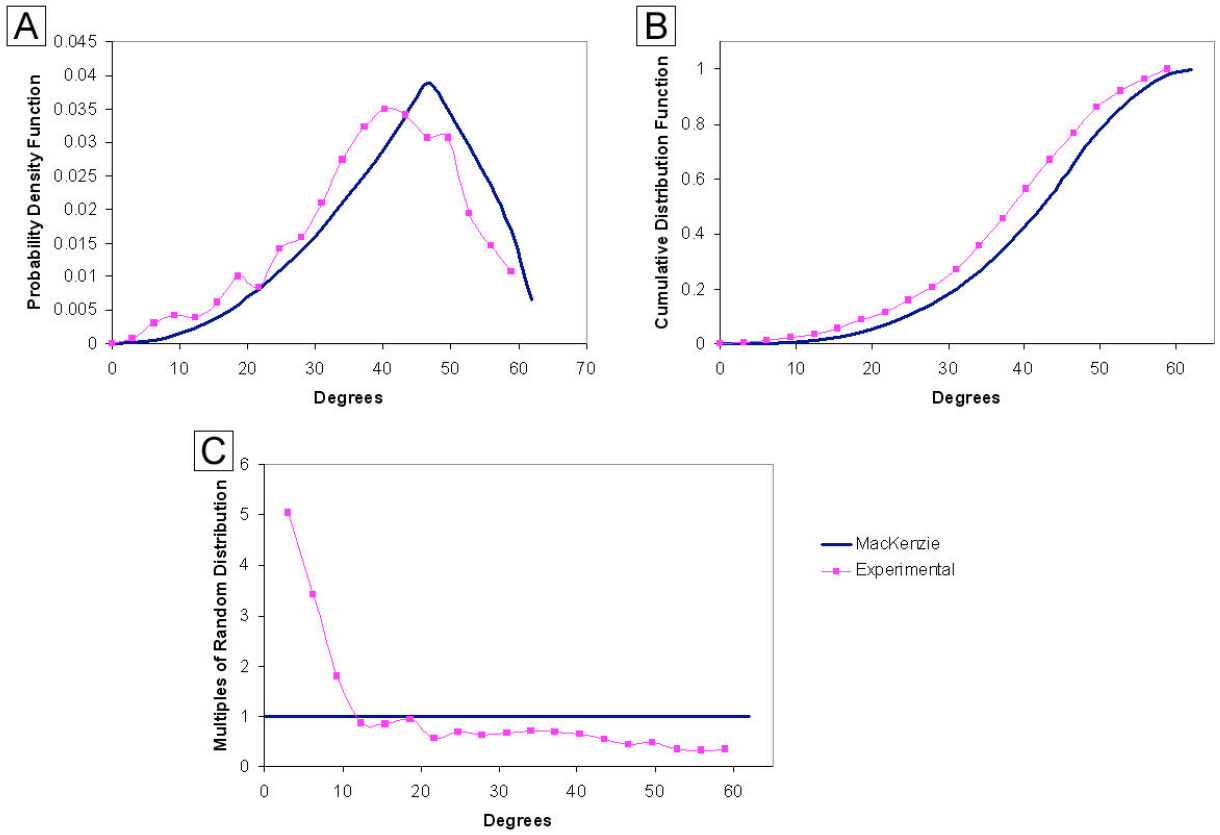

Figure A.1. The MacKenzie and an experimental distribution of misorientation angles represented with (a) probability density function, (b) cumulative distribution function, and (c) multiples of random distribution.

Appendix B Algorithms for Microstructure Generation

B.1 Plank Generator

The Plank Generator algorithms can be found online at: http://latir.materials.cmu.edu/lisachan/codes/. The algorithm named GenPlank.cpp generates plank structures that contain equal volume grains, while the algorithm named GenPlank2.cpp generates plank structures that contain grains of various thicknesses to model after the input grain size distribution.

B.2 Voronoi Tessellation Growth

The Voronoi tessellation growth algorithm named voronoi_cell_nucl_BCCgrid-NonPeriodic.c was used to generate the idealized tetrakaidecahedron structures used in this dissertation. A copy of this algorithm can be found online at: http://latir.materials.cmu.edu/lisachan/codes/.

Appendix C Algorithms for Characterization of the Microstructural Features

C.1 Σ3 and Twin Boundary Fractions

The algorithms used for identifying the Σ3 and coherent twin relationships for each triangular element of the conformed surface mesh are named CountTwins.cpp and TruncateS3.cpp. CountTwins.cpp identifies the triangular elements that have a coherent Σ3 relationship, and outputs a list of grain pairs and their corresponding fraction of coherent Σ3 triangular elements that make up the boundary. This list can then be input into TruncateS3.cpp to remove identified coherent Σ3 boundaries that have less than a threshold fraction of triangular elements being coherent. Both algorithms can be found online at: http://latir.materials.cmu.edu/lisachan/codes/.

C.2 Σ3 Cluster Distributions

To characterize the Σ3 cluster distribution, TwinStats.cpp and TwinStats-VCMD.cpp were used to analyze the microstructures. TwinStats.cpp will identify all the grain clusters that are related with a Σ3 relationship, and output a list of grain clusters (groups of integers that are unique to each grain). This list can then be fed into TwinStats-VCMD.cpp to calculate the center of mass and volume of each grain, and output distributions of grain cluster volume with respect to the number of grains per cluster. Both algorithms can be found online at: http://latir.materials.cmu.edu/lisachan/codes/.

C.3 Twin Cluster Distribution and Twin Removal

To characterize the twin cluster distribution, the list of coherent Σ3 boundaries obtained from CountTwins.cpp and TruncateS3.cpp is used as input files for LinkTwins.cpp. LinkTwins.cpp will take the pairs of integers that identify pairs of unique grains, and link the integers into clusters by matching the integer numbers. LinkTwins.cpp has the additional option of reading in the structure information and removing the twin grains by having the first grain in the twin cluster consume the remaining grains in the cluster. LinkTwins.cpp can be found online at: http://latir.materials.cmu.edu/lisachan/codes/.

Appendix D Algorithms for Crystallography Generation

D.1 Fiber Textures

The algorithm named TextureGen.cpp will generate a list of Euler angles that belong to either the <100>, <110>, or <111> fiber texture. TextureGen.cpp can be found online at: http://latir.materials.cmu.edu/lisachan/codes/.

D.2 CSL Boundary Lattice Misorientations

CSLgen.cpp will search through the Euler angle space and produce a list of any CSL sigma value (up to Σ49c) that is needed. This algorithm can be found online at : http://latir.materials.cmu.edu/lisachan/codes/.

Appendix E Orientation Assignment Algorithms

E.1 Algorithm for Orientation Assignment - MD Version

The algorithm used for assigning grain orientations to the structure such that orientation distribution and misorientation distribution match the target distributions is named texturelist_ultimate.c. The main algorithm and any necessary header files can be found online at: http://latir.materials.cmu.edu/lisachan/codes/texturelist/.

E.2 Algorithm for Orientation Assignment - GBCD Version

The algorithm used for assigning grain orientations to the structure such that the orientation distribution and the five-parameter grain boundary character distribution match the target distributions is named texturelist_5DQuat.c. The main algorithm and any necessary header files can be found online at: http://latir.materials.cmu.edu/lisachan/codes/texturelist/.

Appendix F Twin Insertion Algorithm

The InsertTwin.cpp algorithm will take a structure and generate twins either based on a list of target Σ3 clusters, or randomly with a target number of twin grains. When generating twins based on a list of Σ3 clusters, the algorithm requires the output from TwinStats.cpp such that any Σ3 clusters that existed in the structure prior to the start of the algorithm can be included in the statistics. A copy of InsertTwins.cpp can be found online at:

http://latir.materials.cmu.edu/lisachan/codes/